SIGNAL PROCESSING OF UWB RADAR SIGNALS FOR HUMAN DETECTION BEHIND WALLS

Mohamed Hussein Emam Mabrouk

THESIS SUBMITTED TO THE

FACULTY OF GRADUATE POSTDOCTORAL STUDIES

IN PARTIAL FULFILLMENT OF THE REQUIREMENTS

FOR THE DOCTORATE IN PHILOSOPHY DEGREE IN ELECTRICAL ENGINEERING AND COMPUTER SCIENCE

Ottawa-Carleton Institute for Electrical and Computer Engineering
School of Electrical Engineering and Computer Science
University of Ottawa

Abstract

Non-contact life detection is a significant component of both civilian and military rescue applications. As a consequence, this interest has resulted in a very active area of research.

The primary goal of this research is reliable detection of a human breathing signal. Additional goals of this research are to carry out detection under realistic conditions, to distinguish between two targets, to determine human breathing rate and estimate the posture.

Range gating and Singular Value Decomposition (SVD) have been used to remove clutter in order to detect human breathing under realistic conditions. However, the information of the target range or what principal component contains target information may be unknown. DFT and Short Time Fourier Transform (STFT) algorithms have been used to detect the human breathing and discriminate between two targets. However, the algorithms result in many false alarms because they detect breathing when no target exists. The unsatisfactory performance of the DFT-based estimators in human breathing rate estimation is due to the fact that the second harmonic of the breathing signal has higher magnitude than the first harmonic. Human posture estimation has been performed by measuring the distance of the chest displacements from the ground. This requires multiple UWB receivers and a more complex system.

In this thesis, monostatic UWB radar is used. Initially, the SVD method was combined with the skewness test to detect targets, discriminate between two targets, and reduce false alarms. Then, a novel human breathing rate estimation algorithm was proposed using zero-crossing method. Subsequently, a novel method was proposed to distinguish between human postures based on the ratios between different human breathing frequency harmonics magnitudes. It was noted that the ratios depend on the abdomen displacements and higher harmonic ratios were observed when the human target was sitting or standing.

The theoretical analysis shows that the distribution of the skewness values of the correlator output of the target and the clutter signals in a single range-bin do not overlap. The experimental results on human breathing detection, breathing rate, and human posture estimation show that the proposed methods improve performance in human breathing detection and rate estimation.

Acknowledgements

First and foremost, I am grateful to Allah (God) for all that I am and all that I have. I would like to express my deepest thanks and appreciation to my supervisor Dr. Miodrag Bolic for his valuable support and endless patience throughout this research. He took considerable time from his work schedule and family life to revise the manuscript of the thesis. I am also thankful to my co-supervisor Dr. Sreeraman Rajan for his patience and valuable guidance. In addition, I would like to thank Dr. Izmail Batkin for his helpful research comments and his encouragement.

I would also like to acknowledge Dr. Walid Atta, Dr. Wael Moussa and Dr. Mostafa Mohammed for their continuous support since my early days in Ottawa.

Many thanks go to my colleagues, Dr. Mohamad Forouzanfar, Dr. Mohamed Abousaif, Huthaifa Abderahman, Khaled Metwaly, and Assem Assem for their encouragement.

To my mother, parents-in-law, brothers and sisters, my son Nour, and my daughters, Hana, Malak, and Jana, I must express my sincere appreciation for their guidance, assistance, and love in every aspect of my life. Finally, I thank my lovely wife Heba for her patience, reassurance, and love.

Table of Contents

List of Tables

List of Figures

List of Acronyms

BPF	Band-Pass-Filter
CRE	Coarse Range Estimation
CRLB	Cramer-Rao Lower Bound
DFT	Discrete Fourier Transform
DRMD	Developed Respiratory Movement Detection
EDF	Empirical Distribution Function
ESR	Electronic Scanning Radar
FCC	Federal Communications Commission
FFT	Fast Fourier Transform
FIR	Finite Impulse Response
FMCW	Frequency Modulated Continuous Wave
G-O-F	Goodness-Of-Fit
GPR	Ground Penetrating Radar
IMF	Intrinsic Mode Function
LPD	Low Probability of Detection
LPI	Low Probability of Intercept
LTS	Linear Trend Subtraction
ML	Maximum Likelihood
MLMA	Maximum Likelihood Moving Average
MRM	Monostatic Radar Module
NBCW	Narrowband Continuous Wave
NBI	Narrowband Interference
PII	Pulse Integration Index
PN	Pseudo-Random Noise
PPI	Peak-to-Peak Interval
PPM	Pulse Position Modulation
PSD	Power Spectral Density
PTP	Pulse-To-Pulse
RCS	Radar Cross Section
REB	Research Ethic Board
RET	Reconfiguration and Evaluation Tool
RMD	Respiratory Movement Detection
ROC	Receiver Operating Characteristics
SAR	Synthetic Aperture Radar
SFCW	Stepped Frequency Continuous Wave
SNR	Signal-to-Noise Ratio
STFT	Short Time Fourier Transform
SVD	Singular Value Decomposition
ToA	Time of Arrival
TW-TOF	Two-Way Time-of-Flight
UWB	Ultra-Wide Band

List of Symbols

α	The maximum allowable false alarm probability
β	Threshold assigned to constant false alarm rate
δ	Dirac delta function
ϵ_r	Relative permeability of wall material
σ	Standard division
σ^2	Variance
σ_s	The standard division of the breathing signal amplitude
λ	Scale parameter
λ_j	j^{th} singular value
γ	The skewness value
γ_j	Threshold assigned to the j^{th} decision matrix
μ_a	Mean of the amplitude of symbol sequence
τ	Discrete fast sample time
BW	Bandwidth
C	The speed of light
f_b	The human breathing frequency
f_L	Lower cutoff frequency
f_l	Lower transition of IIR-BPF
f_s	Sampling frequency in slow time direction
f_U	Upper cutoff frequency
f_u	Upper transition of IIR-BPF
$\hat{f}$	Estimated frequency
H_0	The null hypothesis
H_1	The alternative hypothesis
J	The number of the singular values

k	Shape parameter
m	Scan index
M	The total number of scans
m^*	The lowest DFT of the human breathing rate range
$M^* - 1$	The highest DFT of the human breathing
n	The range-bin index
N	The total number of range-bins
N_{DFT}	Number of DFT frequency points
n_q	Number of even multiples of 5859.36 ps
$P_x(x)$	Probability distribution function of x
P_D	Probability of detection
P_{fa}	Probability of false alarms
r^*	The estimated range
$R_{yx}(\tau)$	Cross-correlation between x and y with time delay τ
S	Singular values matrix
t	Discrete slow sample time
U	Left singular vector matrix
V	Right singular vector matrix
$W(f_i, \tau)$	Rectangular window applied at frequency f_i at fast time τ
$W(v, n)$	M^*-sized rectangular window at range-bin n
X	Data matrix
$X(m)$	The amplitude of the range profile in the slow time direction
$y(t, \tau)$	The breathing signal at slow time t and fast time τ
$Y(f, \tau)$	The DFT of the breathing signal at fast time τ
$Y(f, v)$	The 2-D DFT of the breathing signal
$\tilde{Y}_{LTS}(m, n)$	Filtered received range profiles after applying LTS method

$Y_{DFT}^{W}(m,n)$	Windowed DFT of the filtered data matrix
$Y_{DFT}^{W}(m,n)_j$	Windowed DFT of the jth decision matrix
$Y_{EF}(f,\tau)$	The DFT of the breathing signal after applying EF method
$Y_{mean}(f,\tau)$	The DFT of the breathing signal after applying MA method
$Y_{HPF}(m)$	The output of the highpass filter
$Y_W(i,\tau)$	Breathing spectrum after breathing harmonics reduction

Chapter 1

Introduction

It is necessary to monitor subject's breathing behind the wall in many applications such as security applications, rescue operations, home care applications, and military surveillance operations.

Human target detection behind the wall is based on Doppler variations built upon on movements such as chest movement. The first radar vital sign monitoring system was developed in the middle of the 1980's by Georgia Technology Research Institute (GTRI) and a patent on the system was issued in 1992 [*1*]. In 1990, Chuang used clutter cancelation circuits for microwave systems to sense physiological movements remotely through an obstacle [*2*]. Since the late of 1990's, many radar systems have been able to detect single human breathing behind a wall from near range [*3*].

The ability to detect breathing movements in the human body using ultra-wide band (UWB) radar has been reported [*4*,*5*]. Since the beginning of this century, many UWB radar systems have been employed to detect human breathing [*5*,*6*,*7*,*8*,*9*] in realistic conditions [*10*,*11*,*12*,*13*], to estimate the number of targets [*14*,*15*], and to discriminate between human and animal breathing [*9*,*16*].

The detection of humans behind walls is an open and evolving research area. Engineers in the field are searching for methods to optimize the requirements of radar systems and to employ an efficient detection algorithm. These increase the opportunities for utilizing the radar systems in important and critical applications such as rescue operations, and security and military applications.

1.2 Motivations

Detection of human breathing in free space is very important in medical, and homecare monitoring applications. Also, human breathing detection behind walls is very important in rescue operations, military, and security applications.

Regarding rescue operation applications, the United States Geological Survey (USGS) introduced a study on earthquake disasters. It counted twenty two earthquakes with 50,000 or more deaths from 1556 up until 2010. The 2004 earthquake in Sumatra was the third largest earthquake in the world since 1990, and 227,898 people were killed or missing and presumed dead [*17*]. Disasters such as earthquakes are not the only causes of high death tolls. Hundreds of people also lose their lives with the collapse of buildings all over the world. The World Trade Center disaster in September, 2011, claimed more than 5000 lives, partially due to the collapsed towers. In Bangladesh, May, 2013, a collapsed building during a fire contributed to over 650 deaths. Obviously, the more time passes the less likely it is to find people alive. If survivors are found and rescued earlier, the number of victims could be much lower. Development of a system that can detect human vital signs behind walls or under rubble will reduce the number of deaths due to natural disasters.

In military and security applications, it is desirable to detect human breathing, distinguish between multiple targets, and estimate the postures of the targets. The number of targets and respective posture information can be very useful for determining the best breaking in suspicious places scenario.

In hospital and homecare monitoring applications, a study in 2012 on the state of aging and health in America reported that the population of Americans aged 65 or older will reach 89 million people in 2050 [*18*]. A study on the profile of older Americans, in 2012, by the U. S. Department of Health and Human Services reported that about 28% of older persons live alone [*19*]. One of every three adults aged 65 or older falls each year and about 30% of these falls result in serious injuries [*20*]. Sometimes, it is difficult for older persons who lives alone to stand after falling down, especially if they have medical problems with their limbs. Remote contact-less detection of a fall is very important in this application.

Four proposed challenges needed to be addressed in order to detect human breathing behind the walls. These challenges include the ability to estimate an accurate range, to distinguish between two targets, to estimate a target's breathing rate, and in addition, to estimate a target's posture. In the following, we will discuss the dominant problems in human breathing detection systems based on these challenges.

1.2.1 Dominant Problems in Human Breathing Detection Systems

The dominant problems that can limit the detection through-the-wall device operation are: *the clutter, multiple signals received from multiple targets, drifting of the estimated target range from the real range, high errors in the estimated breathing rate, and no posture information being available*. The goals based on reliable detection of breathing signal are: the human breathing detection capability in realistic conditions, discrimination between multiple targets, the accuracy of target localization, the accuracy of the human breathing rate estimation, and the human posture estimation. Signal processing algorithms must be applied to suppress the clutter, enhance the signal to noise ratio, extract the human breathing signal, and extract posture and breathing rate information.

1.2.1.1 Human Breathing Detection in Realistic Conditions

The human breathing detection in realistic conditions means the ability of removing clutter to detect the human breathing at its real range. The clutter suppression problem is discussed in this section. The human chest displacement, caused by breathing, is between 10 and 20 mm [*6*,*21*]. When a human target is illuminated by an electromagnetic wave, the reflected wave will be modulated by the periodic movement due to breathing. The reflected wave from the target is weak compared to the waves reflected from walls. Generally speaking, the changes of amplitude are negligible. Therefore only frequency, phase and arrival time changes can be used for the detection of the periodic movement of the chest wall. Detecting such a weak signal in an environment filled with clutter and noise is a problem that needs to be solved [*22*]. Range gating has been used to remove the clutter [*7*]. However, the target range information needs to be known. SVD has been used to eliminate the effect of clutter and noise [*15*,*23*,*24*,*25*,*26*]. However, the principal component that contains the target information may be unknown. Discrete Fourier Transform (DFT) and Short Time Fourier Transform (STFT) have been used to detect the human breathing after applying a clutter suppression method [*12*,*13*,*24*,*26*]. However, assigning the suitable threshold for high probability of detection and low number of false alarms was problematic because the distributions of the spectrum magnitude of the clutter and target signals overlap. In addition, DFT and STFT need long observation time and long window duration time, respectively, for high frequency resolution. Also, selecting window size and type is a challenging matter in using STFT. Wavelet transforms have been used in detecting the human breathing [*6*,*27*,*28*]. However, a suitable type of wavelet should be studied for better detection. In [*9*], DFT has been used to distinguish between human breathing rates and dogs breathing rates. A challenging problem regarding detecting the human breathing on the basis of the spectrum analysis is the human breathing harmonics and large-scale human body movements [*29*,*30*,*31*]. This issue should be considered when using the DFT, STFT, and wavelet algorithms. What is required is a human breathing detection method that does not require prior knowledge of the target range and the principal component contains the target information. In addition the distribution of the correlator's output is presented in a target or clutter range-bin involving a non-overlapped distribution. This is carried out by studying the third moment of the correlator output squared. Such a method can be used to detect the human breathing in free space and behind walls.

1.2.1.2 Discrimination Between Multiple Targets

DFT and S transforms have been used to discriminate between multiple targets [*13*]. However, the discrimination process has been performed by visual inspection and false alarms may result in detecting clutter as human targets. In [*15*], a threshold that is a non-linear function of the range between the target and the radar has been used to distinguish between two targets using the spectrogram. The nonlinear threshold depends only on the range of the target and many false alarms may be detected. In [*32*], an adaptive cancelation method has been used to distinguish between two targets by removing the interference in the range-bins behind the first target. However, no clutter suppression method has been proposed and the interference is assumed to be additive. In [*9*], two targets have been detected on the basis of the breathing rate and the method depends on the accuracy of the breathing rate estimator. What is required is a method that can distinguish between two targets in free space and behind walls and does not rely solely on the spectrum analysis to avoid false human detections.

1.2.1.3 Human Breathing Rate Estimation

The problem of the high errors in the estimated breathing rate is discussed in this section. DFT, STFT, wavelets, and EMD have been used to estimate the human breathing rate in free space and behind the walls with high breathing rate estimation errors in some scenarios [*12*,*13*,*24*,*27*,*33*,*34*,*35*,*36*,*37*,*38*]. The main sources of error in human breathing rate estimation algorithms are: the large-scale displacements of the human body and the magnitude of the second harmonic may be higher than the magnitude of the first one. Large-scale displacements are the displacements of any human body part while breathing, except the chest or the abdomen. These displacements are like human swings while breathing, trembling hands, or coughing. The problem of the large-scale human displacements has been addressed in [*30*]. The moving average filter and the ellipse fitting methods have been used to eliminate the effect of the human body large-scale displacements. However, the problem of the second breathing harmonic magnitude being higher than the first one has not been addressed. High error in the estimated breathing rate is expected using these methods because the peak of the second breathing harmonic may be picked up as the breathing frequency in some scenarios. What is required is a method that eliminates the effect of the human breathing harmonics on the human breathing rate estimation process in free space and behind walls.

1.2.1.4 Human Posture Estimation

The problem of no posture information is available is discussed in this section. Human posture estimation is important in many applications such as security, military, homecare monitoring applications and rescue operations. Human posture estimation can be used to detect fallen elderly people on the ground/floor and can be used to predict the activity of the human behind walls. In [*39*], a training set of data has been used in a neural network to classify human postures. In [*40*] , the distance between the human torso and the ground/floor has been inspected to detect fallen people. If the distance between the torso and the ground/floor is very small, then the target is lying down. Human breathing rate, heartbeat rate, and movements toward the ground/floor while falling down have been studied to determine if the subject is standing or lying down. However, the human breathing harmonics may affect the detection. Also, in [*39*,*40*], many receivers have been used and more complicated radar systems are required. In [*41*,*42*], Doppler radars have been used to detect fallen people by tracking specific signatures of the fallen human body parts. However, many false alarms have been detected. In [*43*], two Doppler range control radars and three classifiers were used to analyze the human gait movement spectrum. Also, the human gait movement spectrum was studied to detect fallen people in [*44*,*45*]. As in [*41*,*42*], the motion of the human body parts motion was used to detect fallen people. To the best of this author's knowledge, there has been no research that uses the ratios between different human breathing frequency harmonics magnitude to extract posture information to estimate the human posture. A method that can distinguish between human postures in free space and behind walls based on the breathing harmonic magnitude ratios is needed.

1.2.2 State-Of-The-Art

While there has been extensive work to detect human breathing behind walls, to the best of the this author's knowledge, there has been no system solving all of these problems in Section 1.2.1 [*7*,*9*,*12*,*13*,*15*,*22*,*24*,*46*,*47*].

SVD has been used in clutter suppression in human breathing detection systems [*15*,*23*,*24*,*25*,*26*]. Identifying the principal components that are associated with noise and clutter is a nontrivial problem while using SVD for clutter suppression. DFT and STFT have been used to detect the human breathing after applying preprocessing and clutter removal algorithms [*12*,*13*,*24*,*26*]. However, the method that used to assign a threshold for the detection process was a challenging problem. The state-of-the-art algorithms are improved by proposing a method that does not require prior knowledge of which principal component contains the target information and can estimate accurate range and discriminate between two targets.

To estimate the human breathing rate, it was necessary to study the human breathing activity. The two main moving parts while breathing are the chest and the thorax [*48*]. On the basis of spectrum analysis, many human breathing rate estimators have been introduced in the state of the art [*12*,*13*,*24*,*27*,*33*,*34*,*35*,*36*,*37*,*38*]. Human breathing rate in free space and behind the walls is challenging for two reasons:

- The second breathing frequency harmonic may have magnitude higher than the first breathing frequency harmonic [*29*,*31*].
- Theoretically, the Fast Fourier Transform can be used to estimate the human breathing rate in a signal received in UWB radar receiver. However, experimental observations show large error because of human body large-scale displacements [*30*].

According to the author's knowledge, no one extracted the human posture information from the breathing signal spectrum. The movements of the chest and the abdomen may contain some information about the human posture. The displacements of the abdomen will change when the human changes his/her posture. This feature can be used to distinguish between fallen people on the ground/floor, and sitting or standing human postures.

1.3 Contributions

In this thesis, methods are introduced to solve all of the described problems in Section 1.2.1 using stationary monostatic UWB radar system. While performing our study, we observed the following: several major sources of error in human breathing estimation, the importance of including the abdominal movements in the human breathing model, the breathing signal spectrum contains the human posture information, the third moment of the probability distribution of the received signal changes when the target is absent, and the information of the target can be contained in any of first several principal components. We attempt to enhance the human breathing detection behind walls using these observations by the following contributions:

- It has been observed that the major source of error in human breathing estimation algorithms is due to the fact that the magnitude of the second harmonic is higher than the first one in some scenarios. This knowledge is utilized to derive a more accurate human breathing rate estimation algorithm.

Although state-of-the-art algorithms can detect and estimate the human breathing rate, the error of the estimated breathing frequency was high [*30*]. The contribution of the abdomen movements while breathing resulted in large magnitude of multiple harmonics of the breathing signals. The major source of errors in breathing rate estimation algorithms is due to the magnitude of second harmonic being higher than the magnitude of the first harmonic. This led to additional minor contributions:

- The model of the human breathing reflected signal received by PN-UWB radar is modified so that it includes the movements from the abdomen displacements.
- The knowledge of the existence of multiple breathing harmonics is utilized to derive a more accurate breathing rate estimation algorithm.
- The knowledge of the fact that the chest and the abdomen move while breathing is used to apply the constraint that limits the time intervals between each breath to reduce the breathing rate estimation error compared to the FFT-based estimators.

The novel observation of the displacements of the abdomen while breathing and its effect on the received breathing signal spectrum led to the development of the novel human breathing rate estimation algorithm based on the zero-crossing with the time intervals between each breath constraint. The Peak-to-Peak Interval (PPI) of the reflected signal is used to readjust the boundaries of the band-pass filter. This is done to eliminate the noise and obtain more accurate breathing rate estimation. A comparison was made among four different human breathing rate estimators: FFT, moving average, ellipse fitting, and zero-crossing combined with the time intervals between each breath constraint by collecting measurements from a human breathing normally while sitting, standing, and lying down at different orientation angles from the radar. The mean absolute error of the estimated breathing frequency of a human breathing behind the wall was higher than that in the anechoic chamber or office environment using FFT. By using the zero-crossing method the mean absolute error has been reduced by 23.13%, 33.46%, and 49.18%

in an anechoic chamber, an office environment, and behind a 20 cm gypsum wall, respectively, compared to the FFT estimator.

- It has been observed that the contribution of the abdomen displacement relative to the contribution of the chest displacement is different at different postures. This observation is utilized to propose a novel method that can distinguish between fallen people on the ground/floor and people sitting or standing.

The displacements of the abdomen change when the human changes his/her posture. This led to two minor contributions:

- The ratio of the harmonics magnitude of the breathing frequency is utilized to determine posture of a person as well as changes in posture of a single person.
- The displacements of the chest or the abdomen are very small in the dorsal posture. This observation can be utilized to detect fallen people on the ground/floor based on studying the ratios between different breathing harmonics.

These observations led to a method for estimating human posture from the breathing signal. The results of this method show that the ratio between the second and the first breathing frequency harmonic magnitudes is the least when the human is lying down on his/her back and increases when he/she is sitting and standing. For specific threshold, probability of detection for the lying down posture of one subject was 100%, 92%, and 83% in an anechoic chamber, an office environment, and behind a 20 cm gypsum wall, respectively. However, further analysis showed that the threshold level needs to be adapted for each person and therefore this approach requires further analysis.

- Probability distribution of the received signal after filtering was analyzed and it was observed that the third moment in a range-bin in slow time drops exactly in the range-bin where the target is. This drop is independent of whether there is a wall or not in between the target and the radar. This observation can be used to reliably detect the closest target.

This observation led to minor contributions:

- This feature can be used to estimate the target range.
- This feature can be used to distinguish between clutter and human targets. The false alarms of the human breathing detection can be reduced by using this feature.

This contribution led to the development of a human breathing detection method based on studying the skewness value of the amplitude squared of the received signal. This method can present the clutter and target amplitudes in a non-overlapped distributions. Thus assigning a threshold for the target detection is not a problematic operation. The method was tested to detect a human behind a wall. The target was standing 1.5 m behind a 20 cm gypsum wall. Data was collected from two different subjects. A total 46 measurements were collected. The null hypothesis was not rejected when there was no target. Target detection was rejected twice when there was a target in a total 46 measurements. This method resulted in no type I error and 4.34% type II error.

- It has been observed that the information about the target can be contained in any of the initial singular components. A novel human breathing detection algorithm is proposed that does not require priori knowledge of which principal component contains the target information. Based on this observation, we apply method to:

- Combine between SVD and the analysis of the skewness of the received signal to estimate the range of the first target.
- Discriminate between two targets.

The state-of-the-art research used SVD to remove the clutter and noticed that the target information is in the second principal component. However, we observed that the target information is not always in the second principal component. The presence of a target in a range-bin was detected using a novel method which combines the SVD and the skewness test method. This method does not require prior knowledge of which principal component contains the target information. The proposed method is not only detecting human breathing, but can also distinguish between two targets by removing the principal component one after the other. The state-of-the-art uses time and frequency analysis methodology to discriminate between targets. In our research's methodology, a study was made on how to discriminate between targets using the SVD and the skewness determination in each range-bin. We were able to discriminate between two targets standing in an anechoic chamber, an office environment, and behind a 20 cm gypsum wall, separated by 1 m, 0.5 m, and 0.3 m between each other. Although the minimum distance between targets that can be resolved in free space is 20 cm, we were not able to discriminate between targets behind walls separated by less than 30 cm.

The following papers and patent were published based on the research leading to this thesis:

- Mohamed Mabrouk, Sreeraman Rajan, Miodrag Bolic, Izmail Batkin, Hilmi R. Dajani, Voicu Z. Groza, "Detection of Human Targets behind the Walls Based on Singular Value Decomposition and Skewness Variations," 2014 IEEE Radar Conference, Cincinnati, May 2014, pp. 1466-1470.
- Mohamed Mabrouk, Izmail Batkin, Sreeraman Rajan, Miodrag Bolic, Hilmi R. Dajani, Voicu Z. Groza," Remote Sensing of Human Breathing at a Distance," US Provisional Patent, 61/994,408, May, 16, 2014.
- Mohamed Mabrouk, Sreeraman Rajan, Miodrag Bolic, Izmail Batkin, Hilmi R. Dajani, Voicu Z. Groza,"Model of Human Breathing Reflected Signal Received by PN-UWB Radar," 36th Annual International Conference of the IEEE Engineering in Medicine and Biology Society, Chicago, Aug. 2014.

1.4 Thesis Outline

This thesis consists of seven chapters in total. The first chapter includes an introduction, motivations, and the expected contributions.

In Chapter two, the first section introduces the types of radar technology used in human detection behind walls. The second section presents the operating center frequency, bandwidth, and SNR suitable for the best detection performance of human breathing behind the wall. The third section discusses the problems that needed to be solved in order to detect a human breathing behind a wall or under rubble. This is followed by a literature review on human breathing detection in free space and behind walls. The last section presents the radar system that was used in collecting the experimental data.

In Chapter three, a literature review on the human breathing detection signal processing is presented.

In Chapter four, the statistical approach used in this thesis to detect the range-bins that contain a target is introduced. After that, the SVD and skewness variation determination method to detect the human breathing and discriminate between two targets is proposed. Some results in an anechoic chamber, free space, behind a gypsum wall, and the structure lab in University of Ottawa, Ottawa, Canada, are also presented.

In Chapter five, a novel breathing rate estimation algorithm is proposed and the advantages of this algorithm are presented. A comparison is made between our proposed algorithm and the developed state-of-the-art algorithms.

In Chapter six, a novel method for human posture estimation is proposed using UWB radars. A distinction is made between human lying down posture and human sitting or standing posture.

In Chapter seven, the conclusion and potential future work are presented.

Chapter 2

Background

2.1 Types of Radar Technology

Narrowband continuous wave, narrowband pulsed wave, and ultra wideband radars were used to detect human breathing in free space and behind wall structures. Each technology has its advantages and disadvantages and the type of technology choose may involve optimizing engineering trade-offs between conflicting requirements of the application. The requirements of application may include the availability, cost, the interference immunity, obstacle penetration capability, the data acquisition time, ability to determine distance, and the ability to estimate the breathing rate. Also presented in this section, are the different radar technologies that have been used by the state-of-the-art to detect the human breathing in free space and behind walls. A comparison is made between these different technologies and the reasons for choosing the PN-UWB radar in this research are also included.

2.1.1 Narrowband Continuous and Pulsed Wave Radars

Narrowband continuous wave (NBCW) radars have been used for several years in human detection behind walls. Narrowband radars can detect phase variations with high sensitivity proportional to the transmitted wavelength. However, no range information is available and the system is sensitive to narrowband interference (NBI). The narrowband pulsed radar can detect the target range but with low accuracy, and the system is sensitive to NBI. Moreover, it shows poor time stability (time drift and jitter caused by imperfections in the triggering unit of a radar device) which increases non-zero Doppler components [*26*,*49*]. Non-zero Doppler components can increase the number of false alarms. Narrowband continuous and pulsed wave radars have the advantage of good detection of vital signs and are highly sensitive to phase variations. On the other hand, location information cannot be obtained using these radars, target discrimination is difficult and NBI may impact the detection process [*50*].

The first attempt to use microwave systems to sense physiological movements remotely through an obstacle with NBCW radars was in 1985 [*51*]. NBCW radars have the advantage of detecting small movements by detecting phase variation of the reflected wave from the target. Noise and clutter completely obscure the target, making the detection of life difficult. In 1990, Chuang used microprocessor-controlled automatic clutter-cancellation circuits to sense physiological movements remotely through the rubble [*2*]. Two microwave life locator systems working in L-band (2 GHz) and X-band (10 GHz) with transmitted power from 10 to 20 mW were used. The system was tested with a person sitting on a chair behind brick walls of different thickness. The performance of the L-band radar was acceptable up to 3 feet thickness, while the performance of the X-band radar degraded after 1.5 feet [*2*].

2.1.2 Ultra Wideband Radars

The United States Federal Communications Commission (FCC) defines an UWB signal as a signal with either a fractional bandwidth of 20% of the center frequency or more than 500 MHz. The fractional bandwidth is defined by:

$$BW = \frac{2(f_U - f_L)}{(f_U + f_L)} \tag{2.1}$$

where, f_U is the upper cutoff frequency and f_L is the lower cutoff frequency. UWB technology has the following advantages [*13*,*52*]:

1- Guarantees high range resolution.

2- Good penetration characteristics.

3- Possess good immunity against multipath interference.

4- Has the ability to operate indoor as well as outdoor areas.

5- Has the ability to reject clutter, high spatial resolution, and discriminate between targets close to each other.

UWB radars can track multiple targets, and provide better separation between targets and clutter due to its large bandwidth. Although UWB radars possess good immunity against multipath interference, this interference still affects detection and clutter is not completely eliminated in the detected signal. The use of correlation is effective for detecting range and overcoming the problems of multipath interference and clutter [*50*]. UWB radars guarantee an accurate estimate of the reflectors' range, overcome the problem of NBI, have good penetration characteristics, discriminate between multiple targets, and detect small movements through multiple scans. For these reasons, UWB radars stand out among other electromagnetic systems in the human breathing detection fields [*12*,*13*,*50*,*52*].

The first attempt to use UWB radar in medical applications for human body monitoring and imaging was in 1993 [*53*]. In 1996, the US Patent, 5,573,012, in remote sensing was awarded [*54*]. Since then, UWB radar is recognized as a sensor for remote sensing and imaging. By 1999, several publications related to the medical applications of UWB technology in cardiology, obstetrics, and detection of respiration rate appeared [*53*]. UWB radar technologies can be broadly categorized as Impulse, Pseudo-random Noise (PN), Frequency Modulated Continuous Wave (FMCW) radars, and Stepped Frequency Continuous Wave (SFCW) radars.

2.1.2.1 Impulse UWB Radars

Impulse UWB radars have been used widely in detection of human life behind walls. Several detection algorithms have been developed to enhance the received Signal-to-Noise Ratio (SNR). In 2004, Ossberger and Buchegger detected human breathing behind a brick wall of 20 cm thickness when the target was standing 5m from the radar [*6*]. A weakness exists in this study due to the fact that the authors subtracted the background by only subtracting the mean from the received signal, and attempted no enhancement of SNR, for example, by integrating a burst of received pulses, was attempted. In 2006, Levitas used UWB radar made by Geozondas Lithuania, with large operational bandwidth (11.7 GHz) to detect breathing and heartbeat of a human standing 2.4m behind a wall [*55*]. Chernyak proposed a method using multi-site UWB radar devices when searching for survivors in rubble [*56*]. In his work, the radar operating frequency was 2.25 GHz and the bandwidth was 0.5 GHz. The received SNR was 0 dB after coherent summation. In 2009, Baboli introduced a new wavelet based algorithm for estimating the detected breathing rate using 3.2 GHz bandwidth impulse radar [*27*]. In 2010, Levitas and Matuzas used impulse UWB radar with an operating frequency of 2.5 GHz and a bandwidth of 0.5 GHz to detect breathing of a target behind the wall. These researchers were able to discriminate the targets as being either human or a dog by the breathing rate. The receiver had a dynamic range equal to 78 dB from the noise level up to the largest clutter signal [*9*].

2.1.2.2 Random Noise and Pseudo Random UWB Radars

Random noise UWB radars are widely used for a variety of applications such as range profile measurements, detection of buried objects, Doppler estimation, Synthetic Aperture Radar (SAR) and Interferometric Synthetic Aperture Radar (ISAR) imaging [*57*]. The random noise radars use random noise waveform as a transmit signal. The Pseudo Random UWB (PN-UWB) Radar readjusts the time between the transmitted pulses using a pseudo random code and then transmits it. In 2003, Narayanan and Xu discussed the principles and applications of coherent random noise radar. Range profile was estimated using a correlation method and SNR was maximized for better small movement detection by combing between the advantages of a random noise UWB waveform with the power of the coherent processing [*58*]. The radar system was relatively immune to narrowband interference or jamming because of the UWB pulse advantages. In 2004, Narayanan recorded a 2-D high resolution image of two trihedral reflectors obscured behind trees, using a combination of UWB Random Noise Radar and SAR technique [*59*]. Lai, in [*60,61*], used UWB random noise radar with operating frequency from 350 MHz to 750 MHz, 23 dBm total transmitted power, a range resolution of 37.5 m, and 20 dB dynamic range to detect a human standing behind a 50 cm thick brick wall. In 2008, Sachs used the Pseudo Random UWB (PN-UWB) technology to track moving targets and detect people hidden by obstacles. The operating frequency of the radar was 2.5 GHz with bandwidth of 2500 MHz [*46*]. In 2011, Singh used PN-UWB Radar to detect human breathing behind different types of walls. He succeeded to detect the human breathing signal behind a one foot thick gypsum wall, a 4 cm wooden door, and a 12 cm thick brick wall [*24*]. In 2014, Lazaro used a PN-UWB Radar to detect and estimate the human breathing. He was able to detect if the received signal is from breathing activity or other types of movements [*29*].

2.1.2.3 UWB Frequency Modulated-Continuous Wave Radars

In 2009, Maaref published a study of UWB FMCW radar for detection of human beings moving inside a building. The radar operating frequency was from 1 GHz to 5 GHz and was used to detect a human walking behind a wall 20 cm thick. The system provided high range resolution. Cross range resolution was obtained by using a triangulation method. Experimental results showed a -8 dB and -25 dB attenuation when a human was standing behind a concrete wall and a concrete slab, respectively [*25*]. Anitori detected the life signs of people in free space using the same technology with a 25 mW transmitted power with no obstacle [*33*].

2.1.2.4 UWB Stepped Frequency- Continuous Wave (SFCW) Radars

In 2010, Grazzini tested using UWB SFCW Ground Penetrating Radar (GPR) as a rescue device to detect people after the collapse of buildings. The radar had an operating frequency range from 100 MHz to 1 GHz and a 1 mW transmitted power. The target was recumbent inside a tube of diameter 1m under a 1m thick pile of debris. The dynamic range was 100 dB [*62*].

Zhuge, in [*63*,*64*], discussed various UWB technologies. An operational frequency band from 1 to 2 GHz, 20m detection range, and 1.5m length array was used in this research. The radar system had a range resolution of 0.15m and a cross range resolution of 2m at 20m detection distance. The required dynamic range for this system was 120 dB. For FMCW radar, the data acquisition time was 100-500 μs and it provided high energy. In contrast, for SFCW radar, the data acquisition time was about 300 ms and it provided high energy and had a wide dynamic range. For Impulse Radar, the data acquisition time for a stroboscopic receiver was 118 μs and the dynamic range was fulfilled by time gating the antenna coupling and the wall reflection. For the Pseudo-random UWB Radar, the data acquisition time can be derived from the pulse repetition time which was selected as 0.13 μs. Time gating was used to achieve higher dynamic range. The noise radar was the fastest among all of them in data acquisition [*63*]. Nezirović in his PhD thesis compared the four UWB radar technologies in detecting human breathing behind walls or under rubble [*26*].

Table 2.1 summarizes the advantages and disadvantages of using these technologies [*26*,*63*].

Table 2.1 Advantages and disadvantages of various UWB Radar technologies.

UWB radar Technology	**CW UWB radars**	**Impulse radars**	**Pseudo-random UWB radars**
Time Stability	Stable	Stable	High time base stability
Availability	Requires highly linear signal generator	Readily available and widely used technology	Readily available and widely used technology
Cost	High cost	Inexpensive technology	Relatively inexpensive technology
Data acquisition time	Slow data acquisition (ms)	Moderately fast data acquisition (μs)	Fast data acquisition (μs)
Interference Immunity	Relatively immune to narrowband interference	Relatively immune to narrowband interference	Immune to narrowband interference
Dynamic range	It possesses very good dynamic range	Might have a problem maintaining linear dynamic range.	No impulse like waveforms, so makes better use of the available dynamic range than the impulse radar
Power	Good total power budget	Low average transmitted power	Low average transmitted power
Range gating	No possibility of range gating	Allows range gating	No possibility of range gating

To conclude, we need to use UWB technology in human breathing detection behind the walls because it has the capability of penetrating wall constructions. The PN-UWB technology is the fastest in data acquisition time. It is a readily available and inexpensive technology with wide dynamic range and low average transmitted power. Also, it is immune to interference and multipath problems. The author of this research is suggesting using the PN-UWB technology in human detection behind walls.

Although UWB radar can detect the movement of a target behind a barrier, one still needs to develop specialized signal processing algorithms to detect human breathing behind walls.

These algorithms should be validated using appropriate mathematical models and by experimental studies with human subjects.

2.2 Operating Center Frequency, Bandwidth, and SNR

The factors that characterize our UWB Radar system include: Operational center frequency, bandwidth, received signal-to-noise ratio, and the depth that the electromagnetic wave can reach and reflect to the receiver. Yarovoy proposed the following requirements for human breathing detection behind walls which are realistic in some scenarios [*4*]:

1) Maximal operational range of 20m in free space.
2) Penetration through brick walls with a total thickness up to 40 cm (in one way propagation).
3) Target positioning accuracy should be better than 30 cm.
4) Reflection coefficient from walls is up to −10 dB level.

Points 1 and 2 can be achieved by studying the propagation losses and Radar Cross Section (RCS) of the human body. The propagation losses decrease when the center frequency decreases. The radar cross section of the human body has its maximum values at the center frequencies from 1 to 2 GHz and from 3 to 5 GHz [*64*]. Table 2.2 introduces the total propagation loss in different types of walls [*63,64*].

Table 2.2 Total propagation loss for different wall materials (thickness of the wall is 0.2 m) [*64*].

Material	**Frequency(GHz)**	**Propagation loss (dB)**		
		Range: 0.5m	Range:10m	Range:20m
Concrete Block	1	-56.7	-108.7	-120.8
	3	-73.4	-125.4	-137.5
	5	-77.2	-129.2	-141.3
	7	-85.8	-137.8	-149.8
Brick	1	-50.6	-102.6	-114.6
	3	-67.5	-119.6	-131.6
	5	-78.9	-130.9	-143.0
	7	-95.1	-147.1	-159.2
Structure wood	1	-49.1	-101.1	-113.2
	3	-63.7	-115.7	-127.7
	5	-71.0	-123.0	-135.0
	7	-82.0	-134.0	-146.1

Results in [*25*] show that a transmitted waveform with a frequency in the L- or S-band is suitable for detecting the human breathing behind an obstacle, while results in [*26*] show that a bandwidth of 400 MHz and operating frequency less than 1 GHz produce good detection results. A bandwidth larger than 500 MHz can obtain positioning accuracy better than 30 cm. If the reflection coefficient from the wall is up to -10 dB, the dynamic range should be from 100 to 150 dB [*64*].

2.3 Detecting Human Vital Signs behind Obstacles

This research will address the problem of human being detection behind obstacles. In order to solve the human detection problem, consideration must be given to a method for detection of human breathing, detection in realistic conditions including clutter removal, estimation of accurate range and the number of targets, and estimation of human posture. In the following section the issues (denoted by letter P followed by a number) that need to be solved in order to detect the human being behind walls will be presented.

2.3.1 Detection of human breathing (P1)

The human chest displacement, caused by breathing, is between 10 and 20 mm, and the heartbeat causes a displacement ranging between 0.2 and 0.5 mm [*6*,*21*]. When a human target is illuminated by electromagnetic wave, the reflected wave will be modulated by the quasi-periodic movement of breathing and heartbeats. The reflected wave from the target is generally weak and the changes of amplitude may be negligible. Therefore only frequency, phase and arrival time can be used for the detection of the movements due to breathing and the heartbeats. NBCW radars detect the displacement of the human chest and the heartbeat by detecting the phase variation in the reflected signal [*49*,*65*,*66*,*67*]. UWB radars use the time of arrival to detect the human chest and the heartbeat displacement [*5*,*10*,*11*,*23*,*50*,*68*,*69*,*70*]. Phase variation and time of arrival estimation encounter many challenges which include: small movements, low received SNR, high clutter from the wall and other objects in the room, high attenuation of the electromagnetic wave in the human body, and antenna coupling. Furthermore, the large-scale displacements of the human body may be a challenge in human breathing detection and rate estimation [*30*]. Also, the large error in the estimated human breathing rate may be because the second breathing harmonic is higher than the first one in some scenarios.

2.3.2 Clutter Suppression and Detection in realistic conditions (P2)

When human breathing is being detected behind a wall, the reflected signal is a combination of reflected signals from the human being, stationary clutter, non-stationary clutter and narrowband interference [*24*,*26*].

The stationary clutter depends on the material of the walls and the objects inside the room. In some scenarios, the clutter is homogeneous and reflectors are not composed of multiple materials. In other scenarios, walls are composed of different materials and the clutter is heterogeneous and the electromagnetic propagation velocity is not the same in the whole scanning field. This will drift the target's estimated position from its real location.

2.3.3 Estimation of the number of targets (P3)

The received signal may be composed of multiple signals received from multiple targets. Estimating the number of targets that are behind the wall is more problematic than single target detection. When two targets are in the same detection area, the micro-Doppler signature will be composed of the movement activities of these two targets. High resolution radars can distinguish between these targets. When there are more than two targets, the problem of differentiating between the targets becomes more difficult. Two or more receivers and transmitters have been used to distinguish between multiple targets [*71*]. However, distinguishing between multiple targets using a stationary monostatic UWB radar system is more problematic and needs more advanced techniques. Estimating the number of targets and the respiration rate for every target is an open research area.

2.3.4 Detecting the posture (P4)

Posture estimation can be used in non-contact monitoring of vital signs in long-term monitoring of elderly as in home-care where multiple subjects may be monitored independently [*39*,*40*,*44*]. If we can estimate the human posture, we can detect fallen people on the ground/ floor. Furthermore, posture estimation provides a prediction of the best scenario for breaking into a designated area in secuirity applications and rescue operations. It helps to determine how many people are standing, sitting, or lying in the dorsal decubitus position.

2.4 Literature Review on Human Being Detection Behind Walls

In this section, a literature review is presented on using NB and UWB technology in human breathing detection behind walls. Attention will be also given to radar systems specifications such as: center frequency, bandwidth, dynamic range, and maximum range, and the methodology that has been used to detect human breathing behind walls. Later Chapter three will focus on further analysis of the algorithms that have been used to address the human breathing detection problem.

The initial attempt at using microwave systems to sense physiological movements remotely behind an obstacle was in 1990 [*2*]. The first attempt of using the UWB radar in medical applications for human body monitoring and imaging was in 1993 [*53*]. In March 1996, Ross developed a new class of electronic scanning radar system (ESR) for particular application to intrusion detection using UWB transmitters [*72*]. In the same year, the US Patent, 5,573,012, in remote sensing was awarded [*54*]. By 1999, many studies have been done for UWB medical applications like detection of respiration rate.

In 2011, the radar detection method for targets behind corners was introduced. If two or more paths are not in the same range cell, multipath effect can be removed. DFT was used to detect the moving target [*73*]. In the same year, Lui used the same approach to detect a target using DFT or STFT combined with SVD approach [*12*].

DFT and STFT have been used to detect the respiration rate of the target in a specific range-bin [*12*,*13*,*24*,*33*]. In 2012, a method was introduced to detect the breathing of a human behind walls using 2D-DFT or STFT [*13*]. Wavelet transforms have been used to detect the human breathing frequency [*6*,*27*,*28*]. In 2012, a wavelet-based strong clutter removal technique for UWB life detection using DWT was proposed and 8 dB increases in SNR were achieved [*28*].

The human detection challenge requires research not only in human breathing detection but also in several signal processing fields including range estimation, noise and clutter suppression and estimation of the number of targets.

I. Immoreev used range gating to eliminate interference and clutter reflections [*74*]. Range gating may not be precise enough to remove clutter and noise. Singh and Maaref used SVD to suppress clutter and noise [*24*,*25*]. They detected a human standing 2.3 m from the radar and breathing behind a 30 cm gypsum wall, 20 cm brick wall, and a 20 cm concrete wall. They claimed that the clutter will be in the first singular value of the diagonal matrix. However, we found that the clutter may extend beyond the fifth principal component. Tivive showed in his results that the target reflections are not always in the second singular value [*75*]. A. Nezirović estimated which singular value contains the target information by using a threshold based decision method and detected human breathing inside a sewer pipe of 10 cm concrete thickness [*26*]. The experiments were performed in an environment that does not correspond to realistic conditions. Amin used the moments of the statistical distributions of the reflected signal amplitude to measure the contrast in radar imaging [*76*]. The SVD method works well in both indoor and outdoor environments when identifying which principal component contains the target reflections.

The SVD method can be used in clutter suppression and discrimination between multiple targets [*14*,*15*]. The SVD combined with the STFT method has been used to detect human breathing behind different types of walls and to discriminate between two targets [*12*,*15*]. However, SVD combined with STFT didn't give good results in detection behind concrete walls. In 2012, Y. Li proposed a method to discriminate between two targets standing in free space and behind an obstacle [*32*]. He used an IR-UWB radar system transmitting pulses with peak power equal to 5W. An adaptive filtering method was used to remove the interference and distinguish the second target from the first target. Discrimination between multiple targets breathing behind walls is still an open research field.

In 2011, Dwelly introduced a method to distinguish between human and non-human targets. The method can estimate what a human is doing. The method is based on detecting the breathing rate, heart beat rate, and any other movement, and use these parameters as input to a neural network [*39*]. Human posture estimation under LOS and NLOS conditions is also still an open research field.

Table 2.3 surveys the problems that were addressed in the literature on human breathing detection behind walls, as presented in Section 2.3 above. The references [*10*,*11*,*15*,*24*,*32*,*61*] are the most relevant to our work. However, none of them addressed the four problems which are presented in Section 2.3.

From the table, it is obvious that P4 is an open-research area with a small number of contributions. P1, P2, and P3 have been researched by a number of researchers. However, many questions have not been addressed by the state of the art. Some of these questions include: why the error in the estimated breathing rate still high compared with the real breathing rate in some scenarios, why the second breathing harmonic is higher than the first harmonic in some scenarios, which principal component contains the target information when SVD is used in clutter suppression, and what is the suitable threshold that can detect targets and reject clutter. This thesis addressed all of these questions. The choice of solution may involve optimizing engineering trade-offs between conflicting requirements of radar systems, the ability to determine distance, and to estimate the breathing rate. A detailed survey of the state of the art for using NB and UWB technology in human breathing detection behind walls is in Appendix B.

Table 2.3 Survey of the problems that were addressed in the literature on behind the wall detection (problems P1 – P4 are described in Section 2.3).

Reference	P1	P2	P3	P4
[*2*]	X			
[*5*]	X			
[*7*]	X			
[*9*]	X			
[*10*]	X	X		
[*11*]	X	X		
[*12*]	X	X		
[*13*]	X	X		
[*15*]	X		X	
[*22*]	X			
[*24*]	X	X		
[*32*]	X			X
[*38*]			X	
[*39*]	X	X	X	
[*46*]	X			
[*49*]	X			
[*50*]	X			
[*60*,*61*]	X	X	X	
[*62*]	X	X		
[*65*]	X	X		
[*67*]	X			
[*68*]	X	X		
[*69*]	X	X		
[*70*]	X	X		
[*128*]	X			
[*129*]	X	X	X	
[*130*]	X		X	
[*131*]	X		X	

2.5 Analysis of Human Breathing Detection Behind Walls Radar System Requirements

In this section, Sections 2.2, 2.3, and 2.4 are summarized in order to present the most suitable requirements for this research's radar system. The radar systems used to detect human breathing, transmit electromagnetic waves with power form 0.1 mW to 5 W. However, the United States Federal Communication Commission (FCC) mask for UWB is - 41.3 dBm / MHz in the frequency ranges from 3.1 to 10.6 GHz, and is 15.209 dBm / MHz below 960 MHz. The typical average radiated power, integrated over the band of interest may be in the order of mWs [*33*,*55*,*62*]. Recently, Narayanan used UWB Radar with transmitted power of 0.316 mW to detect a human breathing behind a wall. The radiated power spectral density of this short distance radar system is -3 dBm / MHz and -22 dBm / MHz at outputs with and without the power amplifier, respectively, which are much lower than the FCC limit [*61*]. Increasing the transmitted power cannot be used as a solution to the detection problem. However, we can increase the received SNR by integrating a number of the received pulses. By integrating 512 of the received pulses, SNR will be increased by 27.01 dB. The attenuation of the transmitted signal depends on the material of the wall, bandwidth of the transmitted signal, and the central frequency. The operating frequency from 1.6 to 2.4 GHz or from 3 to 4 GHz gave good penetration characteristics [*67*,*64*]. The radar cross section of a human target has its highest value in the frequency range from 3 to 4 GHz [*25*]. Also, it was found that a bandwidth above 2 GHz and having center frequency from 4 to 6 GHz, results in highest SNR values [*23*].

Detecting a human standing 1~5 m behind a 30~50 cm thick wall is realistic in some scenarios. The operating range of the radar will be around 20 m. The dielectric constant of different materials in the walls is the main factor that controls the amount of power reflected from or transmitted through this barrier. A higher dielectric constant results in higher wall reflectivity. Wet brick and concrete have the highest dielectric constants. The receiver operating characteristics (ROC) curve in [*60*] shows the lowest probability of human detection when a person is standing behind a wet brick wall.

Table 2.1 illustrates that the pseudo-random UWB technology is the most suitable technology for this application. It is a widely available technology, inexpensive, immune to narrowband interference, and has the ability of range gating. Based on information previously presented in Section 2.2, it is apparent that a radar system that transmits UWB pulses with a center frequency from 3-4 GHz is required to achieve penetration characteristics and bandwidth 500 MHz or higher for high range resolution. The radar system should have the ability to integrate a high number of the received pulses in order to increase the received SNR. Many radar systems with these characteristics have been used in the state-of-the-art [*24*,*57*,*58*,*59*,*60*,*61*,*68*,*69*,*77*,*78*]. In this thesis' research, it was observed that the PN-UWB P410 radar (Fig. 2.1) produced by the Time Domain company, Huntsville, USA, guarantees the radar system requirements in center frequency, bandwidth, human chest displacement detection, and received SNR. The PN-UWB P410 radar system is described in details in Appendix C.

Figure 2.1 P410 UWB impulse radar [*79*].

2.6 Data Collection

Table 2.4 summarizes the main specifications and the key performance parameters of P410 radar [*79*]. While operating the radar, the time of starting and ending scans was set. The P410 radar receives the reflected waveform in range-bins. Each rang-bin is 1.907 ps. The time difference between starting and ending scan (scan time) must be an integer number of range-bins. The Monostatic-Radar-Module (MRM) produces a radar scan using several samplers acting in parallel as a rake receiver. Because of this architecture, the scan time must be in even multiples of 5859.36 ps. This value is called quanta. If the user requests a fraction number of the quanta, the scan stop will be rounded to the nearest quanta integer value. The rack receiver scans one quantum in 0.792 μs. The radar will collect the scans continuously or in a specified number of scans.

Table 2.4 The main specifications and the key performance parameters of P410 radar [*79*].

Specification	Value
Power:	
Maximum Power Consumption	3.9 Watts
User Interfaces/Devices:	
Standard PC/Laptop Interface	USB 2.0A Client – Micro-B connector
RF Characteristics:	
Operating Band	3.1 GHz to 5.3 GHz
Center Frequency	4.3 GHz
Transmit power (Adjustability range) (-14.5 dBm is FCC Part 15)	Standard: (-31.6 to -12.64 dBm) High power: (-14.5 to 0.7 dBm)
Antenna Ports A&B	Standard 50 Ohm SMA coaxial connector
Ranging Performance:	
Ranging techniques	Pulsed Two-Way Time-of-Flight (TW-TOF), Coarse Range Estimation (CRE)

The amplitude received in the range-bins in each scan is collected using an Excel file, in the horizontal direction, and the scans are collected in the vertical direction. The number of scans is 3000 and the time of each scan is 20 mseconds The time of each scan can be determined from the following formula:

$$Scan\ time\ (\mu s) = n_q \times 0.792 \times 2^{PII} \tag{2.3}$$

where n_q is the number of quanta in a scan, and PII is the Pulse Integration Index. The PII was set to equal 12. This increases the SNR of the received signal by 36.12 dB. Also, the number of quanta was set to 5 to in order to have a maximum range of 4.38m. The scan time was 16.22ms. The time interval between each scan was set to 3.78 ms to keep the scans from overlapping. The total scan time is equal to the number of scans multiplied by the time of a full scan which is equal to 3000×20 msec =1 min. Figure 2.2 shows how the P410 UWB collected the data in a data matrix X. The yellow cells are the range-bins in the fast time direction, the slow time direction represents the scans direction, and the orange spaces illustrate the time interval between each scan.

Time Domain Company introduces P410 Radar with Monostatic Radar Module Reconfiguration and Evaluation Tool (MRM RET). If MRM RET is not connected to the MRM Server, then the reflected waveform (range profile) can be saved in data file without any pre-processing. If MRM RET is connected to the MRM Server, then it is possible to select the type of filters to be employed and the selected filter data streams can be displayed in the Scan Tab or logging to a .csv file. In all of the measurements the MRM service was turned off. The raw scan data was collected, and then, the method of detection was applied. The data was collected in a .csv file and a MATLAB was used to code and simulate our algorithm.

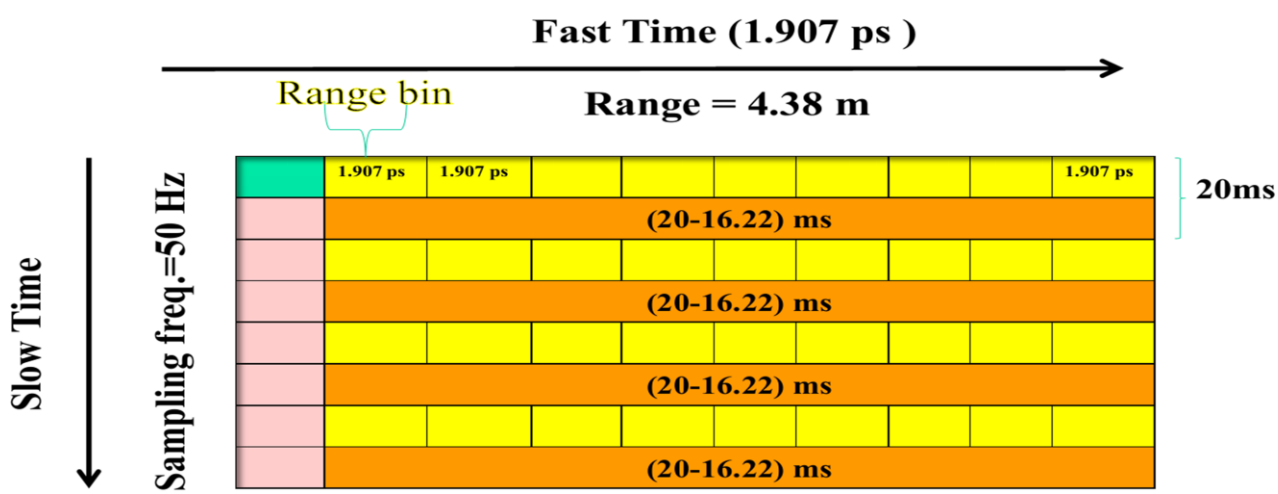

Figure 2.2 P410 data collection.

Chapter 3

State-of-the-Art in Human Breathing Detection Signal Processing

3.1 Introduction

In Chapter two, a comparison was made between different UWB radar systems and it was observed that the PN-UWB radar is suitable in human breathing rate estimation from behind obstacles. Also, problems that have to be solved in human breathing detection behind obstacles were noted and a review was given on the state-of-the-art in solving these problems.

In this Chapter focus is solely on signal processing algorithms developed to solve these problems. The state-of-the-art in signal processing, shortcomings of the state-of-the-art, and the reasons for using the proposed methods for each block in Fig. 3.1, are presented.

3.2 Human Detection and Breathing Rate Estimation System

In this section, this research's detection and breathing rate estimation system block diagram is provided. The reason for presenting the block diagram is to identify the main signal processing parts. Also, the background for some different algorithms that are available in the-state-of-the-art is presented. In the following sections, a review of common algorithms for each part is described.

The detection and breathing rate estimation system consists of five main parts which are: pre-processing algorithm, clutter suppression, range estimation and multi-targets discrimination, breathing rate estimation, and posture estimation. Figure 3.1 is a block diagram of the specific detection and breathing rate estimation system. The collected data is filtered in slow time and fast time direction by applying the cleaning algorithm. The output of the cleaning algorithm is applied to the clutter suppression method. After pre-processing and clutter suppression, the range estimation and multi-target discrimination algorithm is applied to detect targets and estimate the range. The output of the cleaning algorithm in a range-bin containing a target is applied to the breathing rate and posture estimation algorithms. The algorithms will be discussed in Chapters four, five, and six.

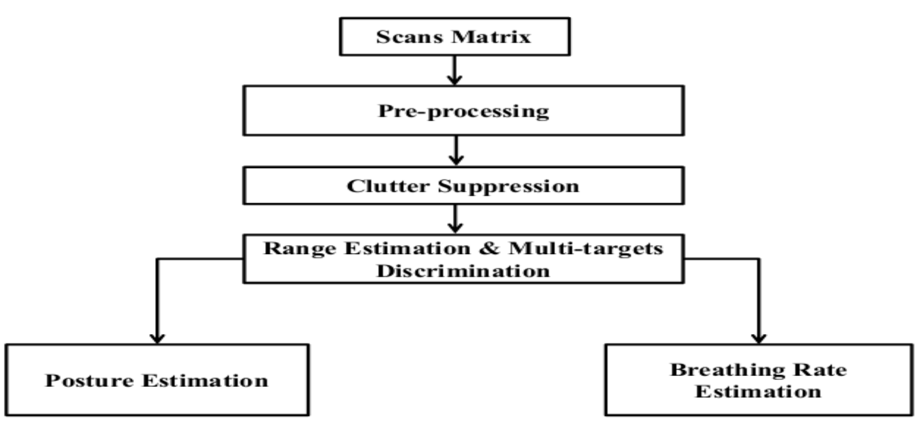

Figure 3.1 General block diagram of target detection and breathing rate estimation algorithms.

3.2.1 Clutter Suppression

Although clutter and unwanted frequencies have been removed from the data matrix X by applying the pre-processing algorithm, it has been recognized experimentally that the breathing signal in the slow time direction still has a part of the energy of the clutter and AWGN that need to be removed [*26*]. Range gating has been used to eliminate clutter and noise reflections [*74*]. However, clutter range information may not be known and range gating may not be precise in all scenarios. SVD has been used to suppress the residual clutter and noise from the human breathing signal received in UWB radars [*24*,*26*,*75*]. The SVD is applied to the Discrete Fourier Transform (DFT) of the data matrix after applying the pre-processing algorithm. In [*24*], the human breathing detection has been done by applying SVD to the DFT of the data matrix, removing the first singular value, finding inverse SVD, and looking for the presence of the human breathing by visual inspection of the plot of the DFT magnitude against the frequency axis. If a high intensity has been observed in the human breathing rate range, a target is detected at that range [*24*]. In [*15*], a non-linear threshold has been used to detect human breathing and the threshold value depended only on the distance between the radar and the target. In [*26*], Nezirović, in his PhD thesis, developed the Respiratory Movement Detection (RMD) algorithm which is proposed in [*46*] to detect human breathing. Nezirović published his work in [*10*,*11*,*23*,*80*]. Figure 3.2 shows the flow chart detailing the steps in the developed RMD algorithm [*26*]. The algorithm can be divided in four main steps:

- Stationary clutter suppression.
- Filtering in fast time direction.
- Applying DFT and using SVD to remove residual clutter and noise.
- Applying a threshold to decide which singular value contains the target information.

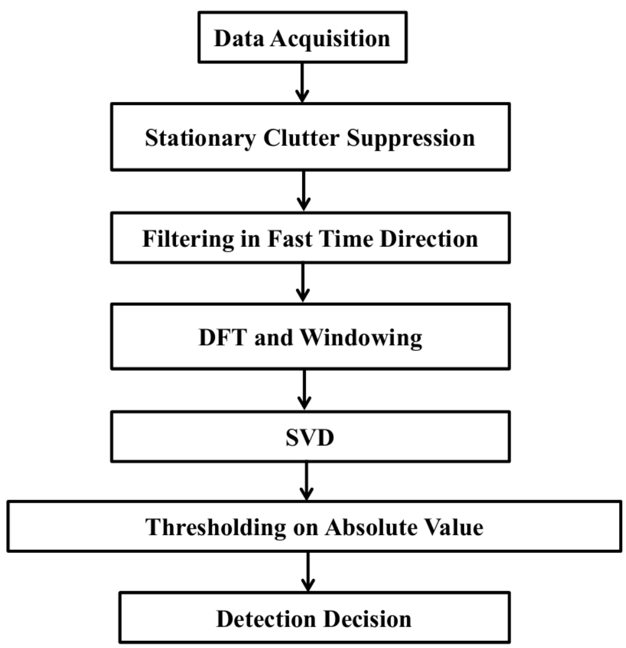

Figure 3.2 The developed RMD algorithm presented in [*26*].

The assumption is that the waveforms reflected from clutter and targets are collected in a data matrix X like that is shown in Fig. 2.2 with number of scans M and number of range-bins N.

In the first step, Nezirović applied the Linear Trend Subtraction (LTS) method to remove the stationary clutter. After the stationary clutter suppression, a Finite Impulse Response (FIR) was applied to every range profile to remove the high frequencies in the fast time direction and the output of the filtering process at the range-bin n in the fast time direction and the time index m in the slow time dimension will be $\tilde{Y}_{LTS}(m,n)$ where $[\,\tilde{.}\,]$ denotes the filtered data matrix and Y_{LTS} is the output of the LTS method. After filtering, the DFT is applied to the slow time dimension and a window in the human breathing frequency range is applied to filter out the frequencies out of the band of the human breathing range. Nezirović assumed that the human breathing frequency may appear in $M^* - m^* + 1$ number of DFT points of the signal in the slow time dimension.

The human breathing frequency range is from m^* frequency bin to M^* frequency bin where, m^* and $M^*$are the lowest and highest frequency bins of the human breathing frequency range for the DFT of the breathing signal, respectively. A $M^* - m^* + 1$-sized rectangular window was applied in the frequency domain and the output can be presented as:

$$Y_{DFT}^{W}(\nu,n) = W(\nu,n) \times DFT\{\tilde{Y}_{LTS}(\nu,n)\}, \quad \nu = \{m^*, m^*+1, \dots, M^*-1, M^*\} \tag{3.1}$$

where, $Y_{DFT}^{W}(\nu,n)$ is the windowed DFT of the filtered data matrix $\tilde{Y}_{LTS}(\nu,n)$ and $W(\nu,n)$ is the $M^* - m^* + 1$-sized rectangular window. SVD is applied to remove clutter and noise in Y_{DFT}^{W}, where Y_{DFT}^{W} is a matrix has $M^* - m^* + 1$ rows and N columns. Equation 3.2 is the decomposition of matrix Y_{DFT}^{W} to the orthonormal basis for the slow time vectors U, the orthonormal basis for the fast time vectors V, and the singular values matrix S using SVD.

$$Y_{DFT}^{W} = \sum_{j=1}^{N} U S_j V^T \tag{3.2}$$

where $j \in \{1, \dots, N\}$, S_j is a matrix have the same size as S and all elements are zero except $S(j,j)$.The majority of the energy from the human breathing signal is expected to be in one singular component in the matrix S. The singular matrix, or decision matrix, can be presented by:

$$Y_{DFT\,j}^{W} = U S_j V^T \tag{3.3}$$

The critical part in the algorithm is the threshold-based detection and classification. In [*24*], Singh assumed that the clutter information would be in the first singular value. The breathing detection is performed by applying SVD to the matrix Y_{DFT}^{W} , removing the first singular value in matrix S, inverting SVD, and detecting the target by visual inspection. However, the research for this thesis found that experimentally the clutter may extend to the second, third, fourth, or fifth singular value. Also observed experimentally was a high number of false alarms by using the algorithm proposed in [*24*]. In [*75*], Tivive concluded his work to the same result; the target information is not always in the second singular vector of a B-scan matrix. In [*14*], Zhang divided the signal in the fast time direction into 22 time segments and determined the STFT of the signal in each range-bin. Then he applied a threshold decision based on the power of the spectral peak in a specific segment and the mean power in all segments to detect the human breathing. However, he did not use the SVD and the residual clutter and noise in the data matrix may block the human breathing detection. SVD technique resulted in a high performance for human breathing detection behind walls [*24*,*26*,*75*]. However, deciding which singular value contains the target information is the key for success or failure of the detection algorithm. Nezirović applied a constant false alarm threshold on each decision matrix. The threshold value can be determined using the following equation [*26*]:

$$\gamma_j = -\lambda_j . \frac{2.log(\frac{P_{fa}}{J})}{\pi.\sqrt{N.M^*}} \tag{3.4}$$

where γ_j is the threshold value assigned for the j^{th} decision matrix, λ_j is the j^{th} singular value, P_{fa} is the false alarm probability value, N is the number of samples per range profile, and J is the number of the singular values. The assumptions are the following: there is one target that stands behind a wall or is buried under rubble, immobile, resting in horizontal position, and breathe normally. Nezirović assumed working in an environment that introduces some sort of control on the non-stationary clutter sources which means there is no object in the area of the experiment except the subject under test. In some scenarios, the magnitude of the clutter in the windowed data matrix Y_{DFT}^{W} may exceed the magnitude of the human breathing signal and false alarms may be detected. Sometimes, the maximum magnitude in a decision matrix ${Y_{DFT}^{W}}_j$ exceeds the threshold γ_j in the absence of a target. We propose in Chapter 4 a method that does not require prior knowledge of which principal component contains the target information.

3.2.2 Range Estimation

In the previous section, we discussed target detection using SVD and threshold-based decision. Once, a target has been detected in a decision matrix D_j, the target range-bin n^* will be estimated according to [*26*]:

$$n^* = arg\, max_{m \in M}\{\left|Y_{DFT}^{W}\left(m, arg\, max_{n \in N}\{\left|Y_{DFT}^{W}(m,n)_j\right|\}\right)_j\right|\} \tag{3.5}$$

and the range r^* will be estimated according to:

$$r^* = \frac{n^* \cdot t_s \cdot C}{2 \cdot \sqrt{\epsilon_r}} \tag{3.6}$$

where, t_s is the sampling time in the fast time direction, C is the speed of the light in free space, and ϵ_r is the relative permittivity of the wall materials. The reflections from the human body and the surrounding objects may contribute instructively or destructively resulting in the maximum reflected energy to be drifted from the real target position. However, the distribution of the magnitude squared of the received signal is studied, and the target may be detected in its real position. If the third moment value of the distribution of the received signal changes abruptly where the target is, the first point where the electromagnetic wave reflects from the target can be recognized.

In 1991, neural network classifier was used to discriminate between different probability distributions of radar return signals [*81*]. L-band coherent radars had been used to collect the data. It was found that the degree of deviation for the received signal magnitude distribution from the Gaussian distribution can be used as a feature in target classification. The skewness and kurtosis were used as a measure of the Gaussianity for the received waveforms when making classification decisions. Falconer used Pulsed-Doppler microwave radar working in the UHF band to discriminate between human activities and non-stationary targets by studying the kurtosis of the Doppler [*82*]. Chest wall motions had high kurtosis values and its statistical distribution tended to be more exponential than Gaussian [*82*]. Rayleigh, K-, and Weibull distribution was proposed for clutter in [*83*] using X-band radar. Stationary clutter range profile magnitude squared was presented as a Lognormal, Weibull, or exponential distribution. Non-stationary clutter or moving targets were presented as a Lognormal, Weibull, Rayleigh or chi-square distributions in [*81,84,85*]. Kurtosis was used to remove the foliage swaying and as a feature to discriminate between non-stationary clutter and targets [*84*], while higher moments were used to measure pixel contrast in human behind wall imaging and to reduce the error in position of the target [*76*]. Table 3.1 summarizes the different models of clutter and different types of targets.

Table 3.1 Different models of clutter and different types of targets

Index	Reference	Data Input	Modeling Purpose	Clutter Model	Target Model
1	[*81*]	The magnitude for sequence of radar returns	Distinguish between several major classes of radar returns including weather, birds, and aircrafts.	Not specified. The skewness and kurtosis of the received signal were used to distinguish between clutter and targets.	
2	[*82*]	The received waveform amplitude	Distinguish between clutter and human breathing	Normal distribution	Exponential distribution
3	[*83*]	Raw data for the received signal	Measure matching between the clutter spectral density and the exponential model	Rayleigh, K-, and Weibull distributions. Clutter PSD is well approximated with the exponential model	Not specified
4	[*84*]	The received energy.	Distinguish between the non-stationary foliage and human breathing	Normal distribution	Chi-square distribution
5	[*85*]	The squared magnitude of the received waveform	Find general models for clutter and targets	Chi-square , Weibull, Rayleigh, and Log-normal distributions	Chi-square , Weibull, Rayleigh, and Log-normal distributions

In this research, the SVD is applied with a novel method and the skewness of the amplitude squared of the correlator output is used to discriminate between clutter and human breathing. The method estimates which singular value contains human breathing information and accurately estimates the range regardless of the material used in the walls.

3.2.3 Multi-Target Discrimination

Multi-target discrimination is affected by clutter, antenna coupling, noise, and the interference generated from the multipath reflected from the nearest target to the antenna [*32*]. In security applications and rescue operations, it is desirable to discriminate between multiple targets separated with a distance less than 1m [*32*]. Zahang introduced a method to discriminate between multiple targets using PN-UWB radar. He used the STFT and non-linear threshold method to discriminate between two targets [*15*]. However, the nonlinear threshold value depends only on the distance and many false alarms may be detected [*15*]. Li proposed a method to discriminate between two targets using DFT and S transform [*13*]. However, he discriminated between multiple targets by visual inspections. Clutter and antenna coupling may block the discrimination between multiple targets in some scenarios. Also, the signal reflected from the first target may reflect from another obstacle and arrive at the same time as the signal reflected from the second target to the receiving antenna. The reflected signal from the second target will be composed of the two signals reflected form the first and the second target. To detect the second target, we have to remove the signal of the first one. The clutter suppression and the removal of the nearest target to the antenna interference were not addressed in [*13*] and [*15*].

In 2012, Li proposed a method to discriminate between two targets standing in free space and behind an obstacle. He used an IR-UWB radar system transmitting pulses with peak power equal to 5W [*32*]. First he applied a LPF to each range profile for smoothing and removing AWGN. Second, in order to remove the clutter, he subtracted the mean from every range profile. Then he applied lowpass FIR filter to the slow time direction to remove the high frequencies from the band of the human breathing frequency band. The output of these three steps is a matrix $W = (w_1\ w_2\ \dots\dots . w_M)$ where, w_i is the received signal along the slow time direction and M is the number of the vectors in the slow time direction. The power spectrum of the received signal in each vector w_i can be determined by calculating the variance of this vector. The maximum variance value refers to the range-bin which contains a target. The magnitude of the power spectrum around 1m is taken as the threshold to detect a target in range-bins beyond the 1m range. However, the antenna coupling effect may make the threshold value high in a way that the target power spectrum value may fall under the threshold. Li used an adaptive method to detect and discriminate between the two targets. The additive cancelation method is used here to remove the interference of the first target in the range-bins behind the target's range-bin. Figure 3.3 is the block diagram of the additive cancellation method used in [*32*]. Assume that $x(n) = d(n) + A \cdot u(n)$, where $x(n)$ is the primary input which contains the second target breathing signal and the interference, $d(n)$ is the required signal, A is the amplitude of the interference, and $u(n)$ is the normalized interference. Also, the reference input $y(n)$ which contains the interference (the first target breathing signal) is presented as amplitude B multiplied with the normalized interface.

$$y(n) = B.u(n) \tag{3.7}$$

The reference input of the additive cancellation, which is here the breathing signal for the first target, is used to remove the interference from the signal $x(n)$ by using the means of the LSE algorithm.

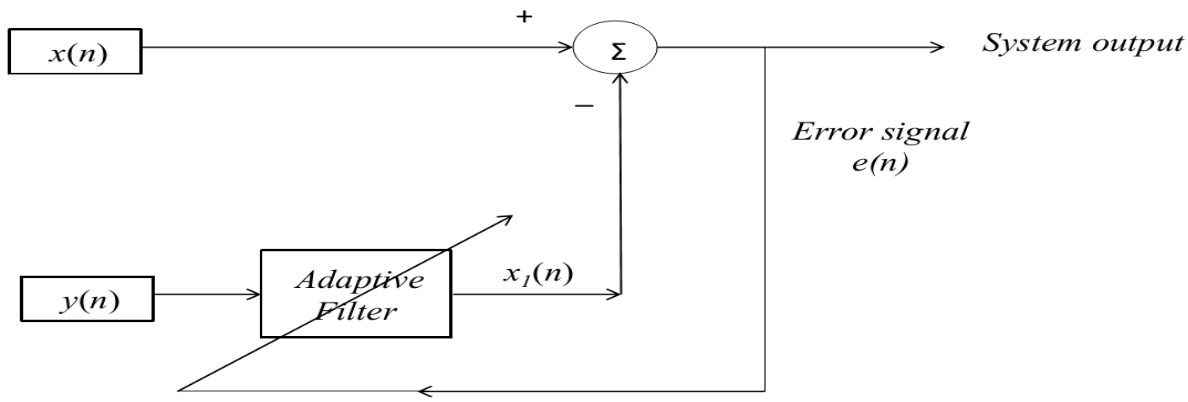

Figure 3.3 Additive cancellation method [*32*].

$$x_1(n) = \sum_{i=1}^{N-1} \widehat{\omega}_i(n)\ y(n-i) \tag{3.8}$$

$$e(n) = x(n) - x_1(n) \tag{3.9}$$

$$\widehat{\omega}_i(n+1) = \widehat{\omega}_i(n) + \mu u(n-i)e(n),\ i = 0,1,\dots,N-1 \tag{3.10}$$

where N is the order of the filter, μ is the step size parameter, and $\widehat{\omega}_i(n)$ is the tap weight [*32*]. The algorithm succeeded in discriminating between two targets separated 0.4 m in free space. However, it failed in discriminating between two targets separated less than 0.6 m and standing behind a 24 cm thick brick wall. In this research, a novel method is proposed that can be used to discriminate between two targets separated by 0.3m and standing behind a 20 cm gypsum wall. Although the algorithm in [*32*] can remove the interference generated from the first target, the algorithm has two drawbacks. First, the mean subtraction method is not enough to remove clutter and noise. It is suggested the SVD technique be used to remove the residual clutter and noise. Second, the method depends on the accuracy of estimating the first target range-bin. An option is to use proposed SVD combined with the skewness method to estimate the first target range-bin.
This research's proposed method can be used separately to discriminate between multiple targets or can be used to enhance the performance of the algorithm suggested in [*32*] by estimating the accurate first target's position. If the first target position is estimated in its real position, the signal in this range-bin can be used as a reference to remove the interference generated from the first target.

3.2.4 Breathing Rate Estimation

DFT and STFT have been used to detect the human breathing in a specific range-bin [*12*,*13*,*24*,*33*] and to estimate the human breathing rate using UWB radars [*35*,*86*,*87*]. Recently, many FFT-based estimators detected the breathing on the basis of the spectrum analysis of the breathing signal [*36*,*37*,*38*]. Extraction of non-stationary physiological signal in noisy environment is problematic. It is necessary to analyze individual events (human breaths) from the point of view of the time intervals between each breath constraint by inspecting the time interval between each breath in time domain. In general, the existing technology does not take into account the physiological properties of individual breath pulses. In 2011, Rosenbury invented a handheld instrument capable of measuring breathing and heartbeat motion at a distance [*38*]. He used filters and spectrum analysis to remove noise and detect the breathing frequency. However, properties of human breathing signals were not taken into account. In 2013, Mohamadi introduced an invention on determination of hostile individuals armed with weapon, using respiration and heartbeat as well as spectral analysis at 60 GHz. A number of radar units were configured to provide scan data samples to a network. The algorithm relies on frequency analysis and uses the DFT of the received signal in the slow time dimension to estimate the breathing rate. The individual features of reflected signal, e.g. duration between breaths pulses were not taken into account for noise discrimination [*88*]. Wiesner invented a method and a system for detecting vital signs of living bodies [*89*]. This method relies on the frequency analysis (DFT) analysis.

The large-scale displacements of the human body while breathing have a frequency spectrum that overlaps with the human breathing frequency range. Also, in some scenarios, the magnitude of the second harmonic of the breathing signal may have a magnitude higher than the first one. For accurate breathing rate estimation, the effect of the human body large-scale displacements needs to be reduced and the first human breathing harmonic must be kept while removing the other breathing harmonics. In [*90*], the human body breathing rate has been estimated using body worn UWB radar where the transmitter and the receiver is placed very close to the human wall chest. Maximizing the periodogram has been used to estimate the breathing frequency. A downside of the periodogram method is its limited capability to capture the respiration dynamics [*91*].

Baboli used a wavelet algorithm for estimating breathing rate using UWB radar [*27*]. The method estimates the range-bin that contains the maximum energy in the human breathing rate and applies DFT to the signal in that range-bin. Human body large-scale displacements and the breathing harmonics frequency range overlap with the human breathing range and the incorrect magnitude peak may be chosen as the estimated breathing rate using DFT. The human body displacements and breathing harmonics should be considered while using wavelets in human breathing rate estimation application.

Narayanan discriminated between the movements behind the wall of the human chest and the arm or the wrist using a Doppler radar system with Empirical Mode Decomposition (EMD) followed by the Hilbert spectrum [*34*]. Many Intrinsic Mode Functions (IMFs) will have a frequency spectrum in the range of the human breathing frequency range and it is difficult to decide which of these IMFs is related to the human breathing activity.

Lazaro proposed techniques for clutter suppression in the presence of body movements during the detection of breathing activity through UWB radars [*29*]. The movements of the human body are detected by computing standard deviation of the signal amplitude in a 4 seconds moving window. If the standard deviation is higher than a threshold, it is considered to be human body movements and is not considered in the breathing rate estimation. For breathing rate estimation, the Lomb periodogram has been used to estimate the rate. Lazaro observed that sometimes the second harmonic is higher than the first harmonic which makes the estimation of the breathing rate difficult in some scenarios [*29*].

Li proposed two methods to reduce the effect of the human body large-scale displacements [*30*]. Li used the moving average filter and the ellipse fitting methods to track the mean of the signal in a sliding time window. Subtracting the mean from the breathing signal will reduce the effect of the non-breathing displacements. However, these methods are sensitive to the time window size.

In the following, three estimators in the application of human breathing rate estimation are studied in both free space and behind the walls.

3.2.4.1 FFT-Based MLE Estimation

The Maximum Likelihood (ML) frequency estimator of the observed signal $y(t,\tau)$ will be [*92*]:

$$\hat{f}_{ML} = arg \underbrace{max}_{f \in F} \; |Y(f,\tau)| \tag{3.11}$$

where, $F \subseteq [0,\infty)$, $Y(f,\tau) = \int_{-\infty}^{+\infty} y(t,\tau) e^{-j2\pi f t} dt$. Usually, the FFT is used to compute $|Y(f,\tau)|$ using Q number of FFT points and then using Eq. 3.13 to find the point q that has a maximum magnitude value where, $q = 0, 1, 2 \dots, Q-1$. The estimation of the breathing frequency $\hat{f}_b$ will be equal to $\frac{q}{QT_s}$, where T_s is the sampling time in the slow time direction.

3.2.4.2 Mean Tracking of the Human Breathing Signal

Li found that the large-scale movements of the human body while breathing may also have a significant effect on the human breathing estimation process [*30*]. Narayanan discriminated between the breathing and wrist movements using the Empirical Mode Decomposition (EMD) [90]. He assumed that the breathing signal was a sine wave signal and based on that assumption, the IMF related to the breathing signal can be defined.

The MLE method proposed in Section 3.2.4.1 may be used to assign the Intrinsic Mode Function (IMF) that contains the breathing frequency. In summary, to estimate the human breathing rate accurately using EMD technique, a method to assign which IMF contains the breathing frequency is required.

The effect of the large-scale body displacements can be reduced by subtracting the mean from the target reflected signal. Moving average filter and ellipse fitting methods were used to reduce the effect of the large-scale displacements to estimate the breathing rate [*30*]. The moving average filter method computes the mean of the breathing signal in a time window and subtracts the mean from this signal. In the ellipse fitting method, the breathing signal is represented in a cluster of two dimensional data. The two dimensional data was obtained by using a self-delayed version of the target reflected signal. This method used a low degree of a freedom ellipse model to fit the two dimensional data. An attempt was made to track the mean of the signal by using this method. After that, the mean is subtracted from the breathing signal [*30*]. A drawback of these methods is that the performance of human breathing rate estimation depends on the time window size used in the mean tracking algorithms. The best noted performance was when the window size was equal to the time interval of one breath. However, ellipse fitting algorithm has shown a better performance in different time windows [*30*].

To study the performance of the methods in Sections 3.2.4.1 and this Section in human breathing rate estimation behind walls, 18 measurements were collected from a human breathing normally at a breathing rate of 18 breaths/min. The target was standing, sitting, and lying down 1.5 m away from the radar and behind a 20 cm thick gypsum wall at different angles (0, 30, 60, 90, 135, 180 degrees) relative to the transmitter and receiver antenna plane. The pre-processing algorithm presented in Chapter four was applied and the proposed range-bin estimation based on

SVD was applied along with the skewness method. Finally, the FFT-MLE, moving average, and ellipse fitting methods were applied to the correlator output at the estimated range-bin. The moving average and ellipse fitting methods were applied to a window length of the correlator output equal to 1.5 seconds and the total observation time of the signal was 40 seconds. A comparison was made between the mean absolute errors of the estimated breathing rate using the three methods.

Figure 3.4 (a) and (b) represent the mean absolute error and the variance of the absolute error of the estimated breathing rate of a human breathing with a breathing rate of18 breaths/min behind a 20cm gypsum wall using the FFT-based estimator, moving average method, and ellipse fitting method, respectively.

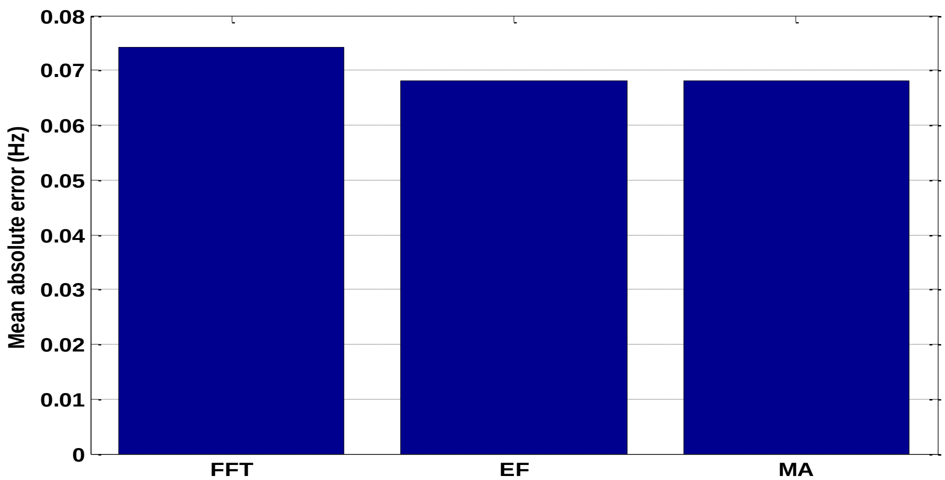

(a)

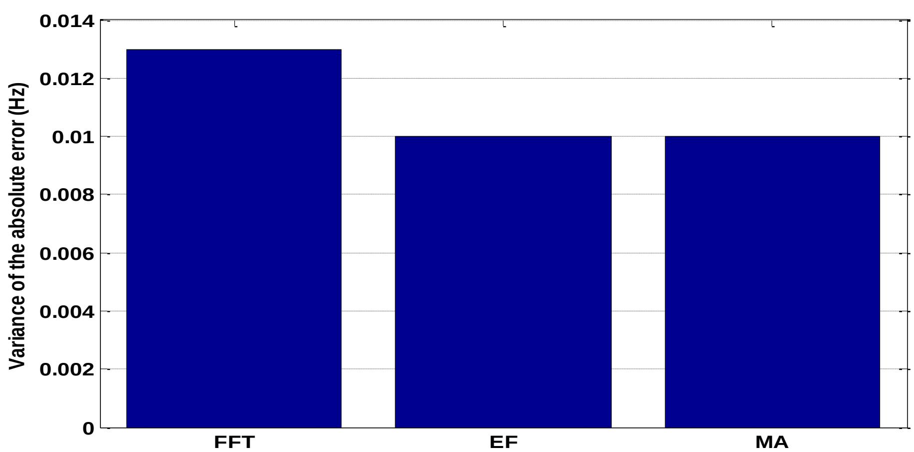

(b)

Figure 3.4 (a) The mean absolute error (b) the variance of the absolute error of the human breathing rate estimate by using the FFT, ellipse fitting (EF), and moving average (MA) methods in an office environment and behind 20 cm gypsum wall.

In this research, we proposed a method that combines zero-crossing technique with an adjustable BPF to reduce the effect of the human breathing harmonics. The method is simple, has high performance in a short observation time (20 seconds or less), and provides high estimation accuracy with low computational complexity. As can be determined at this time, no previous researchers have used the zero-crossing technique in this application, with physiological boundaries combined with an adjustable BPF.

3.2.5 Posture Estimation

Human posture estimation is very important especially in monitoring elderly people in home care applications. Dwelly invented a Biometric radar system and method for identifying persons and positional states of persons [*39*]. In this patent, the human posture is estimated using a neural network. Osterwell invented a method to detect fallen people using UWB radars with steerable directional receive antenna by inspecting the distance of the torso from the floor [*40*]. The inventor uses multiple receivers and one transmitter or two transmitters and one receiver to locate the subject. Also, many radars are fixed in different locations in the room to estimate the distance of the torso from the floor.

In the literature, the signal reflected due the chest movement is often assumed to be sinusoidal [*34,93,94*], and as such is used for detecting and estimating breathing rates. In [*80*], human detection using movements due to breathing was investigated using periodic movements of the chest and it was concluded that movement was proportional to an absolute value of a sinusoidal signal whose frequency was the breathing frequency. Interestingly, in [*48*], the observation of the breathing rate of a number of humans indicated that the displacements of the abdomen are larger than the displacements of the chest. Based on this observation, the mathematical model presented in [*95*] has been adapted along with the two cylinder models presented in [*96*] and observations on the displacements of the chest and the abdomen are recorded.

In this thesis, the ratio between human breathing harmonic magnitudes is used as a feature to estimate the human posture. Again, to the best of our knowledge, nobody has previously utilized the ratio between the breathing harmonic magnitudes in posture estimation.

Chapter 4

Clutter Reduction and Target Detection

4.1 Introduction

The objective of this Chapter is to present the first three main blocks of the general block diagram of target detection and breathing rate estimation algorithms as presented in Fig 3.1. These include: preprocessing, clutter suppression, and range estimation and multi-target discrimination. The first three steps are addressed using a single algorithm based on SVD. The decision to apply SVD in this situation was based on the promising results from the literature, as discussed in Chapter 3, when SVD is applied to remove the clutter and the noise. However, the problem with SVD is that the principal component which contains the target information may be unknown. It was observed that the target information is not only in the second principal component, as claimed in the literature [*24*] but may be found in the few first principal components as well. When the incorrect principal component is picked up, clutter may be detected as a target. This problem can be solved by using a method to detect if this principal component contains target information or not. It was observed that reflections from multiple targets can be distinguished by removing the principal components one after the other. The novel idea here is that detection of a target in a particular range-bin is used to detect the range and distinguish between two targets. A target was detected by studying the skewness of the square of the signal obtained from the correlator output. If the skewness value dropped under a threshold line, a target was detected. Several traditional preprocessing algorithms were applied prior to SVD and skewness test. To summarize, this Chapter will focus on subject detection, determine the range of the subjects, and distinguish between two subjects. Figure 4.1 is the main block diagram for the range estimation and multiple target discrimination algorithms which are presented in this Chapter.

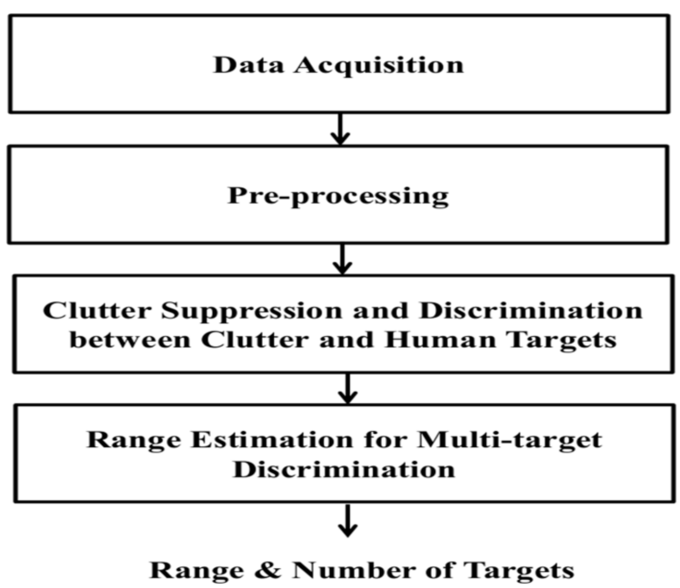

Figure 4.1 Range estimation and multiple target discrimination block diagram.

4.2 SVD in Clutter Suppression

SVD decomposes the data to orthogonal sets with different variances. If the projections that contain almost all clutter and noise are known, they can be removed and the inverse transform can be used to represent the data again without clutter and noise. The data matrix can be presented as multiplication of three matrices. One of these matrices is a diagonal matrix with variances ordered from the higher to the lower value. These values are called principal components. If the SNR of the received signal is more than one, the reflections from the target will be strong and the data of interest is expected to be in the first few components. As a result the noise is expected to be in the remaining components [*97*]. SVD has been used as a noise reduction method in speech processing [*98*], image processing [*99*], radar target recognition [*100*], and human detection behind walls [*24*,*26*,*25*,*101*].

In human detection behind walls, the first components always contain clutter because the amplitude of the received signals reflected from clutter is higher than the signal reflected from human targets. On the other hand, noise still exists in the last components that the target information could be found in the middle components. Assume that we have recorded M scans, where M is the number of scans in slow time direction. Each scan has a data vector of length N, where N is the number of points in fast time. The radar scans can be presented as M number of sources which have N samples of data. If the scans are recorded in a matrix

$$X \in ₵^{M \times N}$$

If $M \geq N$, then the SVD of X can be presented as

$$X = USV^T \tag{4.1}$$

where, $S = \binom{\Sigma}{0}$, $S \in ₵^{M \times N}$, $U \in ₵^{M \times M}$, $V \in ₵^{N \times N}$, $U^T U = I$, $V^T V = I$.

$$X = U\binom{\Sigma}{Z}V^T \tag{4.2}$$

where, $\Sigma = \begin{pmatrix} \sigma_1 & \cdots & 0 \\ \vdots & \ddots & \vdots \\ 0 & \cdots & \sigma_N \end{pmatrix}$, $\sigma_1 \geq \sigma_2 \geq \cdots \geq \sigma_N \geq 0$, and Z is a $(M - N) \times N$ zero matrix.

If $M < N$, then the SVD of X can be presented as

$$X = U(\Sigma\, Z)V^T \text{ , } Z \text{ is a } M \times (N - M) \text{ zero matrix.} \tag{4.3}$$

where, X is the data matrix, the matrix U is called a left singular vector matrix and forms orthonormal basis for the slow time vectors, V is called a right singular vector matrix and forms orthonormal basis for the range profile vectors, and the scalars σ_m , where $m \in \{1, \ldots, N\}$, are called singular values or principal components, M is the number of scans, and N is the number of range-bins [*102*]. If the data matrix is $M \times N$ elements, then the total singular values is $min\{M, N\}$.

SVD is used to identify and order the dimensions along which data points exhibit the most variation. The majority of energy reflected from human targets is expected to be in a number of singular matrices. Every singular matrix, or decision matrix, can be presented by:

$$D_j = US_jV^T \tag{4.4}$$

where $D \in ₵^{M \times N}$, $j \in \{1, \dots, N\}$, S_j is a matrix that has the same size as S and all elements are zero except $S(j, j)$.

The data matrix can be presented as

$$X = D_1 + D_2 + \cdots + D_N = US_1V^T + US_2V^T + \cdots + US_NV^T \tag{4.5}$$

Equation 4.5 can be rewritten as [*24*]

$$X = X_{clutter} + X_{targets} + X_{noise} = \sum_{a=1}^{A} US_aV^T + \sum_{b=1}^{B} US_bV^T + \sum_{c=1}^{C} US_cV^T \tag{4.6}$$

where, A, B, and C are the principal components number that contain clutter, target, and noise information, respectively. If singular values that contain clutter and noise data are known, clutter and noise can be suppressed by eliminating these singular values. Then the data matrix can be reconstructed using inverse transformation of the SVD. Using this method, an effort is made to use SVD as a filter to eliminate the effect of clutter and noise. For human detection, an informed estimation should be made as to which singular value should be omitted. In [*24*], Singh assumed that the clutter data will be in the first singular value. However, Nezirović, in his PhD thesis found that the target data may appear in the third singular value using a threshold decision [*26*].

The research will investigate which components contain target information, how to use SVD in clutter and noise suppression, what statistical approach should be used to detect a moving target, and how SVD can be used to discriminate between targets.

4.3 Pre-processing

Before applying the SVD method, the data is filtered in the slow time (scans) direction and the fast time (range-profile) direction from the unwanted frequency. The unwanted frequencies in slow time direction are the frequencies out of the breathing frequency band, and the unwanted frequencies in the fast time direction are the frequencies out of the transmitted signal frequency band.

The signal pre-processing algorithm prepares the data to be studied using SVD. Figure 4.2 shows the data pre-processing algorithm. The first step, a Butterworth IIR 16th order BPF, with transition band 3.1-5.3 GHz is applied to filter frequencies that are out of the transmitter frequency band and which may distort the received range profile signal. Butterworth filter is used because it has a maximally flat magnitude response in the passband. Figure 4.3 shows the filter's magnitude response.

In the second step, the following simple highpass filter is applied in each range-bin to eliminate the effect of clutter:

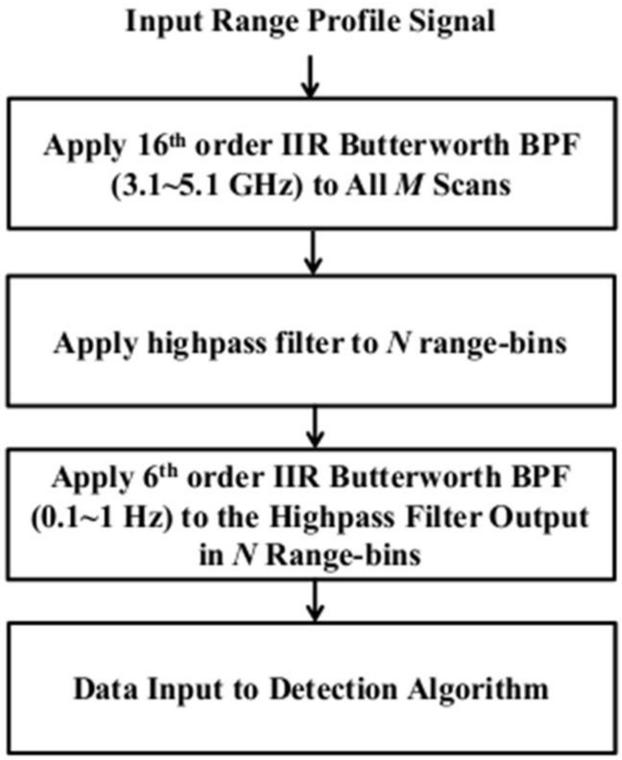

Figure 4.2 The data pre-processing algorithm.

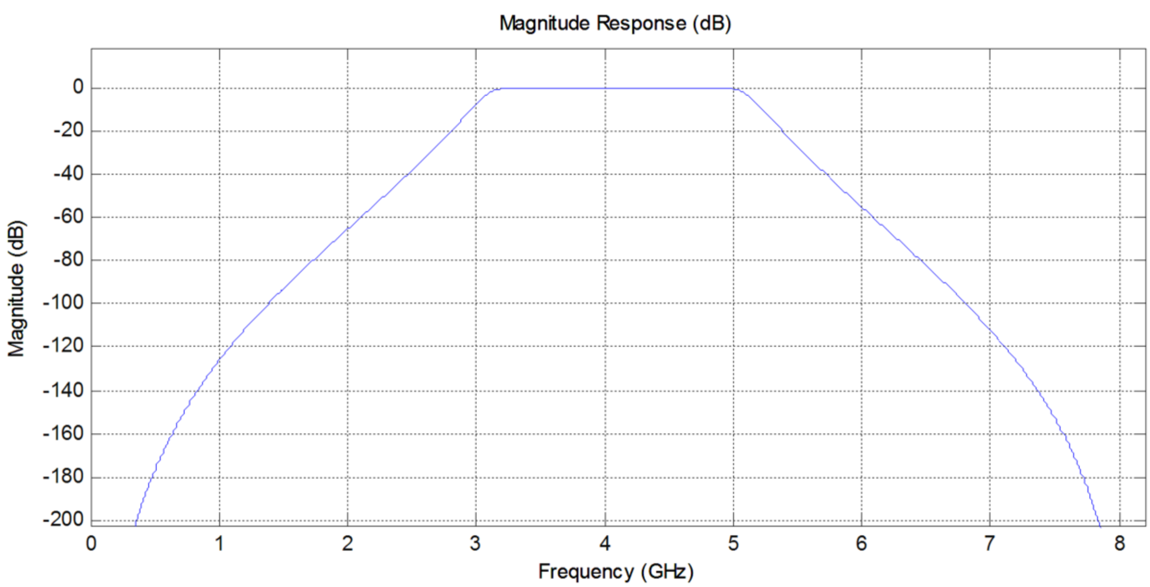

Figure 4.3 The magnitude response of 16^{th} order IIR Butterworth filter.

where $Y_{HPF}(m)$ is the output of the highpass filter, $X(m)$ is the amplitude of the range profile in the slow time direction, and $m \in \{1, \dots, M\}$. The filter has a zero at a frequency equal to zero. This simple filter can eliminate stationary clutter. Remaining clutter is removed by using the statistical clutter removal method. In the following, the SVD method is used to remove clutter which has not been removed using the highpass filter. Finally, a 6th order IIR Butterworth filter with transition width 0.1-1 Hz is used to restrict the analysis to the breathing frequency band. The Butterworth filter is used so as to have a flat magnitude response in the passband. The filter guarantees attenuation in the signal more than -50 dB beyond 5 Hz.
The Z transform of the transfer function of the BPF is:

$$H_{BP}(Z) = 10^{-3} \times \frac{0.162 - 0.486Z^{-2} + 0.486Z^{-4} - 0.162Z^{-6}}{1 - 5.7964Z^{-1} + 13.8769Z^{-2} - 17.8119Z^{-3} + 12.8681Z^{-4} - 4.9612Z^{-5} + 0.7975Z^{-6}} \tag{4.8}$$

After that, SVD is applied to the output of the data pre-processing algorithm.

4.4 Distinction Between Clutter and Human Targets

This research involved using the SVD method to estimate which range-bin may contain a target. SVD is not enough to estimate which range-bin contains a target because a range-bin may have a maximum power value resulting from a clutter. Another method to estimate which decision matrix D_j contains the human target information is needed.

In an effort to detect the presence of the target in any range-bin, skewness is used as the decision statistics. Since the distribution of the signal's energy received at the radar, corresponding to clutter, is different from that of the target, its skewness changes. This forms the basis of using skewness as a decision metric in this thesis. In Chapter three, a literature review was given on using the higher order moments of distribution of radar returns in an effort to discriminate between targets and clutter. In this section, the skewness method is introduced to examine if this range-bin has a target or not. This statistical approach relies on studying the distribution of square of the range profile amplitude in a range-bin in a large number of scans. Figure 4.4 shows how the amplitude of the reflected range profile changes when a target in a specific range-bin is breathing. The Target is in the range-bin B and when the target breathes, the maximum amplitude of the range profile changes in the three range-bins A, B, and C. In this method, the distribution of the range profile amplitude squared is studied after applying the pre-processing data algorithm.

This method illustrated that the distribution of square of the range profile amplitude when there is no target has a longer tail than that when a target exists. This is because the high signal amplitude reflected from the clutter is rapidly attenuated by the BPF. The distribution of the clutter was tested in 46 different environment experiments. All results show that the distribution of the amplitude squared after applying our data pre-processing algorithm has a longer tail than that when a target exists. The Weibull distribution has been introduced as an empirical fit to many measured target and clutter distributions [*85*,*103*].

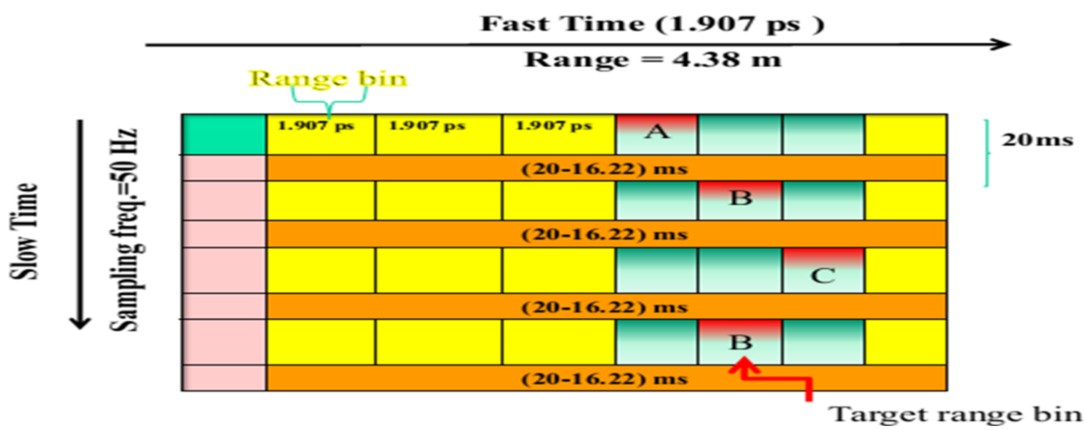

Figure 4.4 An example of range profile amplitude changes due to breathing.

The probability distribution function of the magnitude squared of the output of the correlator x can be presented as:

$$P_x(x) = \frac{k}{\lambda}(\frac{x}{\lambda})^{k-1}e^{-(x/\lambda)^k} \quad , x > 0 \tag{4.9}$$

where, $k > 0$ is the shape parameter and $\lambda > 0$ is the scale parameter. The shape parameter is related to the skewness of the distribution. The skewness of the distribution is inversely proportional to the parameter k.

4.4.1 Fitting Clutter and Target Distributions to Weibull Distribution

In this research, a study was made of the distribution of the magnitude square of the output of the correlator in the UWB radar receiver. Goodness-Of-Fit (G-O-F) techniques were introduced in [*104*]. In the following test, an examination was made as to whether the target and the clutter distribution fit to the Weibull distribution or not.

4.4.1.1 Chi-squared test

To test if a random sample $x_1, x_2, \dots x_i, \dots x_n$ has a distribution function $F(x)$, the approach proposed by Pearson [*104*] was used to partition the random sample range of x_i, where $i \in \{1{:}n\}$, to cells $A_1, A_2, \dots A_j, \dots A_M$, where $j \in \{1{:}M\}$, then studied the binomial distribution of the observed number of x_i's in every part A_j. The binomial distribution with parameter n can be presented as [*104*]:

$$p_i = p\left(x \in A_j\right) = \int_{A_j} dF(x) \tag{4.10}$$

where $p\left(x \in A_j\right)$ is the probability of x falls in A_j. Pearson measured the lack of fit for the data by measuring the difference between the observed and expected number of observations of x in every cell A_j. Pearson used the following statistics to test the fit of a random sample to a specific distribution:

$$A^2 = \sum_{i=1}^{M} \frac{(N_i - np_i)^2}{np_i} \tag{4.11}$$

where, A^2 is the Pearson chi-squared statistics, M is the number of the cells for the data set, N_i is the number of observations of x_i's in a cell for the data set, and np_i is the expected observations in the same cell [*104*].

4.4.1.2 Kolmogorov-Smirnov Goodness-Of-Fit test

The Empirical Distribution Function (EDF) of a real set of data has been studied to measure how much this data fits a specific distribution. If the real data has an unknown distribution $F(x)$ there may be a desire to measure how much this distribution fits a known distribution $F_n(x)$. The difference in the EDF of both distributions can be used to measure levels of similarity of two distributions [*104*].

The statistics that measure the difference between $F(x)$ and $F_n(x)$ are called the EDF statistics [*104*]. Two statistics are D^+, which is equal to the largest vertical difference between $F(x)$ and $F_n(x)$ when $F_n(x)$ is greater than $F(x)$, and D^-, which is equal to the largest vertical difference between $F(x)$ and $F_n(x)$ when $F_n(x)$ is smaller than $F(x)$. Kolmogorov introduced the most well-known statistic D [*104*]:

$$D = max(D^+, D^-) \tag{4.12}$$

The Kolmogorov test, also known as Kolmogorov-Smirnov Goodness-Of-Fit (KS G-O-F) test, can be used to test whether the distribution of the data received in UWB radar has a Weibull distribution or not. EDF tests for the Weibull distribution have been introduced in [*104*]. The EDF of the Weibull distribution is [*104*]:

$$F(x) = 1 - exp\left\{-(\frac{x}{\lambda})^k\right\} \ , \ x \geq 0 \tag{4.13}$$

The KS G-O-F test can be run for a Weibull distribution or convert the real data distribution to an extreme value distribution and run the KS G-O-F test for an extreme value distribution. Let $y = -log(x)$, the distribution for Y becomes [*104*]:

$$F(y) = ex\,p\left[-exp\left\{-\frac{y-\varphi}{\theta}\right\}\right], \ -\infty < y < \infty \tag{4.14}$$

where $\theta = 1/k$ and $\varphi = -log(\lambda)$. The new distribution will be an extreme value distribution if x belongs to a Weibull distribution. Using the previous 46 measurements that have been used to perform the chi-squared test, the KS G-O-F test is applied to the raw data vector in a target's range-bin and in a clutter's range-bin in every measurement. The results of the KS G-O-F test show that the data has Weibull distribution with different shape factors. The shape factor becomes higher when a target exists in that range-bin.

4.4.1.3 Experimental Verification of the Model

Forty-six measurements were collected from two subjects breathing normally and standing 3.5 m from UWB radar behind a 20 cm thick gypsum wall. Each measurement has only one subject. The chi-squared test in [*104*] was applied to the magnitude squared of the output for the correlator in the UWB receiver. The test was applied to the raw data vector in a target's range-bin and in a clutter's range-bin. The raw data distribution was compared to a Weibull distribution. The clutter distribution passed the chi-squared test in all measurements. The target distribution passed the chi-squared test in 43 measurements. The other three measurements passed the test when they were compared to a normal distribution or exponential distribution. In a clutter range-bin, when we fit the raw data distribution to Weibull distribution to estimate the distribution parameters, the shape factor of the distribution k was from 0.2~0.3. In a target range-bin, the shape factor k of the Weibull distribution, which is presenting the target distribution in all the 43 measurements, is approximately equal to one. As a result, the skewness value of the distribution in a target's range-bin will be lower than in a clutter's range-bin.

In the following, we fit the normalized magnitude squared of the output for the correlator to a Weibull distribution. Figure 4.5 is the CDF of the normalized magnitude squared of the output for the correlator in the blue line and the CDF of Weibull distribution function in the dashed red line. These CDFs are at different transmitted power (-16 dBm, -15 dBm, -14 dBm, and -13 dBm), in a clutter's range-bin. The CDF of the magnitude squared of the output of the correlator in a clutter range-bin fits the CDF of the Weibull distributions at different transmitted power.

Figure 4.6 is the CDF of the normalized magnitude squared of the output for the correlator in the blue line and the CDF of Weibull distribution function in the dashed red line at different transmitted power (-16 dBm, -15 dBm, -14 dBm, and -13 dBm), in a target's range-bin. The CDF of the magnitude squared of the output for the correlator in a target range-bin fits the CDF of the Weibull distributions at different transmitted power.

Figure 4.7 shows the skewness value of the magnitude squared of the output for the correlator at every range-bin when a target is breathing with normal breathing 3.5 m from the UWB radar and standing 1.5 m behind a 20 cm gypsum wall. In the figure, it can be observed that there is no drop in the value of the skewness where the wall exists. The distribution of the data vector in a clutter range-bin has a Weibull distribution with shape parameter equal to 0.2~0.3. Weibull distribution with a shape factor equal to 0.2~0.3 has a skewness value around 8. When a target exists in a range-bin, the shape factor k increases and becomes near the value of one. This decreases the skewness of the Weibull distribution to be less than 3.

In the following, we fit $F(y)$ to an extreme value distribution. Figure 4.8 presents $F(y)$ using the blue line and the CDF of an extreme value distribution function using the dashed red line at different transmitted power (-16 dBm, -15 dBm, -14 dBm, and -13 dBm), in a clutter's range-bin and the Kolmogorov-Smirnov test statistics D was equal to 0.113, 0.103, 0.113, 0.119, respectively. Figure 4.9 is $F(y)$ shows using the blue line and the CDF of an extreme value distribution function using the dashed red line at different transmitted power (-16 dBm, -15 dBm, -14 dBm, and -13 dBm), in a target's range-bin and the Kolmogorov-Smirnov test statistics D was equal to 0.044, 0.032, 0.020, 0.038, respectively.

Examining the Figures 4.5, 4.6, 4.8, and 4.9, and the results of chi-squared test and KS G-O-F test of 46 measurements it is evident that the distributions of the magnitude squared of the output of the correlator can be presented as Weibull distribution, except in 3 measurements. The shape factor of the distribution in a clutter's range-bin will have a smaller value (0.2~0.3) than the shape factor in a target's range-bin (around one). The skewness value of the Weibull distribution is inversely proportional with the shape factor k. This means the skewness value can be used to discriminate between clutter and human targets.

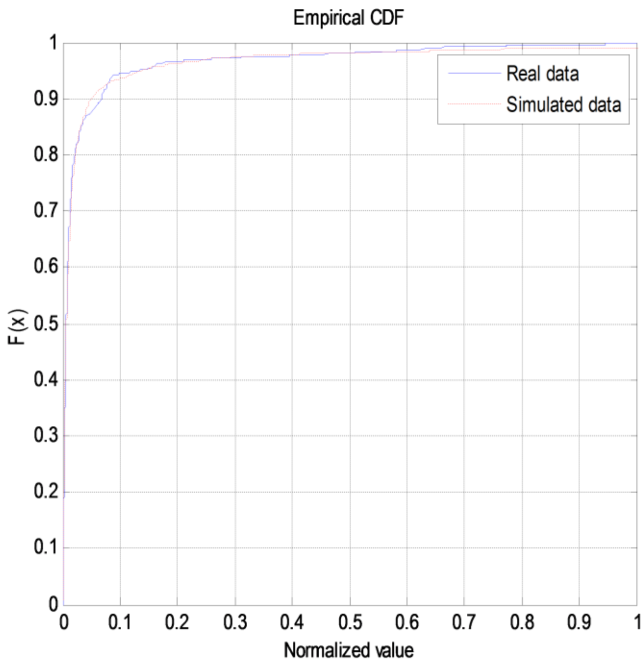

(a)

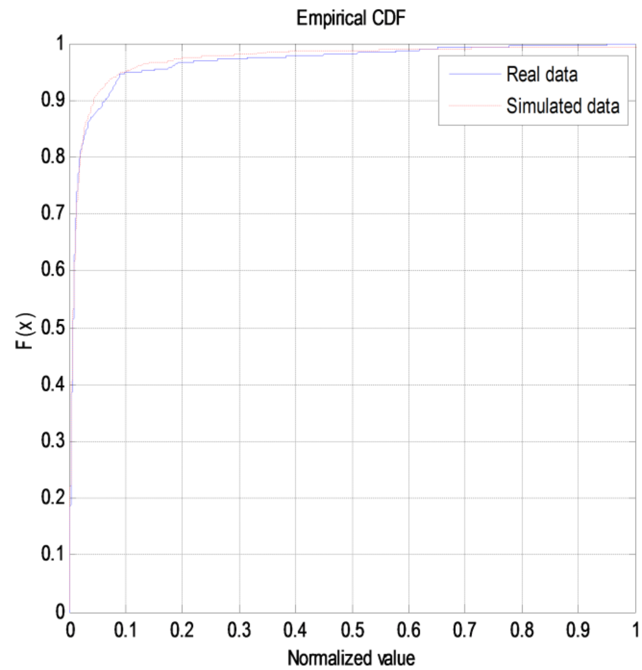

(b)

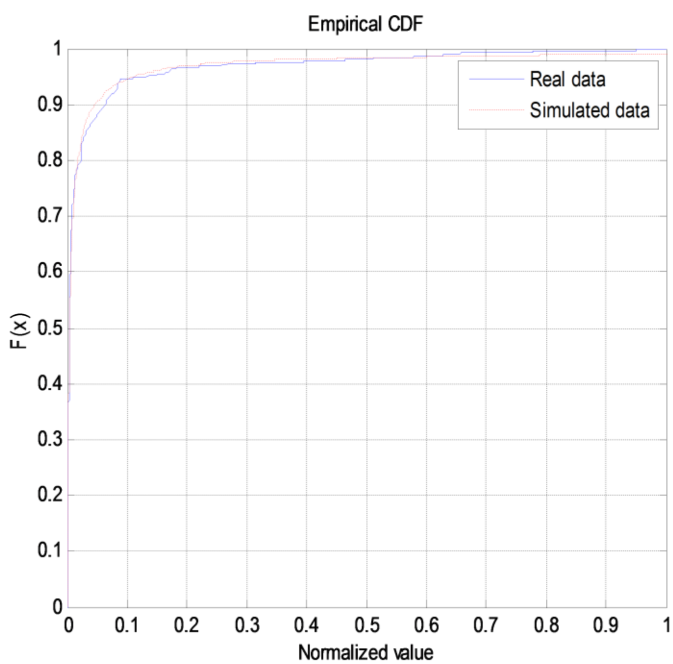

(c)

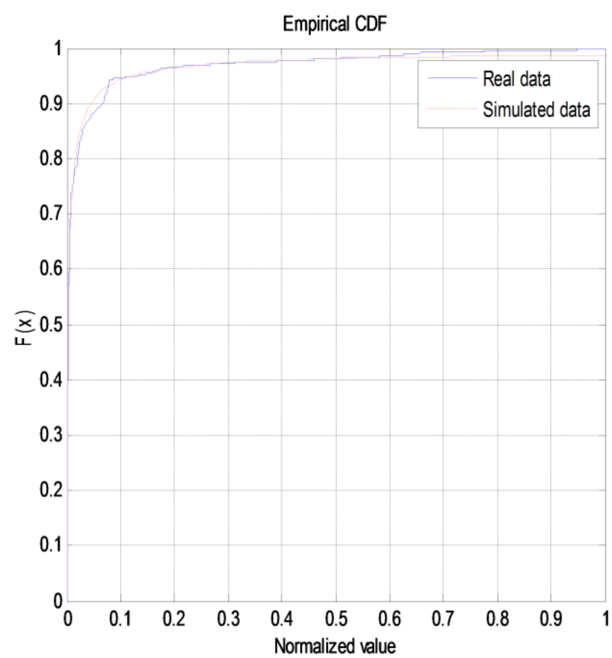

(d)

Figure 4.5 CDF of the magnitude squared of the output for the correlator in a clutter range-bin and the CDF of Weibull distribution function at transmitted power of (a) -16 dBm (b) -15 dBm (c) -14 dBm (d) -13 dBm.

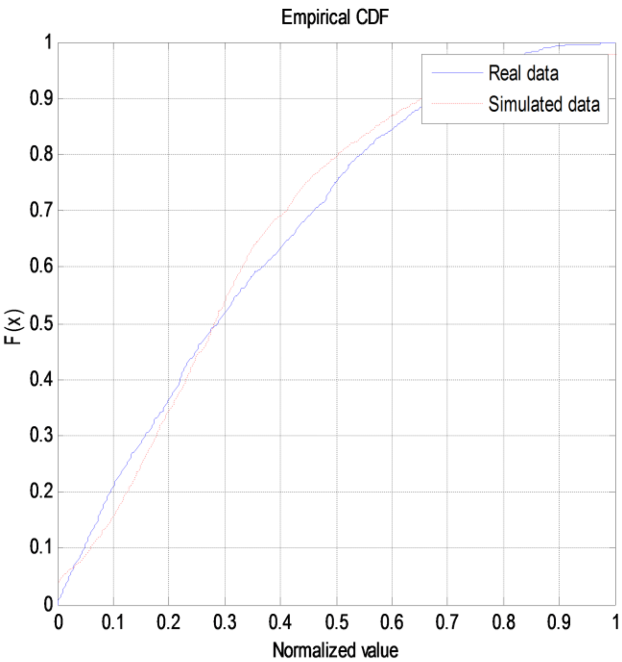

(a)

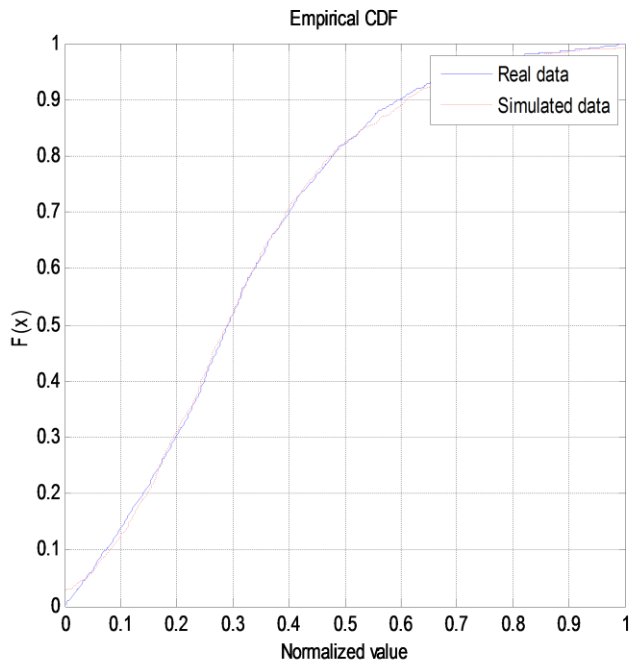

(b)

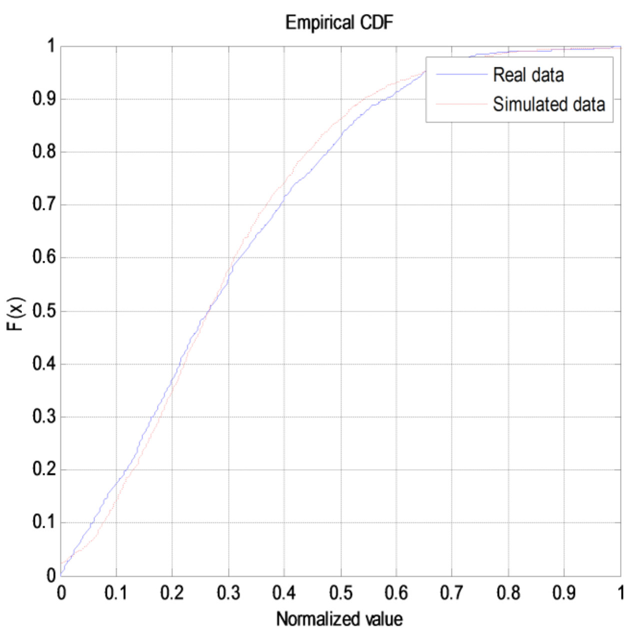

(c)

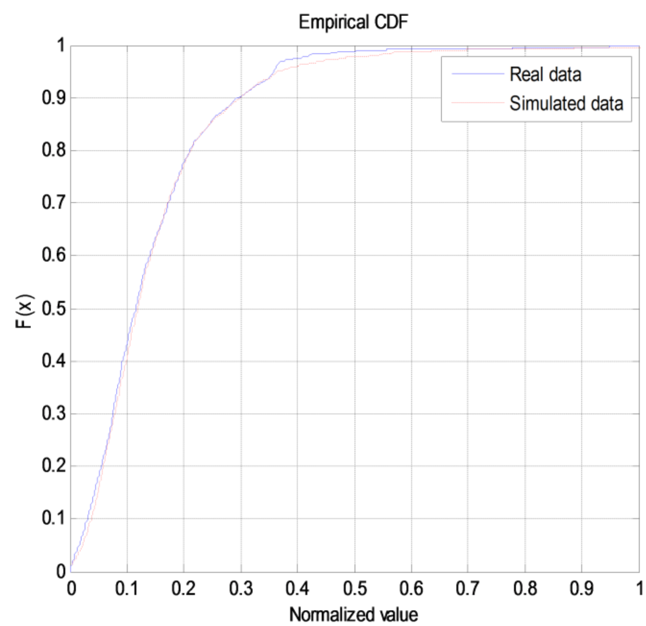

(d)

Figure 4.6 CDF of the magnitude squared of the output for the correlator in a target range-bin and the CDF of Weibull distribution function at transmitted power of (a) -16 dBm (b) -15 dBm (c) -14 dBm (d) -13 dBm.

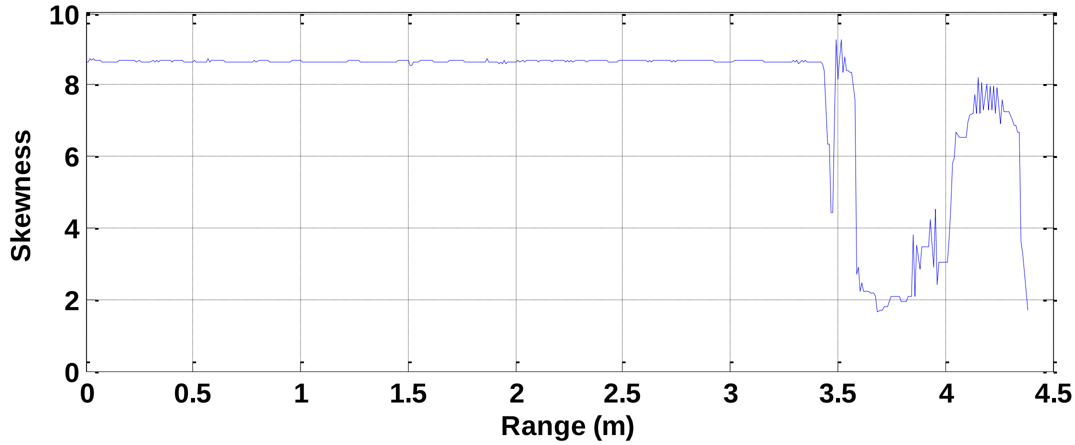

Figure 4.7 Skewness of the squared value of the extracted human breathing signal where the subject is located 3.5 m from UWB radar and 1.5 m behind a 20 cm thick gypsum wall.

Skewness of the amplitude squared distribution at every bin across the scans is determined and the following threshold is calculated:

$$Threshold = [mean(|\gamma_i|) - 0.5\sigma] \tag{4.15}$$

where, γ_i is the skewness of the correlator output squared in the slow time direction at range-bin i and $i \in \{1{:}N\}$, N is the number of range-bins, and σ is the variance of all the skewness values γ_i in all range-bins. Equation 4.16 is the target detection decision based on the skewness test.

$$Skewness \underset{H_1}{\overset{H_0}{\gtrless}} Threshold \tag{4.16}$$

where. H_0 is the null hypothesis when clutter only exists, and H_1 is the hypothesis when clutter and echoes from a target exists. Figure 4.10 shows a target standing 3.5m from the radar and 1.5m from a gypsum wall. The experiment was conducted in a SITE building lab, at the University of Ottawa, Ottawa, Canada. Figure 4.11 (a), (b), and (c) show the normalized power of 2000 scans against the range between the radar and the target without applying SVD, the normalized power of 2000 scans against the range after removing 1st singular value, and the skewness of 2000 scans against the range without applying SVD. It can be observed that the skewness value dropped at the target's range-bin. However, some spikes in the value of the skewness were observed in a few range-bins. Target reflections appear in a number of neighboring range-bins. This feature was used to remove these spikes by applying a median filter of length equal to five samples. Figure 4.11 (d) illustrates the output of the median filter. The spikes were removed and a clear drop in the value of the skewness happened where the target existed.

Figure 4.12 shows a target standing behind a concrete wall supported with a thick plastic layer used to support the walls against earthquakes. This experiment was conducted in the Civil Engineering Department (CED) structure lab at the University of Ottawa, Ottawa, Canada. The figure was divided into four sections. Section 1, 2, 3 and 4 show the radar, the concrete wall facing the radar, the plastic layer facing the target, and the target, respectively. The target was standing 3.5 m from the radar and 1.5 m behind a concrete wall.

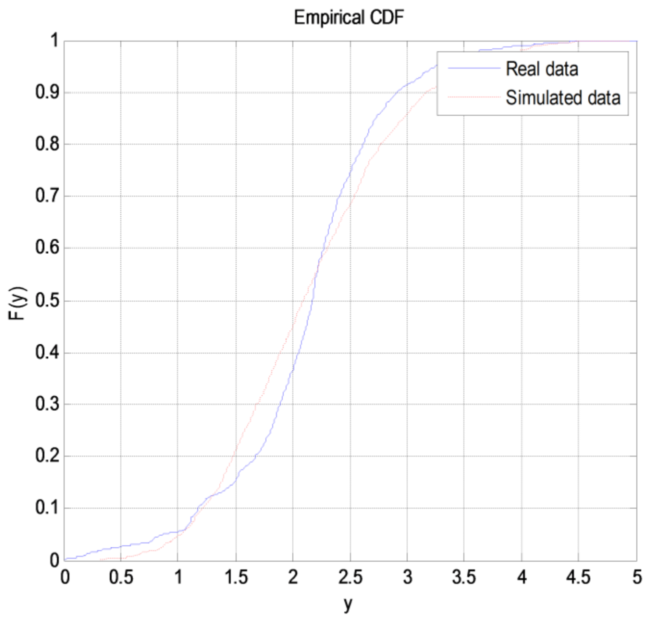

(a)

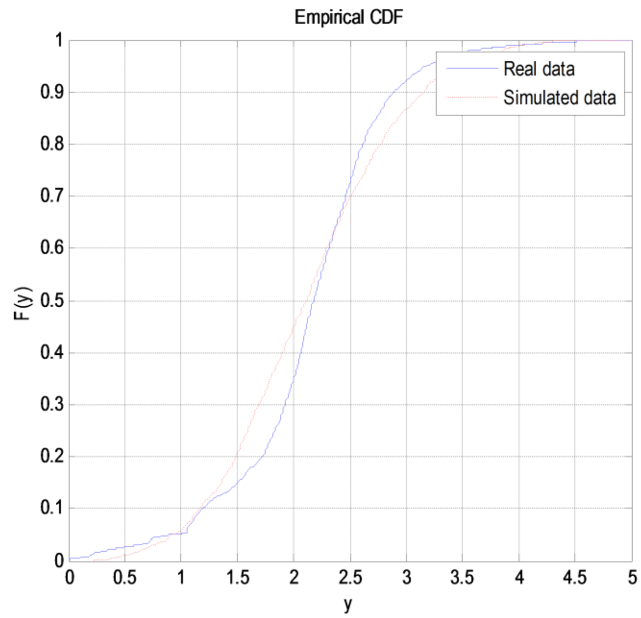

(b)

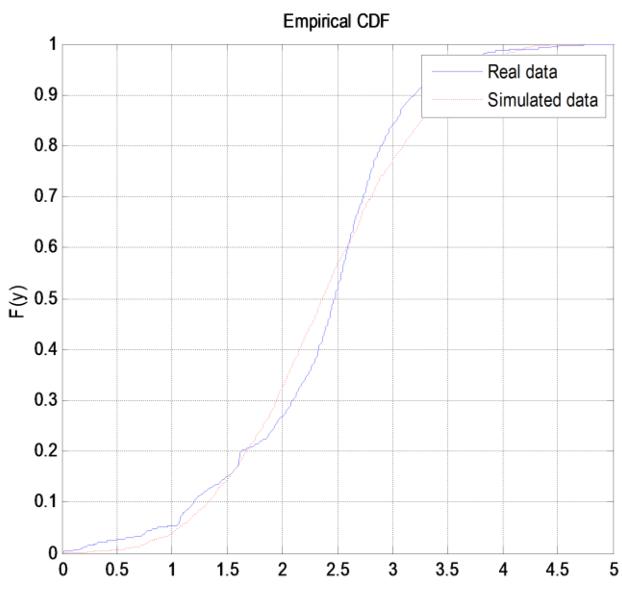

(c)

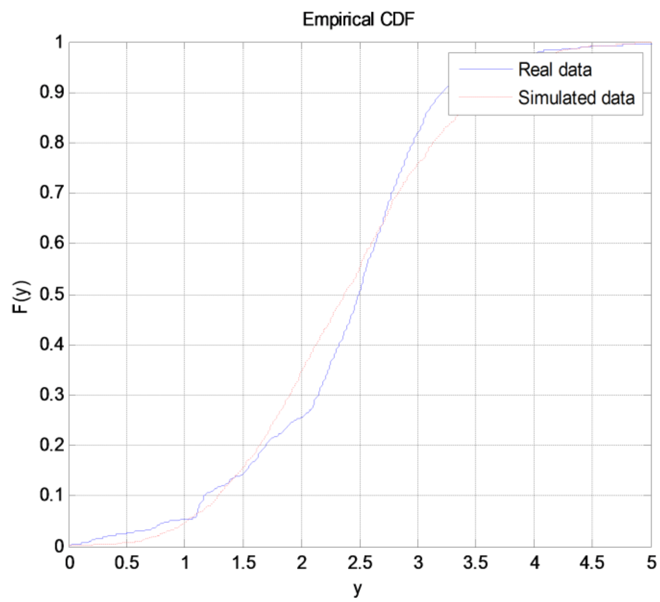

(d)

Figure 4.8 CDF of the magnitude squared of the output of the correlator in a clutter range-bin and the CDF of Weibull distribution function at transmitted power of (a) -16 dBm (b) -15 dBm (c) -14 dBm (d) -13 dBm.

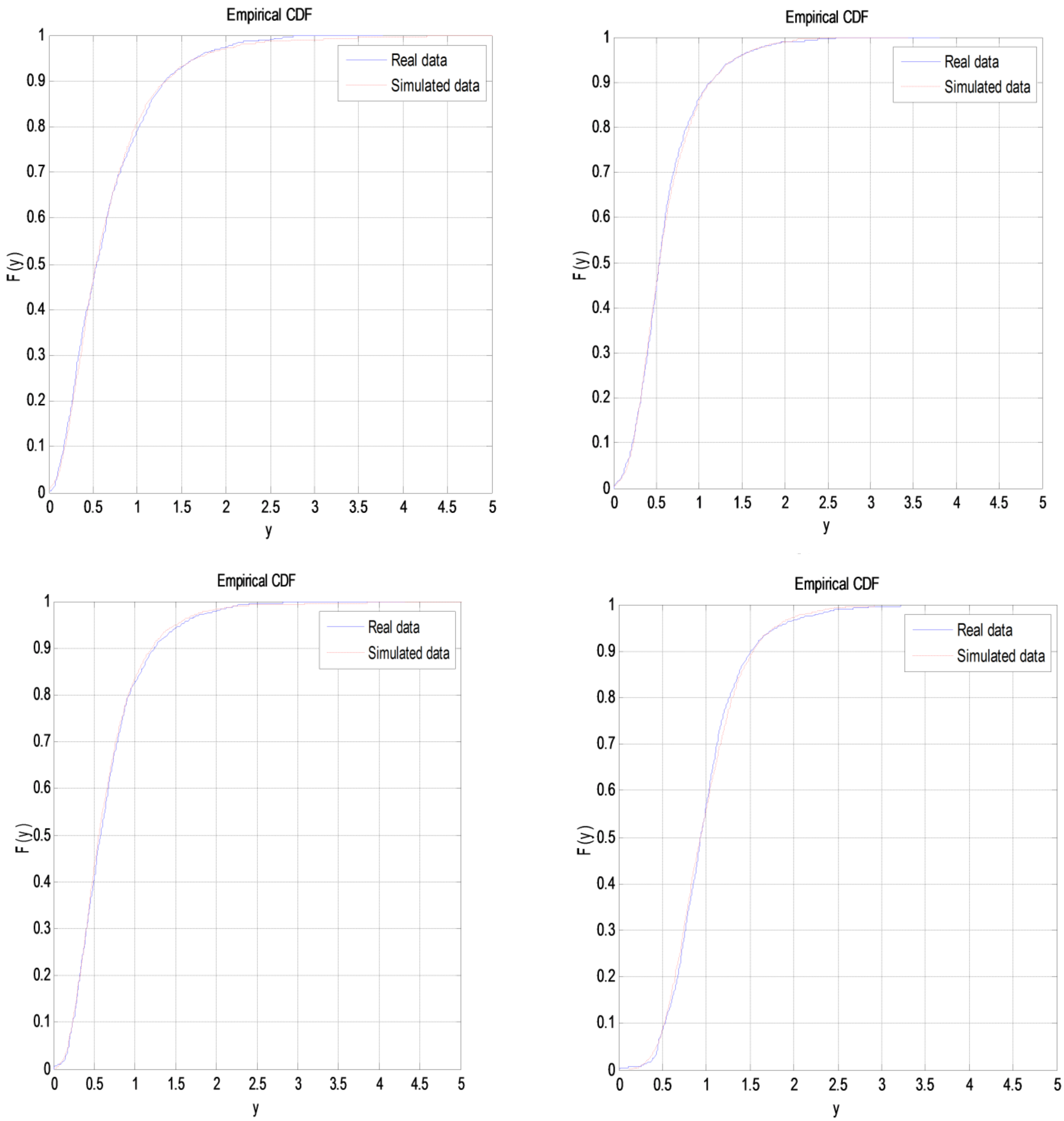

(c) (d)

Figure 4.9 CDF of the magnitude squared of the output of the correlator in a target range-bin and the CDF of Weibull distribution function at transmitted power of (a) -16 dBm (b) -15 dBm (c) -14 dBm (d) -13 dBm.

Figure 4.10 A target is standing behind a gypsum wall.

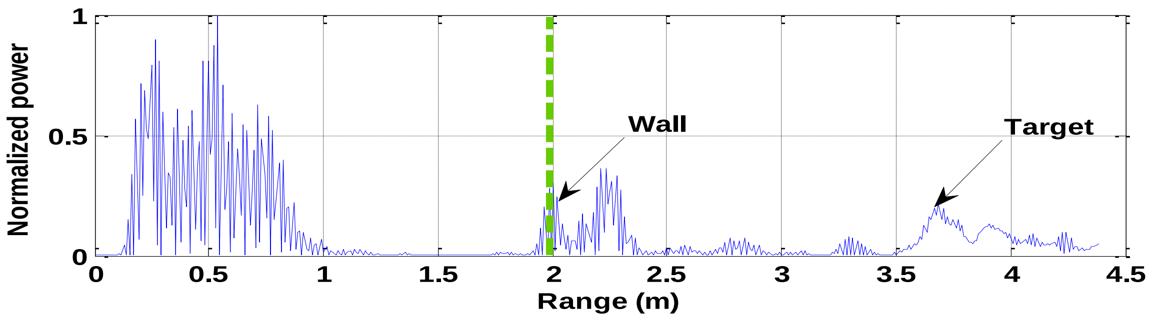

(a)

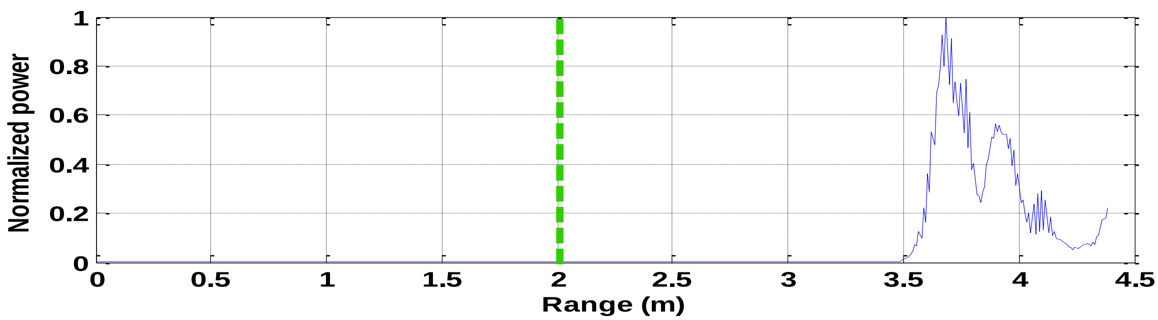

(b)

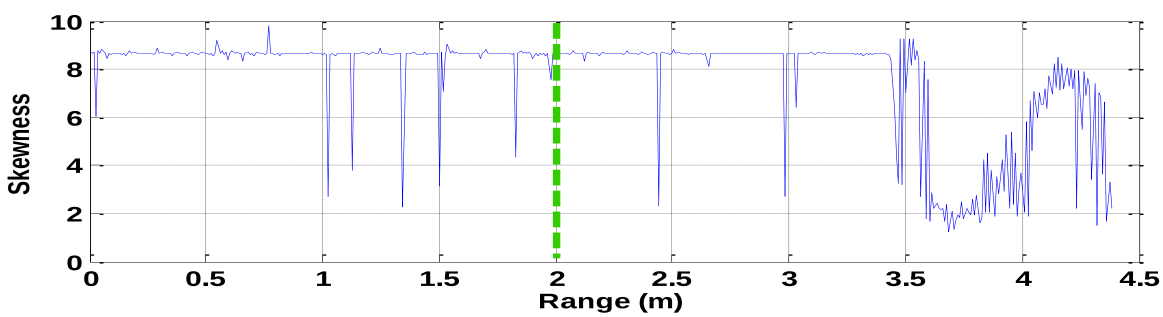

(c)

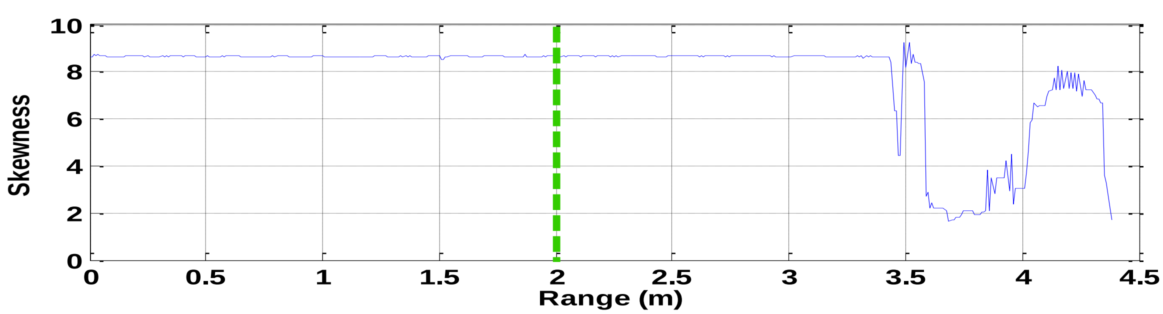

(d)

Figure 4.11 (a) The normalized power without SVD (b) The normalized power after 1st singular value suppression (c) the skewness without SVD (d) the skewness without SVD and after applying median filter.

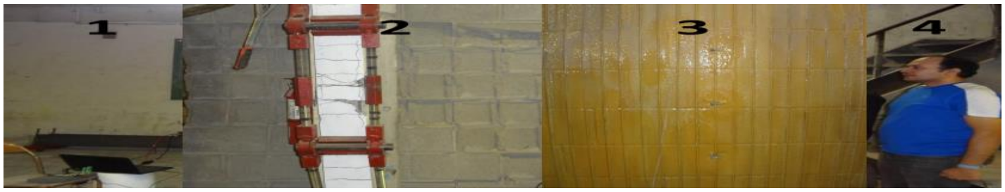

Figure 4.12 A target standing behind a concrete wall supported with plastic layer.

Figure 4.13 (a), (b), (c), and (d) show the normalized power of 2000 scans against range without SVD suppression, the normalized power of 2000 scans against range after removing 1st singular value, the skewness of 2000 scans against range without SVD suppression, and the skewness after applying median filter. The target can be observed in Fig. 4.13 (b) after the first singular value has been removed, by studying the maximum power. Figure 4.13 (c) shows that the skewness did not change in the wall range-bin but changed in the target range-bin. Studying the skewness of a number of scans at every range-bin can be useful for testing if a target exists or not. It can be concluded that studying the skewness is an easy test to implement, and the results are not dependent on the wall composition. Many experiments on human breathing detection behind gypsum and concrete wall were performed. Some other experiments were performed behind masonry brick wall and wood doors. The proposed method of human detection worked well with different types of walls.

It is required to decrease the overlap area between the distribution of the amplitude squared for the output of the correlator in a target's and clutter range-bin, in order to increase the probability of detection. Two solutions have been introduced to increase the probability of detection and decrease the number of false alarms. The first is increasing the SNR of the received signal. When the SNR is increased, the mean value of the distribution of the amplitude squared for the received signal in a target's range-bin will increase and move the two curves apart. This will decrease the overlapped area and reduce the errors. The second solution is to reduce the variance of the two curves. This can be done by reducing the noise power [*85*].

A third solution is introduced to move these curves apart. The skewness method is used to discriminate between the curves. In this method, it is not necessary to use an adaptive threshold method. Assigning a threshold that can detect an abrupt change in the skewness value is sufficient.

4.5 Range Estimation for Multi-Target Discrimination

4.5.1 Range Estimation and Human Target Detection Behind the Wall Based on Singular Value Decomposition and Skewness Variations

Human target detection behind the wall is based on human body deflections. These deflections are generally weak and are masked by the reflections from the wall which form the static clutter; hence, clutter reduction is the first step in detection of a human target using radar technologies. In [*74*], range gating was used to eliminate interference and clutter reflections. However, range gating may not be precise enough to remove clutter and noise. Recently signal processing techniques such as the SVD, have been applied to clutter and noise removal [*24*,*25*].

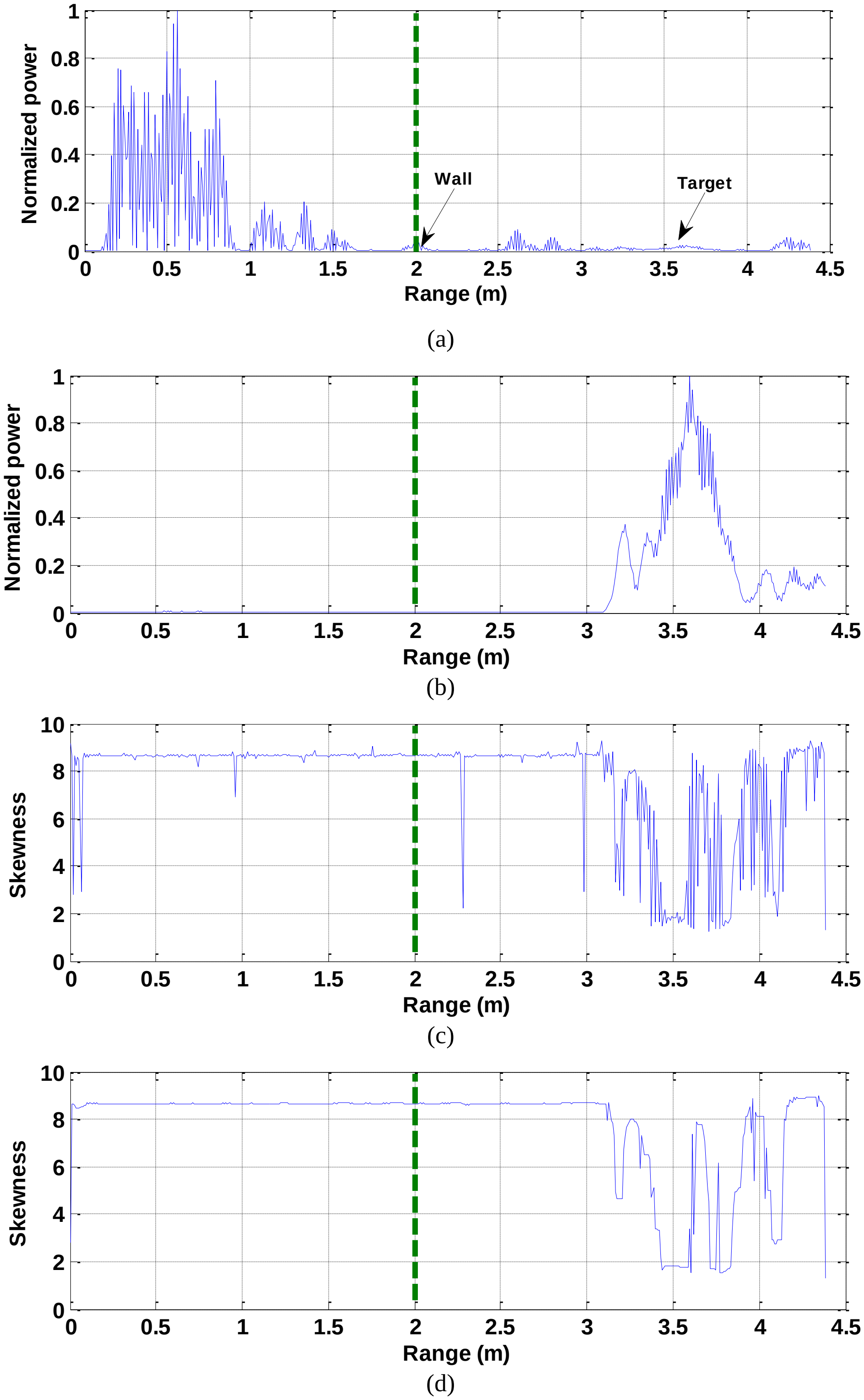

Figure 4.13 (a) The normalized power without SVD suppression; (b) the normalized power after 1st singular value suppression; (c) the skewness without SVD suppression; (d) the skewness without SVD suppression and after applying median filter.

The SVD method works well in both indoor and outdoor environments for clutter removal. Three different detection techniques were discussed in [*24*] for various types of walls. The DFT followed by the clutter reduction method using SVD worked for a gypsum wall, a brick wall and a wooden door but failed to work for thick concrete walls. In [*26*], the singular value pertaining to the target was estimated using a threshold-based decision method and was applied to detect human breathing inside a 10 cm thick concrete sewer pipe. The proposed work in this chapter does not focus on breathing rate estimation but on the estimation of the range-bin that contains a target; hence does not resort to frequency domain techniques.

Although some references show that the clutter information is in the first component or in the third component of the diagonal matrix S [*24,26,25,75*], this research illustrated experimentally that clutter and noise information may extend to the fifth component for the diagonal matrix S. The components or singular values in the diagonal matrix S are arranged from higher to lower values, i.e. the maximum singular value will be the element $S(1,1)$ and the minimum singular value will be the element $S(N, N)$. Figure 4.14 shows the first 40 singular values from σ_1 to σ_{40} in a diagonal matrix S for a target standing 1.5 m from UWB radar and breathing behind a 20 cm thickness gypsum wall.

Figure 4.15 shows an experiment that explains this research approach. A target was standing 15m away from the radar in a hall at the University of Ottawa, Ottawa, Canada, and he was breathing normally. The radar detection maximum range was set to 20 m in this experiment. The upper Figure shows the energy reflected from clutter and the target. The effect of cross-talk between the transmitting and receiving antenna appears in the first five meters range. After applying the SVD, removing the first singular value, and inverse SVD again, the effect of the cross-talk between the two antennas still existed. The bottom Figure shows many energy peaks higher than the target's energy peak at 15 m. This means that the clutter is not only in the first singular value.

4.5.2 Algorithm for Human Detection and Range Estimation

Figure 4.16 shows the detection algorithm. To detect a target, SVD was applied to the output of the data pre-processing algorithm. After that, the first singular value was removed and this should contain clutter information, then perform inverse transform to obtain information matrix again. The power of the signal in the slow time direction is determined at every range-bin. The bin b with the maximum power is selected as a potential target and the test statistics based on skewness are applied. As a result, the following detection decision is made:

If skewness < Threshold, the target is detected. If the test statistics are not satisfied, absence of a target is reported. This was continued for five iterations. The experimental results show that no target exists beyond the sixth singular value. However, it may be different in different detection scenarios. Further experiments were performed to verify the method presented in this section. The setup of the experiment is shown in Fig. 4.10.

The data matrix using P410 radar was obtained for two normally breathing subjects, each standing behind a 20 cm thick gypsum wall and at a distance of 3.5m alone from the radar. Twenty three measurements for each subject were collected. SVD was used to first identify the range-bin that contained a target, followed by the skewness test to confirm the detection. The detection decision was made according to Eq. 4.16.

The target was detected 44 times out of 46, leading to missed detection (error type II) of about 4.35%. False detection (error type I) was zero.

4.5.3 SVD in Discriminating Between Two Targets

Two targets can be detected by omitting the singular values by order. Each time the matrix X is inversed transform and the maximum power range-bin is tested. It can be predicted that the two targets might be seen in the first six components. The maximum power was examined each time. If the maximum power has been recorded in different range-bins, then there may be multiple targets. After recording the range-bins that contain the targets, the skewness method is used to test if these range-bins contain a target or a clutter.

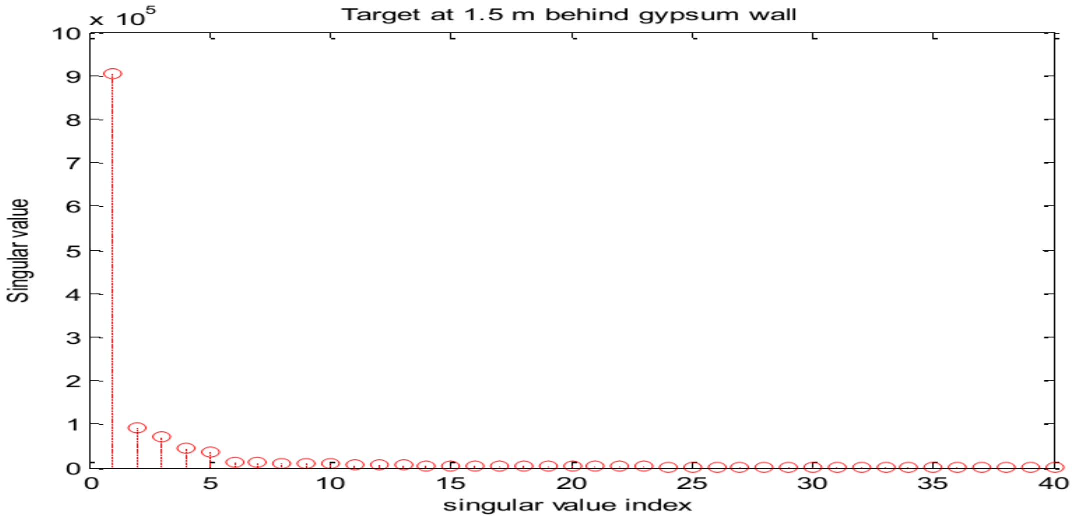

Figure 4.14 The first 40 singular value when a target is breathing behind a 20 cm thickness gypsum wall and standing 1.5 m from the radar.

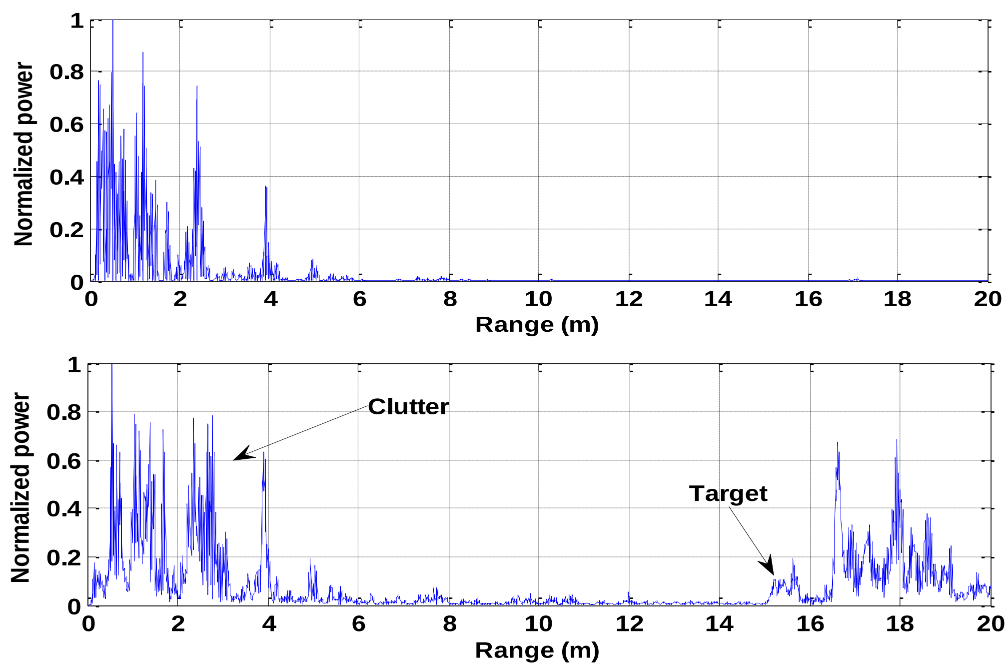

Figure 4.15 The normalized power in all range-bins of the waveform reflected from a target standing 15 m away from the UWB radar in free space and breathing normally.

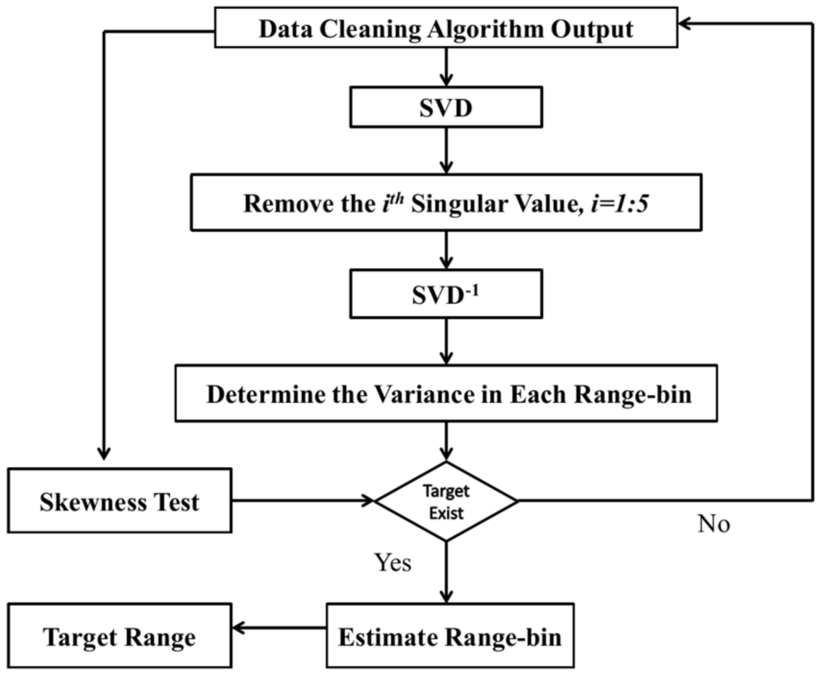

Figure 4.16 SVD detection algorithm.

4.6 Experimental Results

4.6.1 Human Breathing Detection

In this section, a comparison is made between the RMD algorithm proposed in [*26*] and presented in Chapter three and the proposed method of this research in the human detection for three experimental cases. In the first case there is no target. In the second case, an effort is made to detect a human breathing for 20 seconds and to have stopped breathing for 20 seconds in free space. In the third case, the goal was to detect a target standing behind a gypsum wall, as shown in Fig. 4.10. The target wore a breathing belt to validate the breathing rate results. Table 4.1 shows the experiment parameters for the radar and the target.

Case one:

When the developed RMD algorithm was applied, the maximum magnitude values detected in the rectangular window in the first decision matrices exceeded the assigned threshold values. A false alarm was detected in the first, second, fourth and fifth decision matrices. These false alarms were detected at range ≈ 0.5 m. When the detection algorithm was used, no target was detected. Figure 4.17 shows that the skewness was not changed at 0.5 m because there was no target.

Table 4.1 Experiment parameters.

Index	Parameter	Value
1	Transmitted pulse duration	500 ps
2	Pulse repetition interval	1 ns
3	Resolution	7.5 cm
4	Number of scans	2000
5	Number of range samples	480
6	Sampling frequency in slow time	50 Hz
7	Target breathing rate	20 breaths per minute

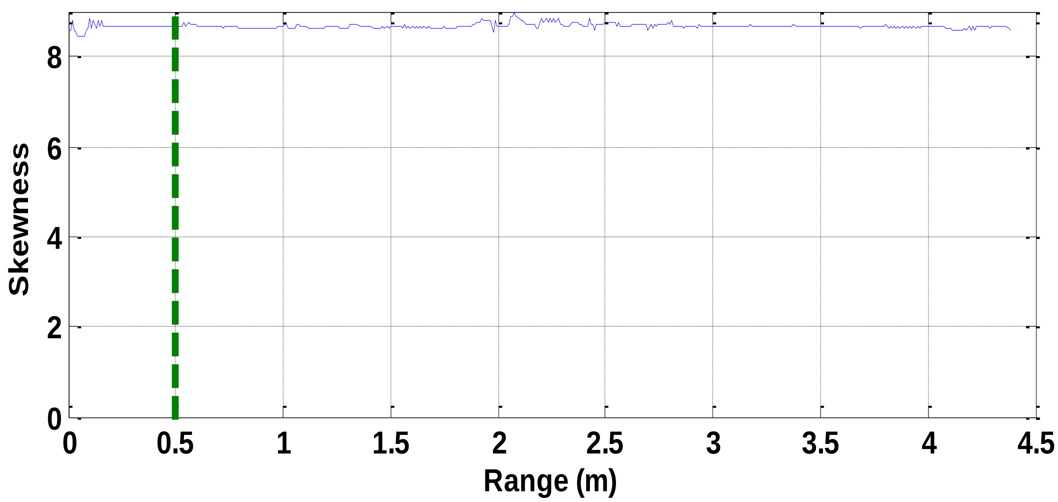

Figure 4.17 The skewness of the matrix X when there is no target.

Case Two:

The target was breathing 18 breaths per minute and was sitting 2.3m from the radar in free space. When the developed RMD algorithm was applied, the target was detected at 2.3 m. The detected breathing rate was 0.2 Hz. Figure 4.18 shows the periodogram of the received signal at every range-bin after applying the Developed RMD (DRMD) algorithm. The algorithm pertinent to this research detected 6 breaths in 20 seconds (0.3 Hz) and the stop breathing event. The target was detected at 2.29 m.

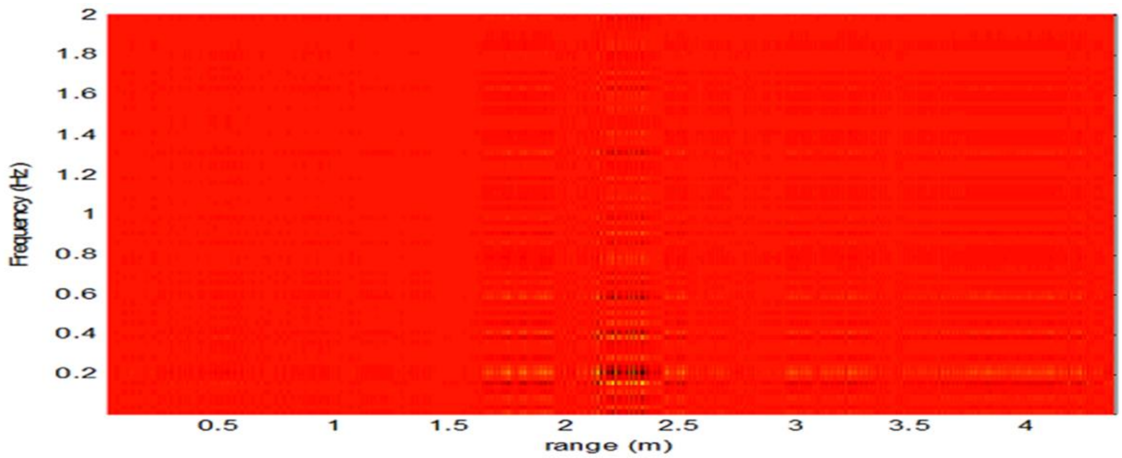

Figure 4.18 The periodogram of the received signal at every range-bin.

Case Three:

A target was standing behind a gypsum wall as shown in Fig. 4.10 and breathing normally. Although, the target can be detected using DRMD algorithm, the magnitude in the first four decision matrices exceeds the threshold values. The estimation of the breathing rate and the range were difficult because multiple breathing frequencies were detected in multiple ranges. The algorithm pertinent to this research showed better performance.

In the following, a comparison was made between the performance of the human breathing detection by the RMD algorithm and the proposed algorithm. The reflected signal was collected from a human breathing with a breathing rate equal to 18 breaths/min. The subject was asked to breathe when he/she heard a tone generated by a software program and repeated every 3.33 seconds The experiments were performed in an office environment at the University of Ottawa, Ottawa, Canada. The reflected signal was recorded while the target was standing, sitting, and lying down at six different angles θ, 0^0, 30^0, 60^0 , 90^0 ,135^0, and 180^0, relative to the radar antenna plane. Eighteen measurements were taken at different postures and different angles. Another set of measurements was performed while the target was standing, sitting, and lying down at six different angles θ while behind a 20 cm thickness gypsum wall.

From Eq. 3.4, the threshold value depends on the singular absolute value λ_j and P_{fa}. However, it is hard to predict the suitable P_{fa} for high detection probability. The DRMD algorithm proposed in [*26*] and the proposed detection method of this research were applied to the eighteen measurements in office environment and behind the wall. The output of the two algorithms is a decision about the existence of a human target. Figures 4.19 is the Receiver Operating Characteristics (ROC) curves which show the true positive detection rate versus the false positive detection rate in free space and behind 20 cm thick gypsum wall, respectively. The figure shows the area under curve (AUC) in each case. The AUC is higher when the proposed detection method is used. It can be concluded that the performance of this research method is better than the performance of the DRMD method in both scenarios: free space and behind walls.

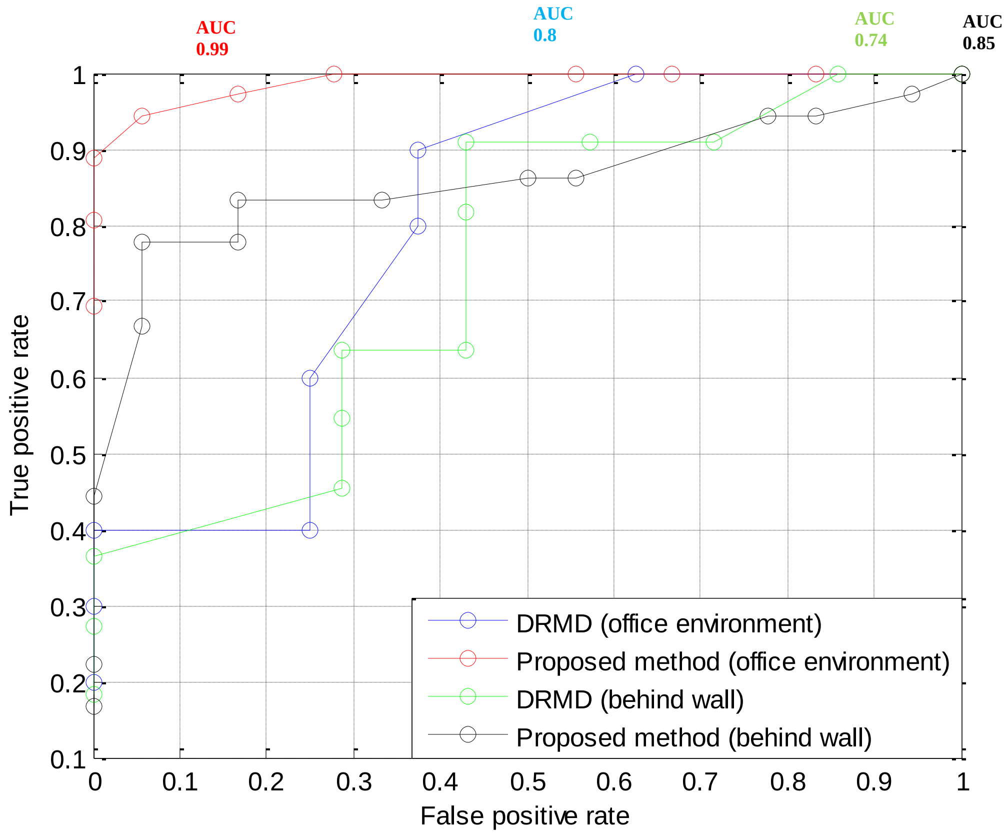

Figure 4.19 ROC curve of human breathing detection in free space and behind a 20 cm gypsum wall.

4.6.2 Detection of Two Targets

In this section the performance of the proposed algorithms is studied as it relates to discriminating between two human targets in free space and behind the wall. Figure 4.20 shows two targets sitting in an anechoic chamber at the University of Ottawa, Ottawa, Canada. One target is sitting 2.5 m from the radar and the other target is sitting 3.5 m from the radar.

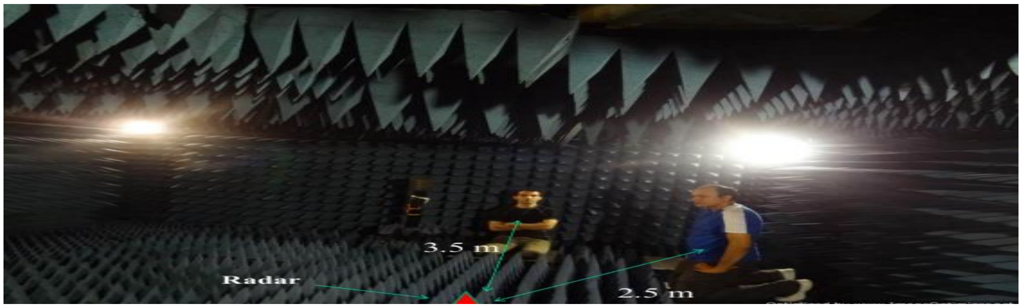

Figure 4.20 Two targets sitting in an anechoic chamber at the University of Ottawa, Ottawa, Canada.

Figure 4.21 (a), (b), and (c) shows the normalized power in all range-bins without using SVD suppression, after removing the first singular value, and after removing the first and the second singular values, respectively. After removing the first singular value, the clutter was suppressed. The first target can be observed at 2.5 m in Fig. 4.21 (b). After removing the first and the second singular values, the clutter and the first target information were suppressed. The second target can be observed at 3.6 m in Figure 4.21 (c). After removing the first, second, and third singular values, the second target was detected; hence the iteration stopped.

It was observed that the minimum resolution to detect two targets in free space is 20 cm. Any two targets detected in the range of 20 cm are considered as one target. Figure 4.22 (a) shows two targets standing 3.5 m and 3.8 m respectively from the P410 UWB radar and behind a 20 cm gypsum wall. Figure 4.22 (b) shows the normalized power against the range before and after removing the first and second singular values. The maximum peak of power after removing the first singular value was detected at 3.8m distance from the radar where the first target was standing. When using the skewness test at that bin, the detection was confirmed. Similarly, after removing the second singular value, the second target was detected at 3.5 m. Also, the second target was detected after removing the first three singular values; hence the iteration stopped. Figure 4.22 (c) is the skewness of the received signal amplitude squared. We can observe a drop in the skewness value where the two targets are. SVD along with skewness thus can be used to estimate the range of the targets and discriminate between them. Thus, the algorithm can discriminate between two targets separated by 30 cm behind a 20 cm thick gypsum wall. However, the algorithm proposed in [*32*] and presented in Chapter 3 can discriminate between two targets separated by more than 60 cm.

The algorithm presented in Fig. 4.17 was applied to discriminate between the two targets. In every iteration, the power of the signal in the slow time direction is determined at every range-bin. The bin, *b*, with the maximum power was selected as a potential target and the test statistics based on skewness are applied. In addition, the following detection decision is applied:

Case	**Power**	**Skewness**	**Decision**
1	Peak	Did not pass the test	False alarm
2	Not peak	First drop in the skewness value	Target
3	Peak	Pass the test but not the first drop in the skewness value	Target

In case one, a maximum power was detected in *b* but the distribution does not pass the skewness test. The maximum power observed in this range-bin is due to antenna coupling, power reflected from a wall, or generally a stationary object. If a maximium power is observed in a range-bin which pass the skewness test, then a target exists. In case teo, the first target may have a reflected energy less than the second target. In this senario, the second target will be detected first and the first target will be skipped. However, the first drop in the skewness value happens at the first target. If a first drop in the skewness value is detected, it can be assumed that this drop is related to the presence of a human target. In case three, the skewness value is tested for the second target's range-bin. If the range-bin passed the skewness test, two targets are detected. The algorithm is applied with the following steps:

- A target is detected at first drop in the skweness value.

- Run the SVD detection algorithm in Fig. 4.16 for 5 iterations.

- Find the range of the targets.

- The bins, b_1, b_2,… with the maximum power were selected as a potential target and the test statistics based on skewness are applied.

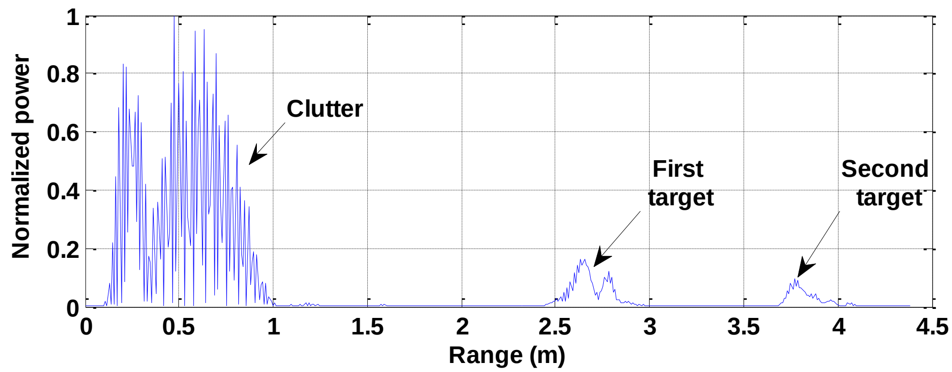

(a)

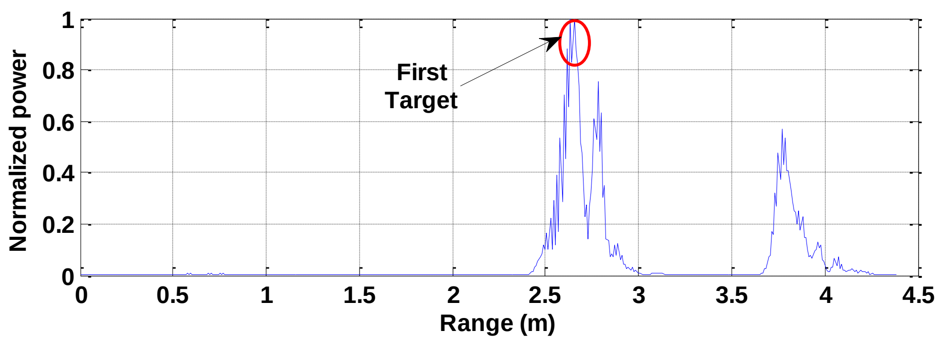

(b)

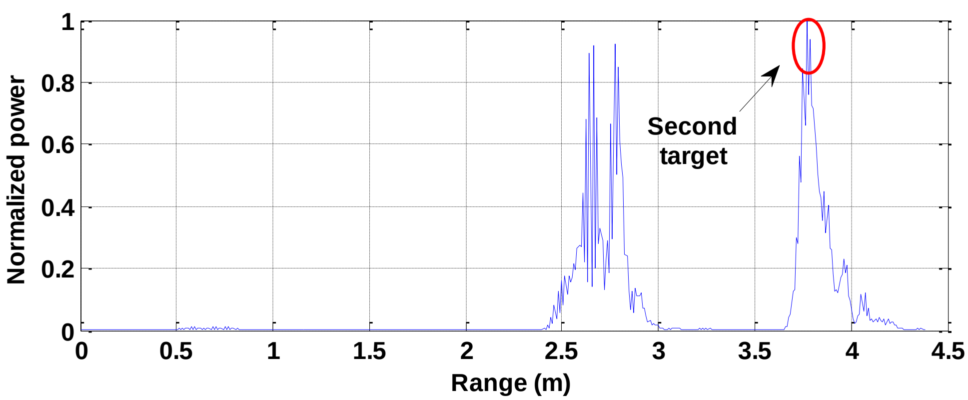

(c)

Figure 4.21 (a) The normalized power without SVD suppression (b) The normalized power after 1st singular value suppression (c) The normalized power after 2nd singular value suppression.


P410
Radar
First
Target
Second
Target

(a)

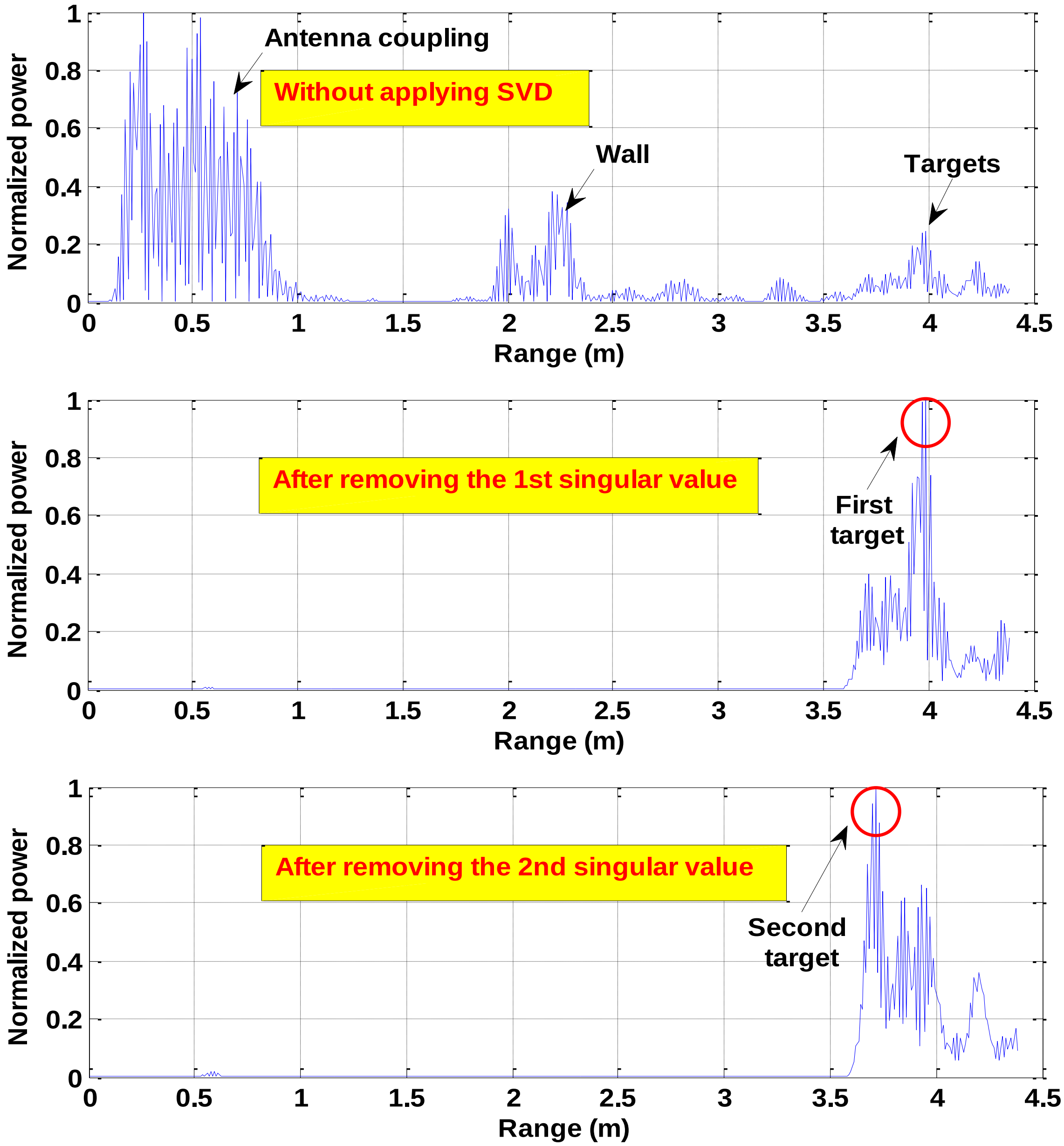
Antenna coupling
Without applying SVD
Wall
Targets
Normalized power
Range (m)
After removing the 1st singular value
First
target
After removing the 2nd singular value
Second
target

(b)

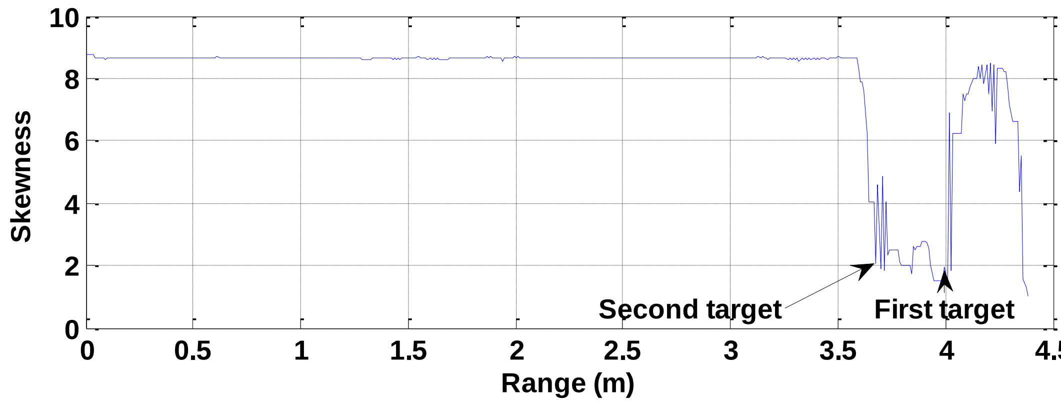

(c)

Figure 4.22 (a) Two targets standing 0.3 m from each other, 3.5 m from P410 radar behind a gypsum wall; (b) normalized power vs. range before and after removing the first and second singular values; (c) skewness vs. range before applying SVD.

The proposed algorithm was applied to discriminate between the two targets breathing with normal breathing and separated by 1 m, 0.5 m, and 0.3 m. Three experiments were performed in an anechoic chamber, an office enviroment, and behind a 20 cm gypsum wall, at the University of Ottawa, Ottawa, Canada. The proposed algorithm was applied to the nine measurements and two targets were successfully detected in every measurement.

One limitation of the proposed algorithm is when only one target exists, the reflections from this target may appear in a false range because of the multipath effect. The algorithm was applied to detect one target breathing normally and standing in an anechoic chamber, an office enviroment, and behind a 20 cm gypsum wall. Nine measurements were collected in each experiment. In the case of the anechoic chamber and the office enviroment, one target was detected in eight measurements and two targets were detected in one measurement. In the case of behind the wall, one target was detected in six measurements and two targets were detected in three measurements.

In future work, the proposed algorithm will be used to enhance the performance of the algorithm presented in [*32*]. Any interference generated from the first target in the range-bins behind it will be removed by using the algorithm in [*32*]. Then this research's method will be applied to discriminate between multiple targets.

4.6.3 Stop Breathing Detection

In the following, the algorithm proposed in Fig. 4.16 is applied to detect the event of stop breathing in a time window equal to 40 seconds. A target was breathing normally with a breathing rate equal to 0.3 Hz and standing 3.5 m from the radar in an anechoic chamber. The target was breathing with a normal breathing for 20 seconds and he stopped breathing for 20 seconds. The target was detected at 3.4 m away from the radar. Figure 4.23 (a) is the normalized correlator output at the estimated range-bin. Attenuation in the amplitude of the signal was observed when the target stopped breathing. Stop breathing event could not be detected using the DRMD algorithm proposed in [*26*] because the DFT is applied to the whole reflected signal. STFT was applied to the correlator output signal to study the variations in the frequency spectrum of the breathing signal in time domain. Figure 4.23 (b) illustrates the STFT of the same signal using a window time equal to 10 seconds , an overlap ratio equal to 50%, and utilizing a Hann window in the frequency domain. The stop breathing event can be observed in the last 20 seconds. However, it was very difficult to estimate the breathing rate. The second breathing frequency harmonic magnitude was higher than the first one. Later in Chapter five, the reasons of this error will be discussed. Figure 4.23 (c) illustrates the STFT of the same signal using a window time equal to 10 seconds , an overlap ratio equal to 50%, and utilizing a Hann window in the frequency domain after applying the zero-crossing method with breathing pulse interval constrain. The method is discussed briefly in Chapter five. The stop breathing event was detected at the same time it happened and a breathing rate equal to the real breathing rate (~0.3 Hz) was estimated. The frequency of the breathing rate was observed at 0.3 Hz in the first 20 seconds in Fig. 4.23 (c).

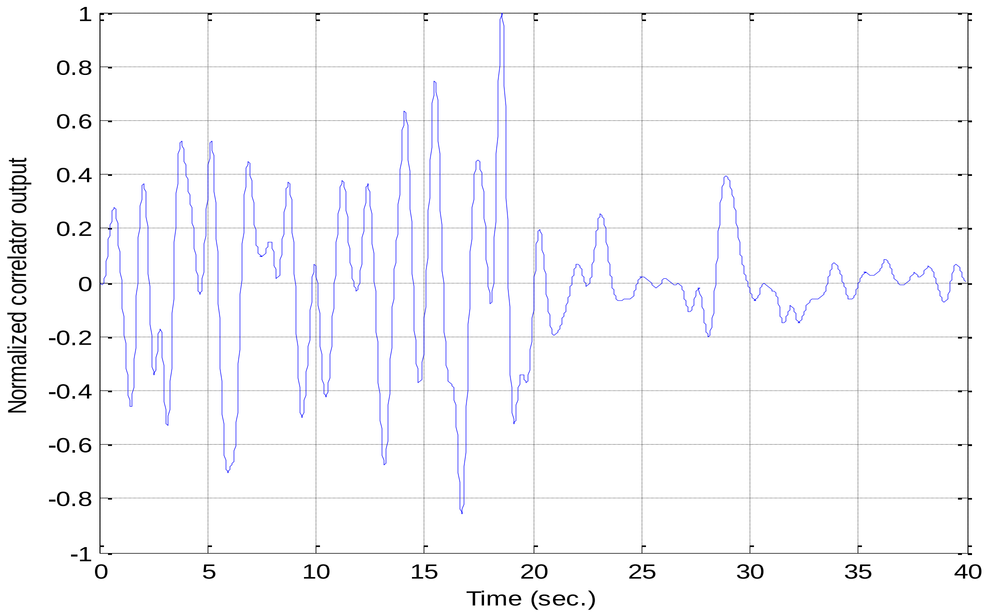

(a)

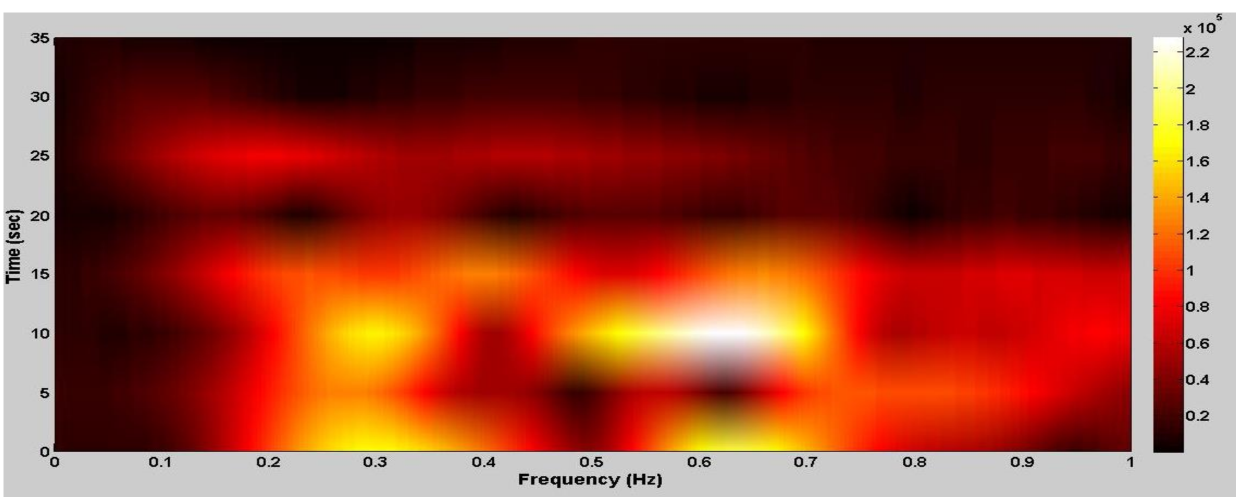

(b)

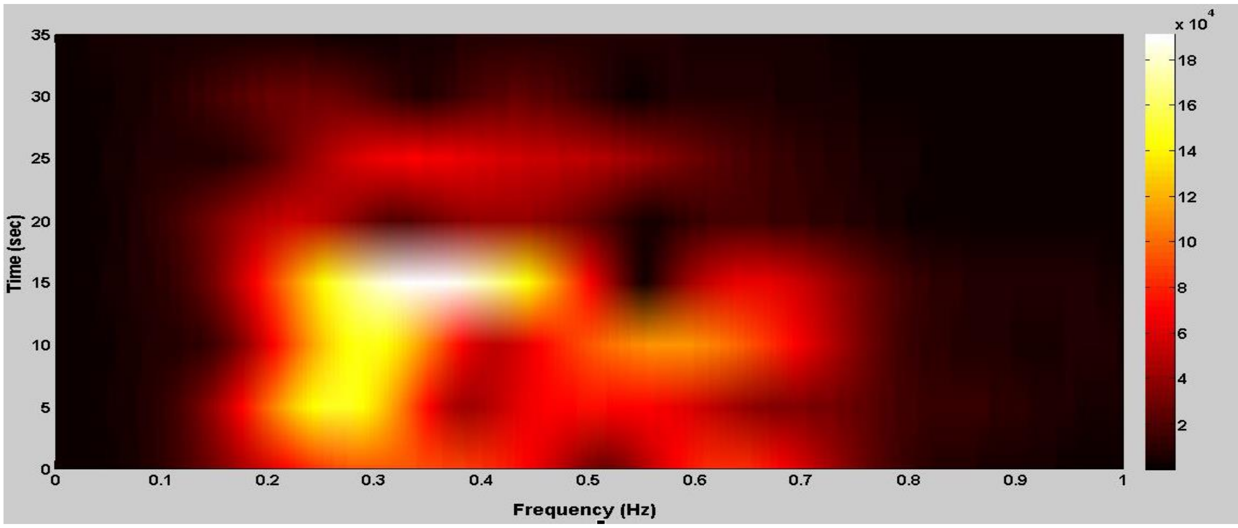

(c)

Figure 4.23 (a) The reflected signal from a target breathing for 20 seconds and stop breathing for another 20 seconds (b) STFT of the same signal (c) STFT after applying zero-crossing method with breathing pulse interval constrain.

4.7 Discussion

In this section a summary will be given of the main points regarding developed methods and algorithms in Chapter 4. The SVD was applied to suppress clutter. A novel method combining the SVD and the third moment determination of the square of the correlator output in the slow time direction was used to estimate which principal component contains the target information. The method was used to detect human targets and estimate the target range. It was found that if the singular values were replaced by zeros one by one, two targets can be detected in free space and behind walls.

Important Observations Obtained Experimentally:

1. It was observed that for each range-bin that the shape of the skewness of the distribution of the amplitudes of the square of the signal changes depending on whether the target is in this range-bin. The skewness will drop in a range-bin where the target is regardless of whether there is a wall between the target and the radar.
2. The target is not always related to the second singular value. Deciding which singular value contains the target information is the critical part in using SVD in clutter suppression. A combination of the SVD and the skewness test method can be used to estimate which singular value contains the target information.
3. It was found that if the first several singular values were replaced by zeros, one after the other the clutter reflections can be reduced; followed by the first target reflections, the second target reflections, the third target reflections...etc.

Modeling:

Probability distribution of the signal in a range-bin with and without target was fitted to a Weibull distribution. It was shown that fitting the probability distribution of square of the signal reflected from the clutter and human target to Weibull distribution passed the Chi-squared test and Kolmogorov-Smirnov test. The result of the modeling work is that the two modeling distributions have significantly different skewness and therefore the skewness can be used as a reliable decision statistic for detecting target's range-bin.

Target Range Estimation Based on SVD Combined with the Skewness Test:

The combination of skewness and SVD was used to estimate the target range. It was found that a drop in the skewness value of square of the correlator output occurs at the range-bin where the target is located. The target range was estimated by detecting the peak of the maximum power of the correlator output in the slow time direction. However, the position of the peak may drift from the real target position because of multipath. Using this method, estimation can be made of the position of the human body where the radar signals are reflected. This occurs because the first drop in the skewness value happens at this point.

Comparison Between the Proposed Algorithm and the State-of-the-art RMD Algorithm for Target Detection in a Specific Range-bin:

The proposed algorithm has the following advantages over the developed RMD algorithm:

- The algorithm can discriminate between multiple targets.
- The algorithm uses SVD combined with the skewness method to reduce the false alarms.
- The algorithm can estimate which singular value contains the target information.
- An assumption is not made neither about a constant false alarm level nor of a specific singular value related to the target information .
- An adaptive threshold value in the detection decision was not assumed. Only an abrupt change is detected in the skewness value of the amplitude distribution for the range profile in all range-bins.

It was observed that at least 20 seconds collected signals in the slow time direction are needed to detect the target and estimate the breathing rate. Although the observation of a drop in the skewness value for the correlator output squared is enough to detect a target, the value of the threshold was assumed to be as presented in Eq. 4.15. This threshold value may differ from one radar system to another to fit the capability for detecting this drop in the skewness value.

Discrimination Between Two Targets:

The proposed algorithm for detecting single target is applied iteratively. It relies on detecting the closest target initially based on the skewness position. A drop in the skewness value happens at the first target range-bin. This allows for detection of the first target that is closer to the radar even if he/she is breathing shallower than the second target that is further away. After the first target is detected, the process is continued until the second target is detected starting from the first iteration. The algorithm starts to search for a second target by applying the single target detection algorithm iteratively. SVD is applied iteratively to remove the contributions of the clutter and the first target. When the algorithm for detecting single target is applied iteratively, the i^{th}singular value is replaced by zeros, where i is the number of iteration. If the range-bin with the maximum power peak in i^{th} iteration passes the skewness test, a detection of a second target is recorded.

This research’s method is applied to distinguish between two targets in free space and behind a 20 cm thick gypsum wall. A distinction could not be made between two targets breathing with normal breathing and separated by 20 cm and 30 cm in free space and behind walls, respectively.

Stop breathing detection:

The proposed algorithm for single target breathing detection was able to detect a human breathing for 20 seconds and stop breathing for another 20 seconds The range of the target was estimated accurately. Breathing rate estimation algorithms can be applied to the breathing signal at the estimated range-bin. Different breathing rate estimation methods were discussed in Chapter three. In this research, we use the zero-crossing method combined with breathing pulse interval constrain to estimate the breathing rate. The stop breathing event was detected and the breathing rate was estimated in a short time interval (20 seconds).

Limitations:

The following limitations may prohibit discrimination between multiple targets:

- Distinction between two targets is difficult when the two targets are facing the radar and standing behind each other. The signal reflected from the second target will be attenuated after passing through the first target. Also, the two signals reflected from the two targets will interfere. This makes the discrimination between the two targets very difficult.
- When the two targets are standing at the same distance from the radar, the distinction between them becomes very hard. Although the two targets may be standing at different angle from the radar, the reflected waves may reach the receiver at the same range-bin. However, in this scenario, multiple receivers can be used to distinguish between multiple targets at the same range from one receiver.
- The waves reflected from a subject may reflect again from any object in the room. This causes a multipath wave. This wave appears as a shadow of the real target at a distance larger than the real distance. This shadow needs to be removed to distinguish between multiple targets.

Chapter 5

Breathing Rate Estimation

5.1 Introduction

In this Chapter, the fourth main block of the proposed algorithm which is the breathing rate estimation is presented as illustrated in Fig. 3.1. It was observed that two main parts of the human body move while breathing: the chest and the abdomen. The contribution of the abdomen movements results in multiple harmonics of the breathing signals. The major source of errors in the human breathing estimation algorithms originates with the second harmonic magnitude which may be higher than the first harmonic magnitude in some scenarios [*29*,*30*]. The second harmonic frequency may be detected as the human breathing rate and high errors are expected.

Although many breathing rate estimators have been presented in the state-of-the-art [*36*,*37*,*38*], none of them addressed the problem of the second harmonic. Two methods, including the moving average filter method and ellipse fitting method have been used to reduce the error in the estimated breathing rate [*30*]. However, it was observed that the error is high in some measurements [*29*,*30*]. The novel idea here is that a moving average sliding window was applied at the possible breathing frequency with the goal of reducing the second harmonic magnitude. This approach guaranteed detecting the maximum magnitude of the breathing signal spectrum at the real breathing rate. Subsequently, a comparison was made between the state-of-the-art algorithms. As a result, a new method using zero-crossing technique was proposed.

The human lung has a volume range of 4 to 6 litres and the tidal volume is between 500 ml to 800 ml. As a result, the chest wall moves between 10 and 20 mm towards the radar [*6*]. When a human target is illuminated by an electromagnetic wave, the reflected wave is modulated by the periodic movement due to breathing. A simple way to track the chest wall movements is to study the ToA of the amplitude peaks in a range-bin. Interference, the multipath effect, and the amplitude attenuation in the reflected signal will affect the peak positions and the breathing Pulse-To-Pulse (PTP) intervals. The breathing on average for newborns rate is 0.62 Hz or 37 breaths per minute. While adults breathe on average 10-14 breaths per minute [*105*]. The average adult breathes in and out every 4.2- 6 seconds. If we disregard the PTP intervals that are less than 1.5 seconds and more than 11 seconds, estimation can be made of the average PTPs. Zero-crossing method can detect the intervals between true peaks by omitting the peaks outside of the breathing time interval boundaries.

In the approach used in this research, the zero-crossing method was used with one physiological constraint in order to compute the mean value and the standard deviation of PTPs in order to readjust the bandwidth of the IIR BPF. The physiological constraint included the repeated breathing pulses every 1~11 seconds. This method can reduce the effect of the breathing frequency harmonics. After that STFT or DFT was applied to the algorithm output to estimate the breathing rate. Not only can the frequency of the chest movement be detected in a short time window (~20 seconds), but also, any changes in the breathing rate can be noted. The detection of breathing rate variability can initiate a stress level mark in a human breathing pattern. To the best of the author’s knowledge, PTP adjustable BPF method in this application has not been used in this application.

5.2 Human Breathing Signal Received in PN-UWB Radar

In this section, a mathematical model of the breathing signal received in PN-UWB radar is proposed. The reason for proposing this model is for the purpose of understanding the spectrum of the breathing signal and to determine why the error in the estimated breathing rate is high in some scenarios [*29,30*]. The mathematical model illustrated that at some scenarios the second harmonic magnitude is higher than the first one. This was observed when the magnitude of the spectrum at the breathing rate, or its harmonic, was computed using Eq. 5.14.

Thoracic and abdominal movements are the two important movements related to breathing. However, most of the research in human breathing detection has considered only thoracic movements in modeling the breathing signal.

Only recently, human breathing signal was assumed to consist of superposition of returns from thorax and abdominal movement in [*96*] while using continuous wave radar for Doppler-based breathing rate estimation. The human body was modeled as two cylinders, one corresponding to the thorax and the other corresponding to the abdomen with different displacements and possible phase offsets. However, the phase variation due to the movements of thorax and abdomen was modeled as a sinusoid. Although [*95*] considered breathing signal to be non-sinusoidal when using UWB radar, it did not explicitly analyze the signal as a superposition of returns from the thorax and the abdomen. Interestingly, in [*48*], it was observed that on an average, the displacement of the abdomen was at least four times that of the chest; hence, it was necessary to incorporate the contributions of abdomen into the model as suggested in [*48*]. It was observed that the breathing signal obtained from the thorax and the abdomens, using a breathing belt based on a piezo-electric sensor produced by CleveMed ™, Cleveland, USA are non-sinusoidal. As a result, the two cylinder model used in [*96*] along with the non-sinusoidal model proposed in [*95*] was adopted and new method of breathing rate estimation is presented.

Considering a human body modeled as two cylinders, the top represents the thorax and the bottom represents the abdomen. In addition, a PN UWB radar transmitter and receiver are placed at location x_T and x_R while the nominal chest and abdomen position (air skin interface) is at location x_c and x_a of a stationary human target.

The signal at the receiver $d(t)$ obtained after reflecting off the chest and abdomen of a human target positioned at distance d_0 is given by $d(t)$ as shown in Fig. 5.1:

$$d(t) = d_0 + m_c(t) + m_a(t) \tag{5.1}$$

$$= d_0 + \sum_{i=1}^{M} c_i \, sin(2\pi i f_b t) + \sum_{j=1}^{N} a_j \, sin(2\pi j f_b t) \tag{5.2}$$

where c_i are harmonic components of chest displacement and a_j are harmonic components of abdomen displacement, f_b is the breathing frequency. M and N represent the number of significant components of the chest and abdomen displacements respectively.

Since radar does not have enough resolution to identify heart motion, the displacement due to heart is ignored. The radar used in this thesis provided a correlated output as shown in Appendix C. The correlated output can be represented as the sum of responses of the channel, and the variation due to chest and abdomen:

$$r(t,\tau) = \sum_i A_i p(\tau - \tau_i) + Ap(\tau - \tau_d(t)) \tag{5.3}$$

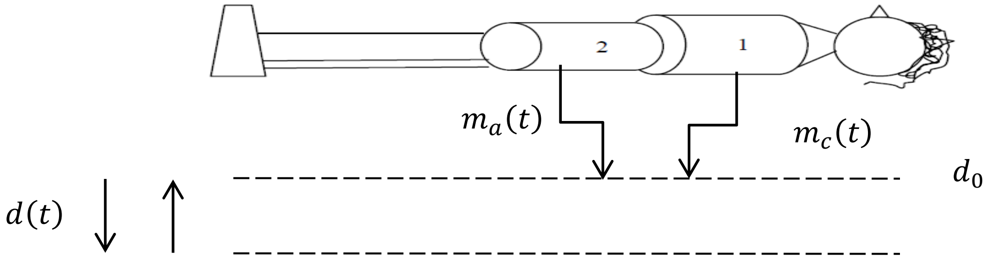

Figure 5.1 Human breathing signal model.

where $p(t)$ is the correlator output, A_i is the correlator output related to the i-th static multipath component, τ_i is its delay, and A is the correlator output as related to body reflection. The time delay $\tau_d(t)$ associated with chest and abdominal movement is modeled as the sum of time-of-flight τ_0 with two composite delays as shown below:

$$\tau_d(t) = \tau_0 + \sum_i^M \tau_i \, sin(2\pi i f_b t) + \sum_j^N \mu_j sin(2\pi j \, f_b t) \tag{5.4}$$

where $\tau_0 = \frac{2d_0}{c}$, $\tau_i = \frac{2c_i}{c}$, $\mu_j = \frac{2a_j}{c}$, and c is the speed of light. The sampled correlator output is obtained in discrete instants in slow time $t = kT_s$, $k = 1, \dots, K$ at discrete fast sample time $\tau = lT_f$, $l = 1, \dots, L$ and is stored as a matrix.

Since the environment was static, the static clutter component appeared as DC-component in the slow-time direction and was removed by using pre-processing algorithm. Let the clutter free signal, $y(t, \tau)$, contains only the movements related to the chest and the abdomen and is given by:

$$y(t, \tau) = Ap(\tau - \tau_0 - \sum_{i=1}^M \tau_i \, sin(2\pi i f_b t) - \sum_{j=1}^N \mu_j sin(2\pi j \, f_b t)) \tag{5.5}$$

Figure 5.2 (a) and (b) are the chest and the abdomen breathing signals recorded by the breathing belt, respectively. Figure 5.2 shows that the displacements of the abdomen cannot be ignored and should be considered in all UWB radar human breathing detection models. Figure 5.3 (a) and (b) are the DFT of the recorded signals in Fig. 5.2 (a) and (b), respectively. Multiple frequency harmonics of the breathing frequency were observed in the DFT of the abdomen breathing signal. This indicates that the displacement of the chest and the abdomen are not sinusoidal. It can be assumed that the chest movement is sinusoidal and the abdominal displacement is semi- sinusoidal. However, the movements of the chest and the abdomen may differ from one human to another.

If it is assumed that the chest movement is sinusoidal ($M = 1$) and the abdominal movement is composed of the fundamental frequency (first harmonic) and the second harmonic ($N = 2$), then the above equation becomes:

$$y(t, \tau) = Ap(\tau - \tau_0 - (\tau_1 + \mu_1) \cdot sin(2\pi f_b t) - \mu_2 \, sin(4\pi f_b t)) \tag{5.6}$$

The Fourier transform of $y(t, \tau)$ along the slow time can be expressed as follows:

$$Y(f, \tau) = \int_{-\infty}^{+\infty} y(t, \tau) e^{-j2\pi f t} dt \tag{5.7}$$

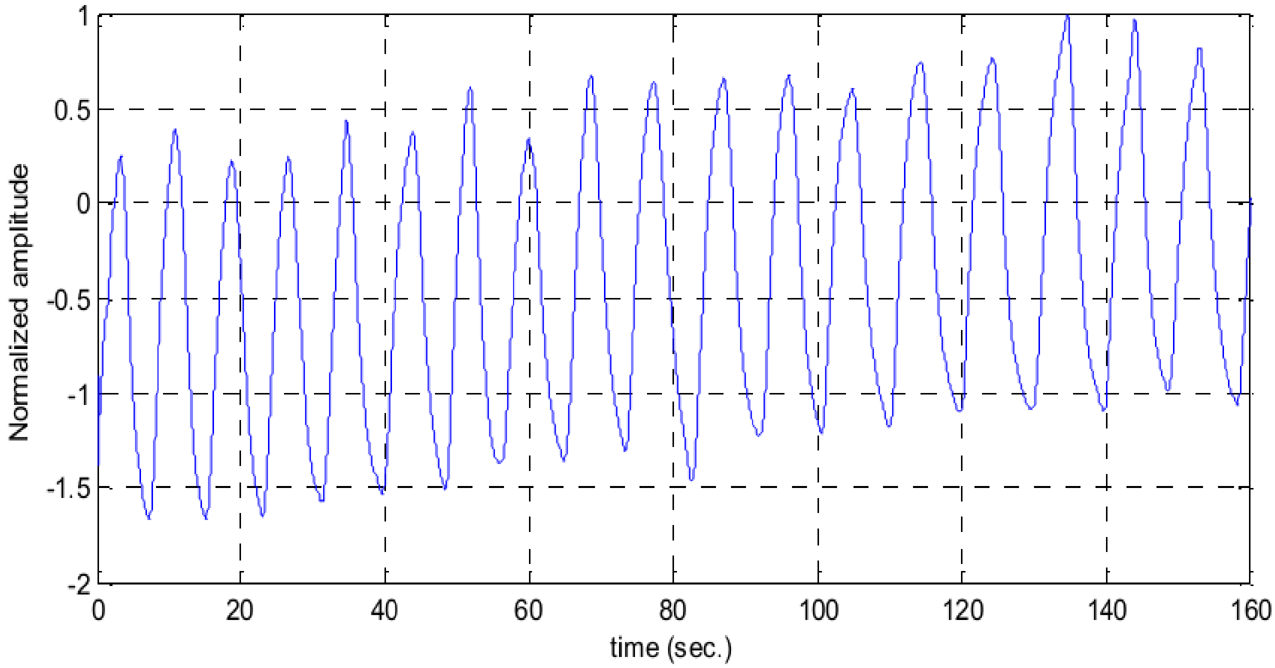

(a)

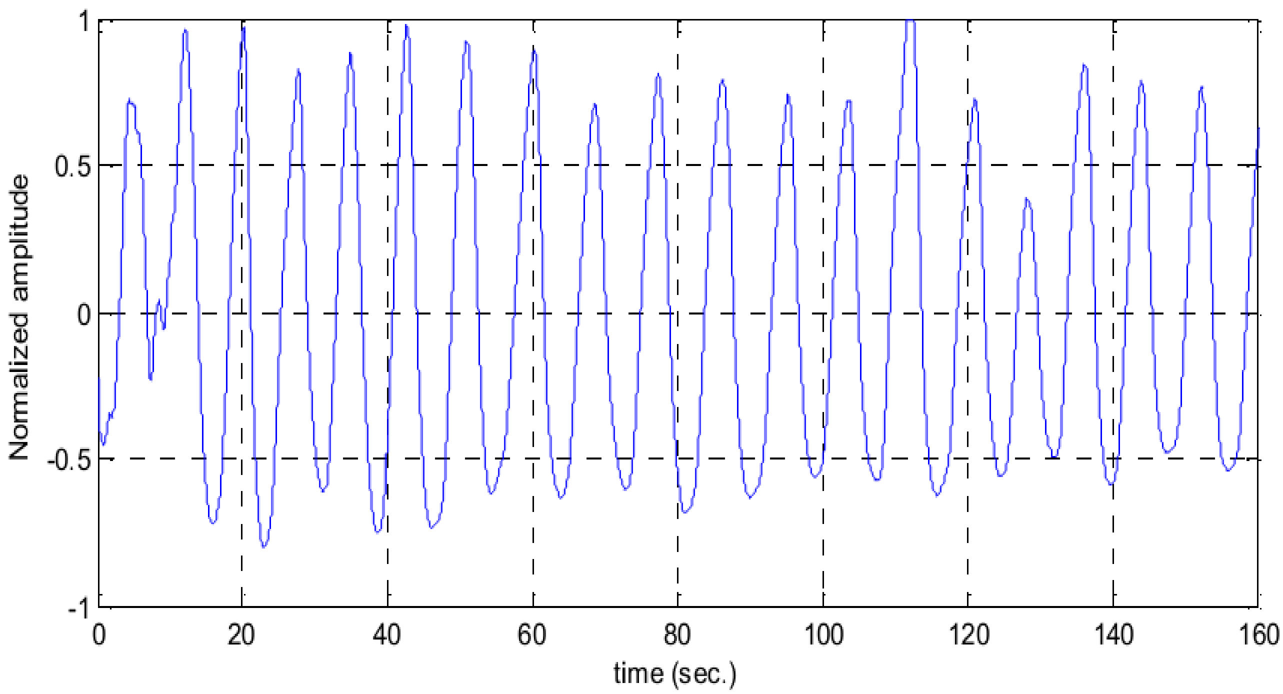

(b)

Figure 5.2 (a) Chest breathing signal (b) Abdominal breathing signal recorded by a piezo-electric breathing belt.

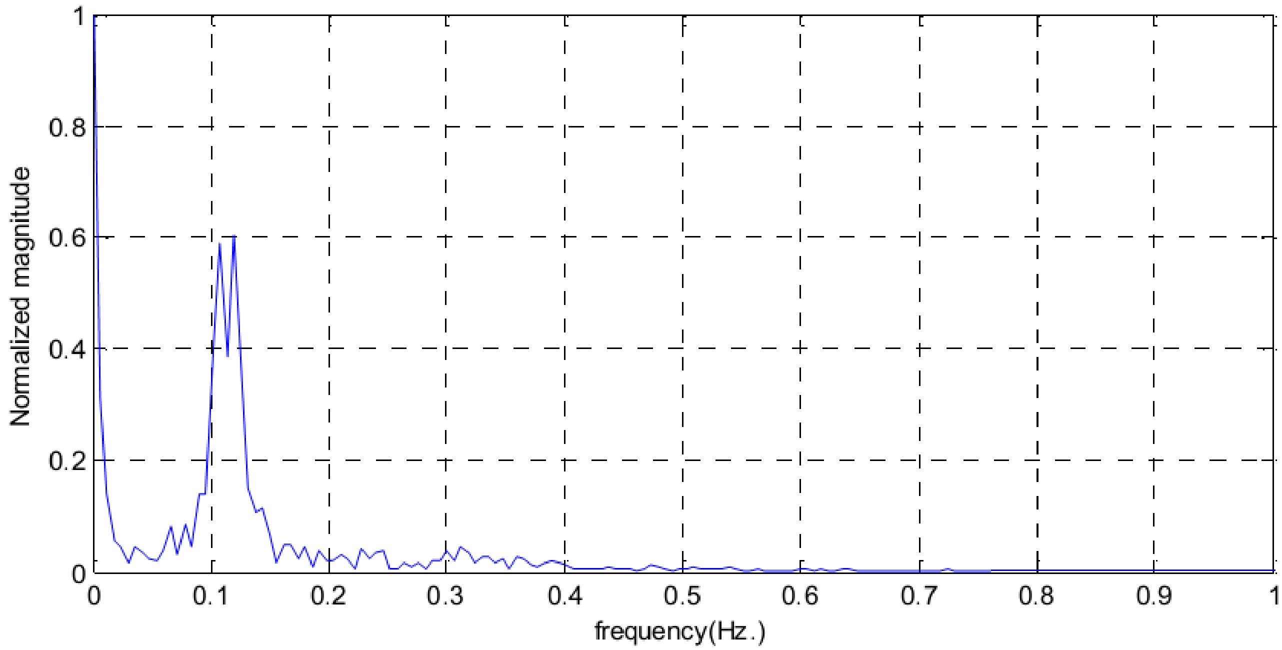

(a)

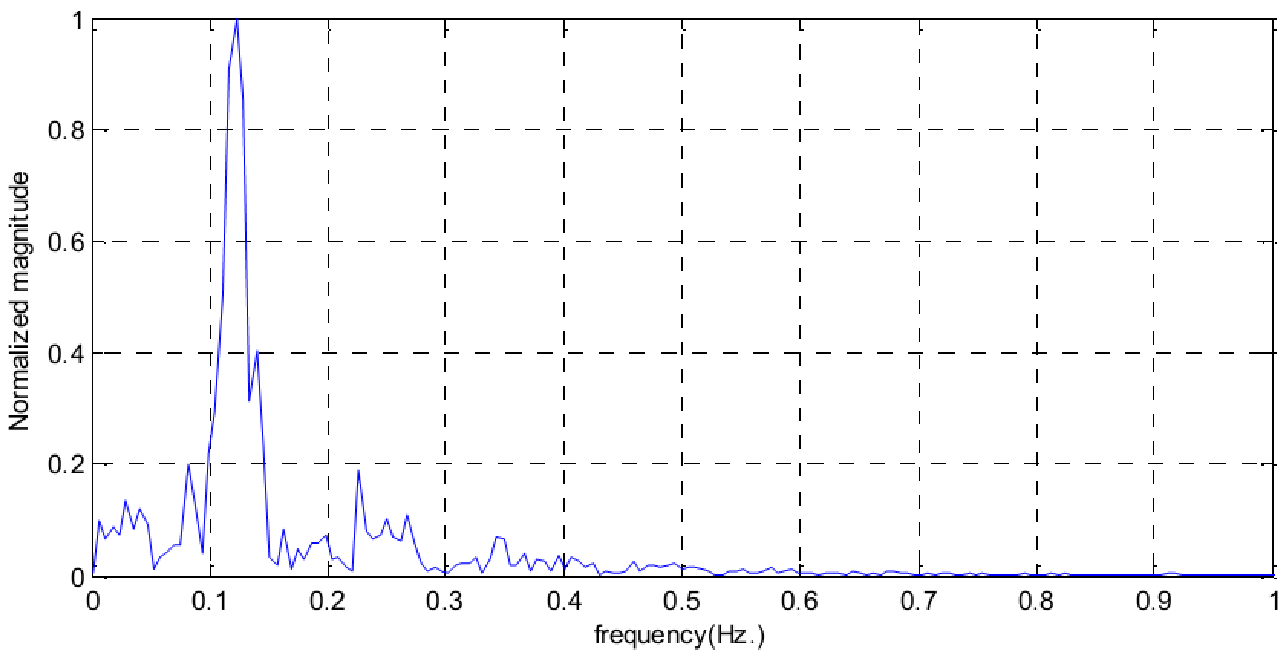

(b)

Figure 5.3 (a) FFT of chest breathing signal (b) FFT of abdominal breathing signal recorded by a piezo-electric breathing belt.

and can be obtained from the 2-D Fourier transform as follows:

$$Y(f,\tau) = \int_{-\infty}^{+\infty} Y(f,\nu)e^{j2\pi\nu\tau}d\nu \tag{5.8}$$

The 2-D Fourier transform $Y(f,\nu)$ can be written as follows

$$Y(f,\nu) = AP(\nu)e^{-j2\pi\nu\tau_0}\int_{-\infty}^{+\infty}(S_1S_2S_3)e^{-j2\pi ft}dt \tag{5.9}$$

where $P(\nu)$ is the Fourier transform in the fast time of the correlated pulse and:

$$S_1 = \sum_{k=-\infty}^{+\infty} J_k(\beta_{\tau_1}\nu)e^{-j2\pi kf_bt} \tag{5.10}$$

$$S_2 = \sum_{l=-\infty}^{+\infty} J_l(\beta_{\mu_1}\nu)e^{-j2\pi lf_bt} \tag{5.11}$$

$$S_3 = \sum_{m=-\infty}^{+\infty} J_m(\beta_{\mu_2}\nu)e^{-j2\pi m(2f_b)t} \tag{5.12}$$

where $\beta_x = 2\pi x$ and $\sum_{p=-\infty}^{+\infty} J_p(z)e^{-j2\pi pf_0t} = e^{-jzsin(2\pi f_0t)}$ is the series of Bessel functions.

After substituting and simplifying, it can be shown that at $\tau = \tau_0$

$$Y(f,\tau_0) = A\sum_{k,l,m=-\infty}^{+\infty} C_{klm}\delta(f-(k+l)f_b-m(2f_b)) \tag{5.13}$$

where

$$C_{klm} = \int_{-\infty}^{+\infty} P(\nu)J_k(\beta_{\tau_1}\nu)J_l(\beta_{\mu_1}\nu)J_m(\beta_{\mu_2}\nu)d\nu$$

Furthermore using mean value theorem C_{klm} can be evaluated as follows [*31*]:

$$C_{klm} \approx \Delta f.J_k(\beta_{\tau_1}f_c)J_l(\beta_{\mu_1}f_c)J_m(\beta_{\mu_2}f_c)P(f_c) \tag{5.14}$$

where Δf is the pulse bandwidth. The above equation indicates that the slow time spectrum is discrete and it has spectral lines at frequencies of the harmonics for the breathing frequency. These harmonics are intermodulation products of the chest and abdominal movements. The amplitude of each intermodulation product for a frequency $f = (k+l)f_b + m2f_b$ is determined by the coefficient C_{klm}.

From equations 5.5 and 5.13, the signal $y(t,\tau)$, as reflected from a human breathing at a target estimated range-bin, has multiple frequency components varying with time. In Eq. 5.13, if the movements of the chest and the abdomen are not pure sine waves, the breathing spectrum will contain more frequency lines and extracting the human breathing rate becomes more complicated. In some scenarios, the second harmonic magnitude becomes dominant and it is necessary to reduce the effect of the second harmonic in order to estimate the real breathing rate. Figure 5.4 (a) illustrates the DFT of the human breathing as detected in a range-bin estimated by the proposed detection algorithm in the previous Chapter. Figure 5.4 (b) illustrates the STFT of the same signal using a window time equal to 20 seconds , an overlap ratio equal to 50%, and utilizing a Hann window in the frequency domain, respectively. The target was sitting 2m from the radar in an office environment and breathing with normal breathing. Figure 5.4 shows that the breathing signal had multiple frequency components and the second harmonic was dominant. A simple way to track the chest wall movements is to study the ToA of the amplitude peaks in a range-bin.

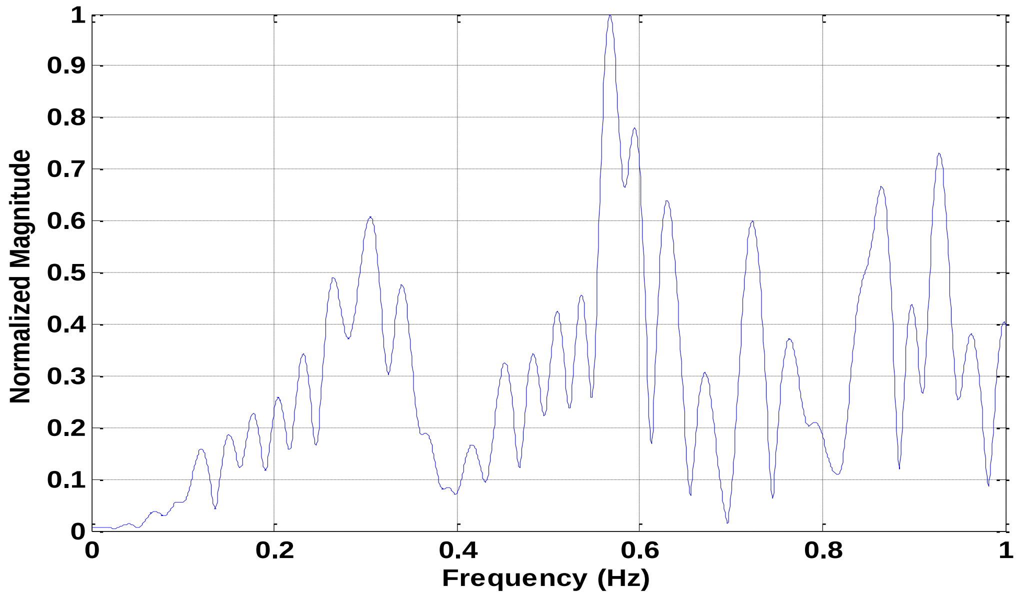

(a)

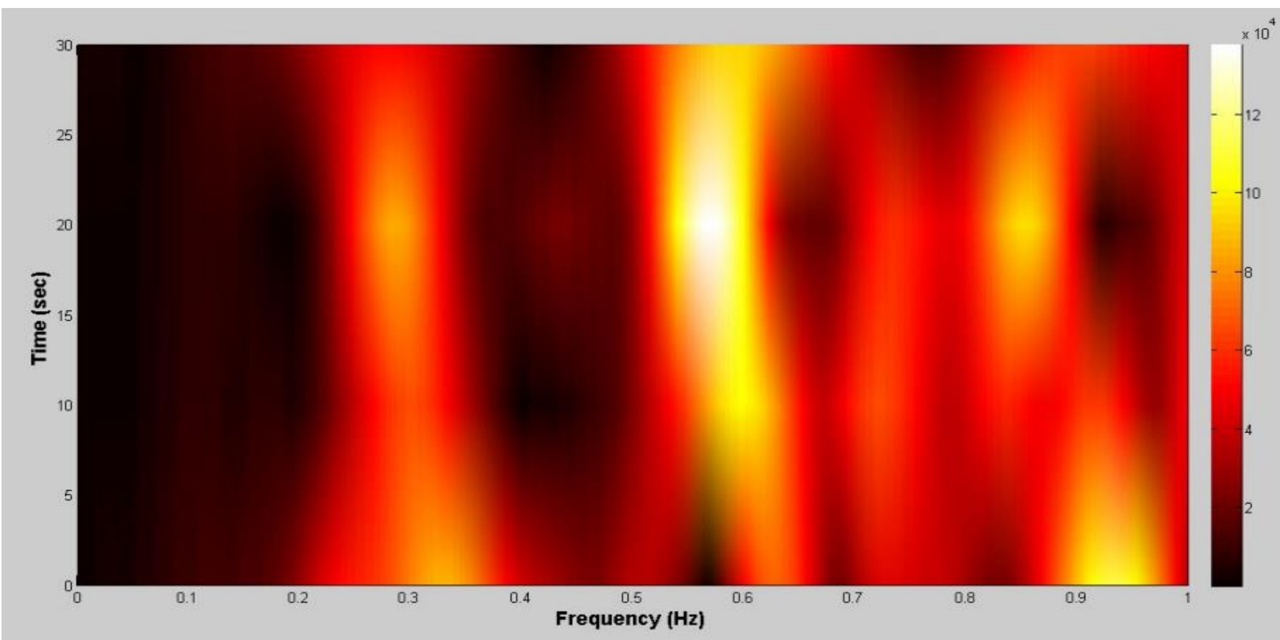

(b)

Figure 5.4 (a) The DFT of the human breathing signal (b) STFT of the human breathing signal.

5.3 Human Breathing Rate Estimation

Many frequency and phase estimators and transforms have been introduced in several signal processing applications. One of the most famous transforms is the FFT [*92*]. The accuracy of several FFT-based MLEs estimators was discussed in [*92*,*106*,*107*,*108*,*109*].

The Zero-crossing phase and frequency estimator which include three refinement methods have been proposed in [*92*]. Lio compared FFT with the zero-crossing phase and frequency estimators. The simulated results showed that the zero-crossing frequency and phase estimators can provide high estimation accuracy and low computational complexity. Although the FFT-based MLE can provide a high accuracy of estimation, the latency can be prohibitive in some scenarios because the FFT can only be performed after receiving the entire signal [*92*].

Coarse estimation of the human breathing rate can be performed by counting the breathing pulses and rejecting the non-breathing pulses. The breathing pulses repeat every 1.6~6 seconds [*105*]. The time interval between the sequential breathing pulses can be used to accept/reject a breathing pulse. The zero-crossing technique accepts/rejects the breathing/non-breathing pulse and offers breathing rate coarse estimation. The coarse human breathing rate estimation can be refined by using an adjustable bandpass filter which is based on the human breathing time intervals constraint combined with one of the accurate frequency and phase estimators. Once the effect of the breathing harmonics or any other unwanted frequency components is removed, the breathing signal will be ready for applying the selected estimator.

5.3.1 Human Breathing Rate Estimation Using FFT-based MLE

In this section, an examination of the four distinct FFT estimators in the human breathing rate estimation was carried out (see Section 3.2.4.1). A comparison was made of the breathing rate estimation accuracy for each of these methods. The frequency estimation error for each method was computed for the purpose of proving which method performed best.

Many methods have been used in pitch estimation in audio analysis applications such as Comb filters [*110*], autocorrelation [*111*], and harmonic summation [*112*]. Estimation of the fundamental frequency in a multi-harmonics signal has been discussed in [*112*]. In our application, it was necessary to reduce the error in the estimate due to the presence of the second harmonic. The harmonic summation method presented in [*112*] was adapted in this research. Three windows were centered at the first two multiples of the fundamental breathing frequency. Then, the magnitude value at the fundamental frequency was replaced by the summation of the magnitudes after applying the three windows. Finally, the three windows were slid on every possible human breathing frequency (0.1~0.8 Hz) and the magnitude values were updated at these frequencies. Using this method, it can be guaranteed that the magnitude at the fundamental breathing frequency will be higher than the magnitude of the second harmonic.

A moving average window of length $M_w + 1$ at the frequencies f_i, $2f_i$ and $3f_i$ was applied to the output of the FFT estimator, where, i is the DFT frequency point index and is equal to $\left\|\frac{f_b.N_{FFT}}{f_s}\right\|$, f_b is the breathing frequency and it is changing from $f_{bl} = 0.1\ Hz$ to $f_{bh} = 0.8\ Hz$. In addition, N_{FFT} is the number of the DFT frequency points, and f_s is the sampling frequency in the slow time dimension. $|Y(f,\tau)|$ is multiplied with the moving average rectangular window $W(\ i,\tau)$ at frequencies f_i, $2f_i$, and $3f_i$. At the frequency points i, $2i$, and $3i$ all the magnitudes of $|Y(f,\tau)|\ \times\ W(\ i,\tau)$ are added, then slide the window on all the frequency points N_{FFT} and determine the summation of the magnitude at every point. Figure 5.5 shows the process of eliminating the effect of the second harmonic. The output of the process will be $Y_W(i,\tau)$ and can be presented by the following equation:

$$Y_W(i,\tau) = \sum_{i-M_w/2}^{i+M_w/2} |Y(f,\tau)| \times W(i,\tau) + \sum_{2i-M_w/2}^{2i+M_w/2} |Y(f,\tau)| \times W(2i,\tau) + \sum_{3i-M_w/2}^{3i+M_w/2} |Y(f,\tau)| \times W(3i,\tau) = w_1 + w_2 + w_3 \tag{5.15}$$

The Maximum Likelihood Moving Average (MLMA) estimated breathing frequency $\hat{f}_{MLMA}$ can be computed from Eq. 3.11 as:

$$\hat{f}_{MLMA} = arg \underbrace{max}_{i \in [\frac{f_{bl} \cdot N_{FFT}}{f_S} : \frac{f_{bh} \cdot N_{FFT}}{f_S}]} Y_W(i,\tau) \tag{5.16}$$

The steps of applying the method are:

- Apply three windows with length equal to $M_w + 1$ at the lowest possible human breathing frequency point i and its second and third harmonic, $2i$ and $3i$ to the DFT of the breathing signal.
- Sum all the magnitudes of the three windows and update the magnitude of the spectrum at i to this value.
- Move the three windows to $i + 1$, $2(i + 1)$, and $3(i + 1)$.
- Repeat the second and the third step until i reaches the highest possible human breathing frequency point.
- $\hat{f}_{MLMA}$ is computed using Eq. 5.16.

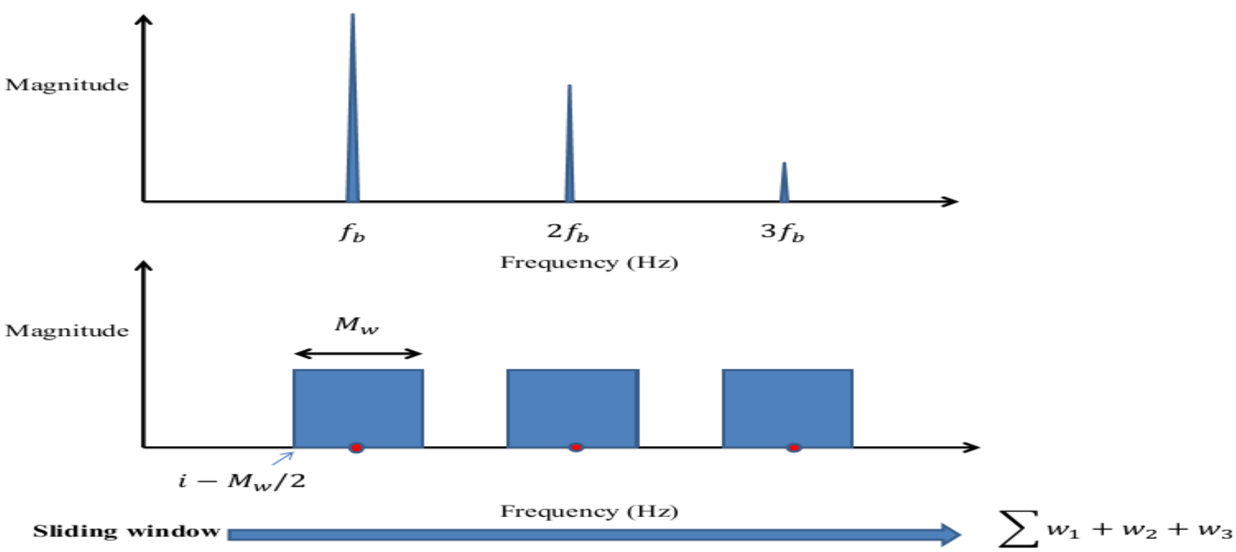

Figure 5.5 Process of transforming the spectrum using three windows. The first one is slid in small frequency increments while the other two are placed at frequencies two and three times higher than the center frequency of the first window.

In this research, the DFT was applied with the number of frequency points equal to 2^{16}. It was found that a moving average window length equal to 1% of the breathing frequency (4 points in the case of breathing rate ~0.3Hz) is enough to eliminate the effect of the second harmonic in the human breathing spectrum. The error in the estimated breathing rate increases with longer windows and lower SNR. Different types of windows (rectangular, Gaussian, Hann, and Hamming windows) were applied and it was found that the rectangular window outperformed the other widows.

Figure 5.6 (a) shows the breathing signal reflected from a human breathing with normal breathing and sitting 2m from the radar. Figure 5.6 (b) is the DFT of the received signal before applying the three windows. Figure 5.6 (c) is the modified spectrum after applying the three windows. Using DFT, a peak was detected at the second breathing harmonic. However, by using this modified spectrum summation method, the magnitude at the fundamental breathing frequency was equal to the summation of the first, second, and third breathing frequency magnitudes, and a peak was detected at the first breathing harmonic.

5.3.2 Zero-Crossing in Breathing Rate Estimation

In the two previous sub-sections, four FFT estimators, EMD, and two mean tracking algorithms were proposed in human breathing rate estimation. It can be concluded that DFT and EMD estimators are not enough to estimate the accurate human breathing rate because of two reasons:

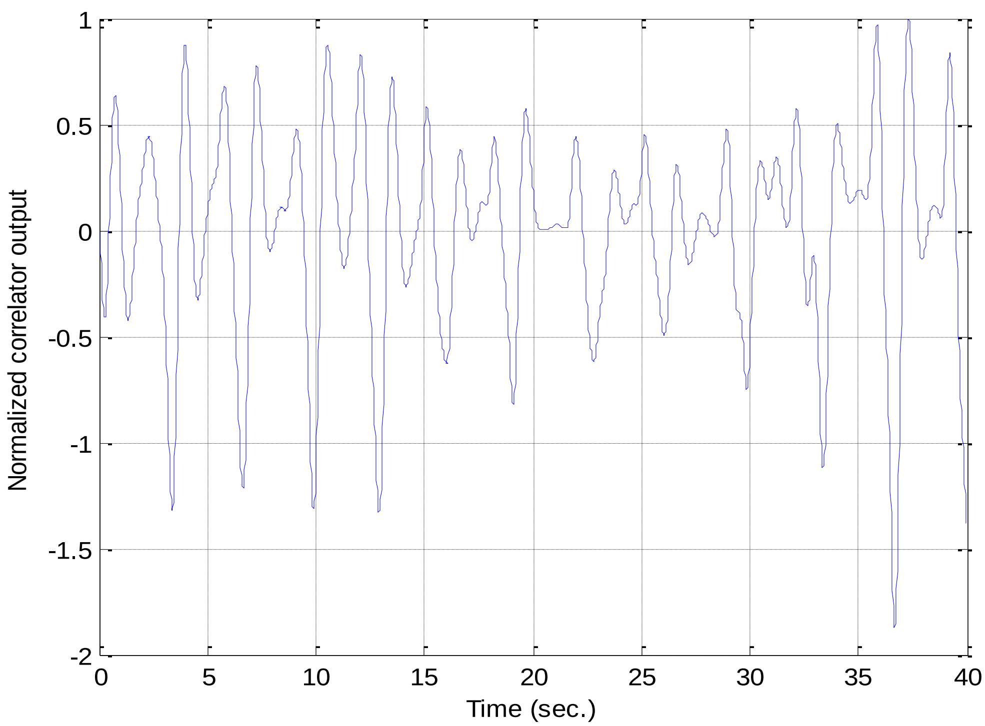

(a)

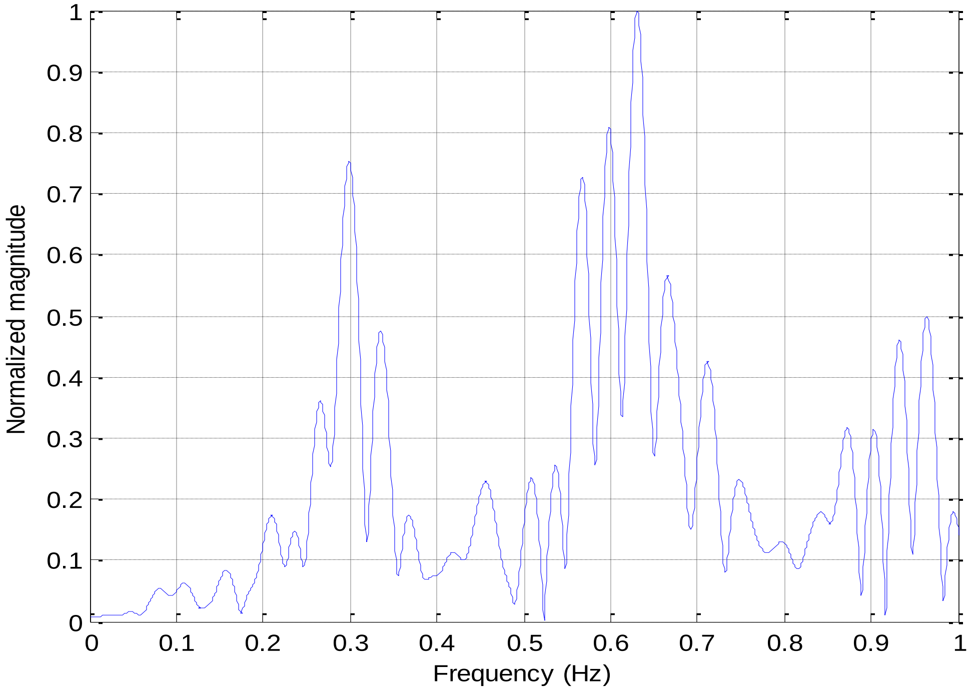

(b)

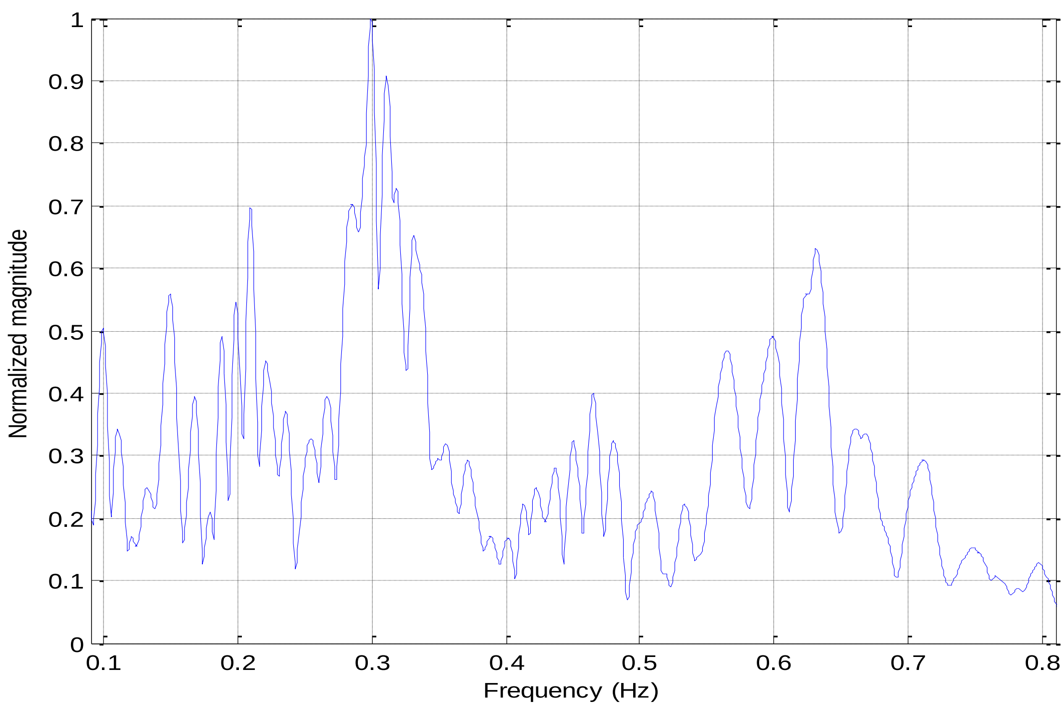

(c)

Figure 5.6 (a) The breathing signal of a human sitting 2 m from the radar. (b) DFT before applying the three windows (c) after transforming the spectrum using three windows.

- The multiple breathing frequency harmonics may have a magnitude higher than the magnitude of the first breathing frequency harmonic.
- Any human body part displacements while breathing will generate multiple frequency components which will need to be removed. These frequencies overlap with the human breathing frequency range. A method to assign which frequency is related to the breathing signal is required.

Although the mean tracking algorithms can reduce the effect of the large-scale body displacements on the breathing rate estimation, the algorithms are sensitive to the time window size and the error in the breathing rate is still high in comparison with the real human breathing rate. More advanced techniques are required.

The zero-crossing technique has been used as a frequency and phase estimator [*92*,*113*,*114*]. Zero-crossing estimators, followed by refinement methods, may have a better performance than other frequency and phase estimators in some scenarios [*92*,*115*]. An advantage of the zero-crossing method is that the properties of physiological signals can be used to remove the non-breathing human body displacements. In the following section the zero-crossing method in the human breathing rate estimation is proposed.

5.3.2.1 Coarse Human Breathing Rate Estimation

The zero-crossing algorithm operates by detecting the time instants of the zero-crossings for a specified threshold level and sorts these zero-crossings in to a vector $S = (t_1, t_2, \dots t_s)$ where s is the number of detected zero-crossings. In order to minimize the effect of the white noise, a state machine is used and a zero-crossing threshold level is assigned [*92*]. The initial threshold level assigned is equal to the standard deviation σ_s of the breathing signal amplitude. The initial upper and lower threshold level (Thr_U and Thr_l) are equal to $+\sigma_s$ and $-\sigma_s$, respectively. Figure 5.7 shows the state machine used to detect the zero-crossing s of the signal $y(t,\tau)$. Given n is the time samples index in the slow time dimension. The signal amplitude $y[n]$ or its absolute value $|y[n]|$ will be examined if it is higher or lower than a threshold as shown in Fig. 5.7. A negative-slope zero-crossing was detected on state transitions 1 → 2 and 3 → 2 when $y[n] > +\sigma_s$ or $|y[n]| \leq +\sigma_s$, and altered to be less than $-\sigma_s$. A positive-slope zero-crossing was detected on state transitions 2 → 1 and 4 → 1 when $y[n] < -\sigma_s$ or $|y[n]| \leq +\sigma_s$, and altered to be more than $+\sigma_s$. After that, a linear interpolation is required to determine the zero-crossing time when the signal crosses from state to another state.

When the signal crosses the zero line with a positive slope, Eq. 5.17 is used to determine the zero-crossing time [*92*].

$$t_n^+ = t_{n+1} - \frac{y(t_{n+1},\tau)}{\frac{y(t_{n+1},\tau)-y(t_n,\tau)}{t_n-t_{n+1}}} \tag{5.17}$$

where, t_n is the last sample in the signal in state 1 before crossing to state 2 and t_{n+1} is the first sample in the signal in state 2. When the signal crosses the zero line with a negative slope, Eq. 5.18 is used to determine the zero-crossing time [*92*].

$$t_n^- = t_n - \frac{y(t_n,\tau)}{\frac{y(t_{n+1},\tau)-y(t_n,\tau)}{t_{n+1}-t_n}} \tag{5.18}$$

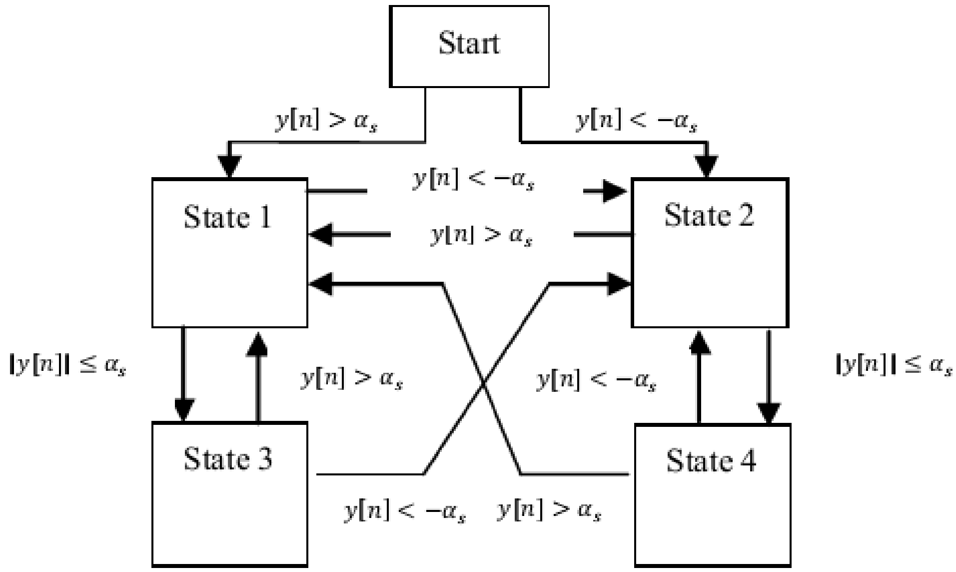

Figure 5.7 State machine implementation of the zero-crossing detector [92].

where, t_n is the last sample in the signal in state 2 before crossing to state 1 and t_{n+1} is the first sample in the signal in state 1. The vector S becomes equal to $(t_1^+, t_2^-, \dots t_s^+)$ if the first zero-crossing has a positive slope and the number of zero-crossing S are odd. The vector S becomes equal to $(t_1^-, t_2^+, \dots t_s^+)$ if the first zero-crossing has a negative slope and the number of zero-crossing S are even. The breathing pulses will be repeated every PTP interval. The PTP interval will be sorted in a vector $S_{PTP} = (P_1, \dots P_s)$. The elements of the vector S_{PTP} will be modified according to the physiological boundaries of the human breathing pulses interval to remove any pulses that are not related to human breathing. The interval between any sequential human breathing pulses should not be less than 1.5 or more than 11 seconds. S_{PTP} will be modified according to the following rule:

$$S_{PTP} = \begin{cases} P_n & 1.5 \leq P_n \leq 11, n = 1, \dots, s \\ 0 & elsewhere \end{cases} \tag{5.19}$$

A coarse estimation of the breathing rate $f_B = 1/T_B$ was computed where, T_B is the mean value of the PTPs discarding the zeros.

5.3.2.2 Fine Human Breathing Rate Estimation

For fine estimation, a 6th order IIR Butterworth bandpass filter with upper cut-off frequency f_u and lower cut-off frequency f_l determined by Eq. 5.20 and 5.21 was used to remove the higher breathing harmonics and any noise in the signal:

$$f_u = \frac{1}{T_B - a\sigma_B} \tag{5.20}$$

$$f_l = \frac{1}{T_B + a\sigma_B} \tag{5.21}$$

where σ_B is the standard division of the PTPs intervals and a is a constant. We studied the value of a by applying our human breathing rate estimation method to 27 measurements which were collected from 3 subjects breathing with normal breathing standing, sitting, and lying on his/her back 1m, 2m, and 3m from the radar and facing the transmitter and receiver antennas. Table 5.1 is the subjects' weight, height, and age. Figure 5.8 shows the absolute error in breathing rate estimation at a =0.5 to 1.8. The breathing rate estimation absolute error is minimum at $a = 1.2$. In this research's estimation algorithm, a was chosen to be equal to 1.2. However, the proposed method was not very sensitive to the value of a.

The lower and upper cutoff frequencies of the bandpass filter was adjusted based on the time interval between each breath in the time domain. First, S_{PTP} was updated according to Eq. 5.19 to remove all the pulses that are not related to breathing. The constraint was that the human breathing pulses were repeated between 1.5 seconds and 11 seconds. Second, the human breathing was coarsely estimated from the mean value of S_{PTP}. Finally, the upper and lower cutoffs frequencies of the bandpass filter were adjusted according to the mean value and the standard deviation of PTPs intervals.

Table 5.1 Subjects weight, height, and age.

Subject	Weight (Kg)	Height (m)	Age
A	132	187	40
B	97	187	37
C	77	172	35

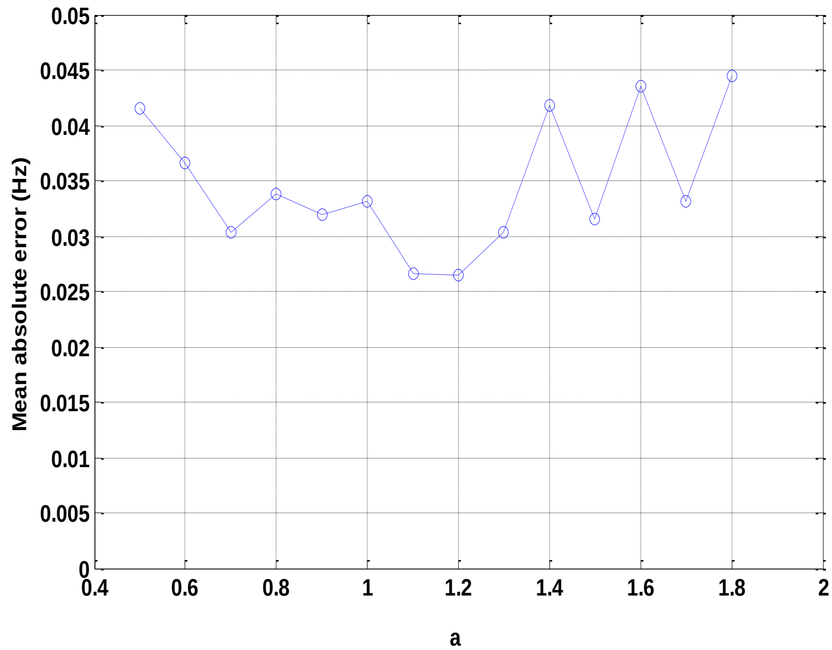

Figure 5.8 Absolute breathing rate estimation error using zero-crossing method.

Figure 5.9 is the block diagram of this research's novel human breathing rate estimation algorithm. The zero-crossing method with the state machine in Fig. 5.7 was applied to the reflected signal from the target $y(t,\tau)$. The output was the PTPs. After that, the human breathing constraint in Eq. 5.19 was applied and the output was the updated S_{PTP}. The mean value of the time intervals between the breathing pulses was used in a coarse human breathing estimation by determining $f_B = 1/T_B$. After that, the mean value and the standard deviation of the updated PTPs were used to readjust the lower and upper cutoff frequencies of IIR BPF. Then, the iteration continues until the difference between the upper and the lower cutoff frequencies, and the upper and the lower cutoff frequencies of the previous iteration of the bandpass filter were less than 0.01 Hz. If not, the output of the adjustable IIR BPF, $y_{BPF}(t,\tau)$, was applied again to the algorithm.

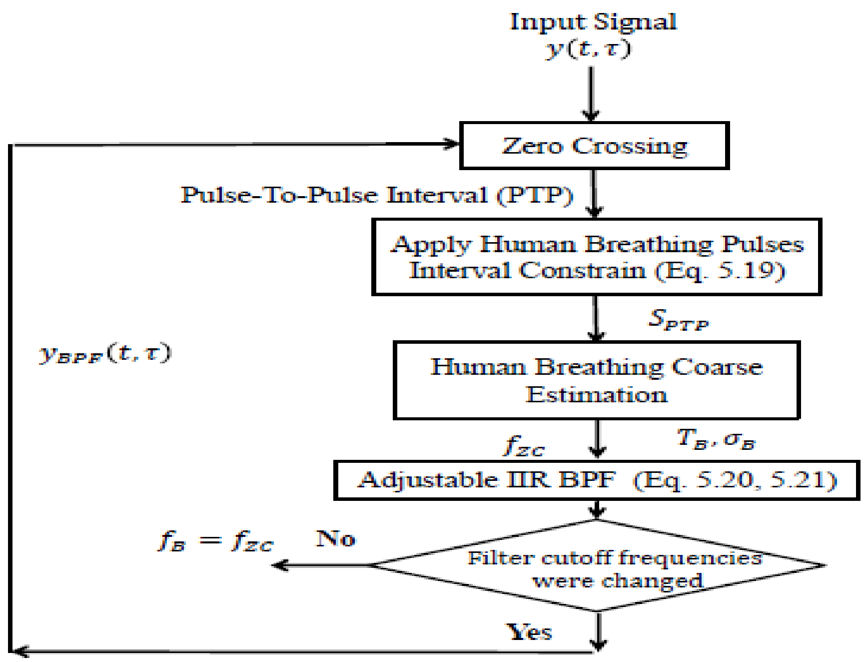

Figure 5.9 Human breathing rate estimation algorithm.

In the following section it is evident how this novel method outperforms the state-of-the-art. The signal reflected from a target standing 2m from the P410 UWB radar and breathing with a breathing rate equal to 18 breaths/min was collected in free space. The proposed range-bin estimation algorithm in Chapter 4 was applied to the collected data matrix X after applying the pre-processing algorithm. Figure 5.10 shows the normalized correlator output at the target estimated range-bin in time domain. The blue and red points show the zero-crossing s at Thr_U and Thr_l , respectively. The yellow and green points show the estimated zero-crossing s points t_n^+ and t_n^-, respectively.

Figure 5.11 (a) and (b) are the DFT and the STFT of the correlator output in Fig. 5.10 after applying the proposed zero-crossing method. Figure 5.11 (a) shows that the multiple frequency components have been removed and a peak has been detected at frequency equal to 0.35 Hz. The same results are evident in Figure 5.11 (b). The non-breathing frequency component has been removed and a breathing rate appears as high magnitude intensity at 0.35 Hz.

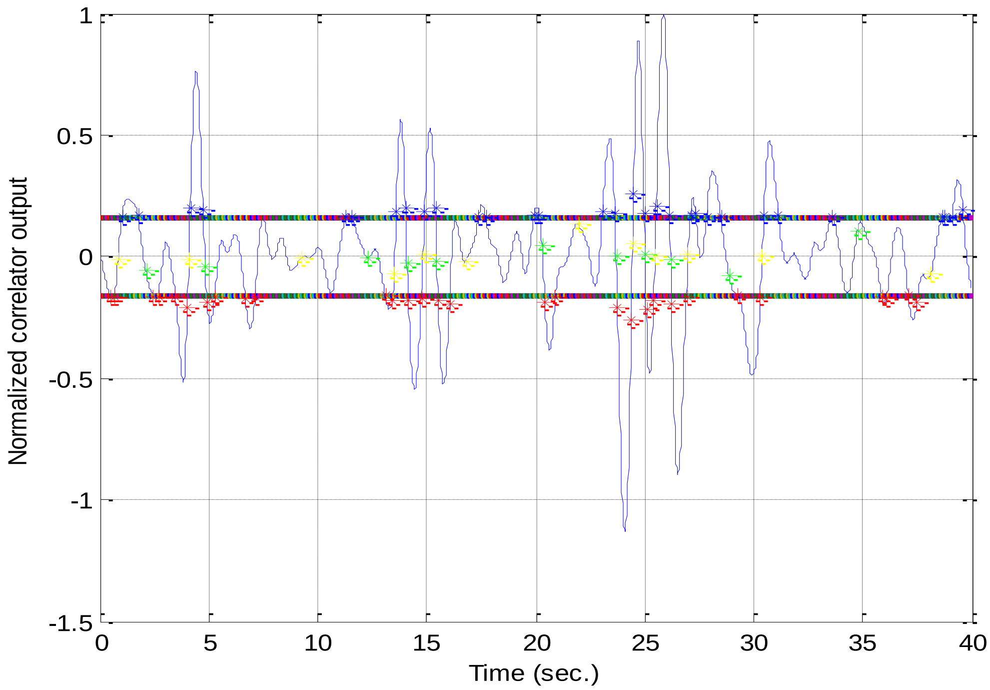

Figure 5.10 Human breathing signal in an estimated range-bin.

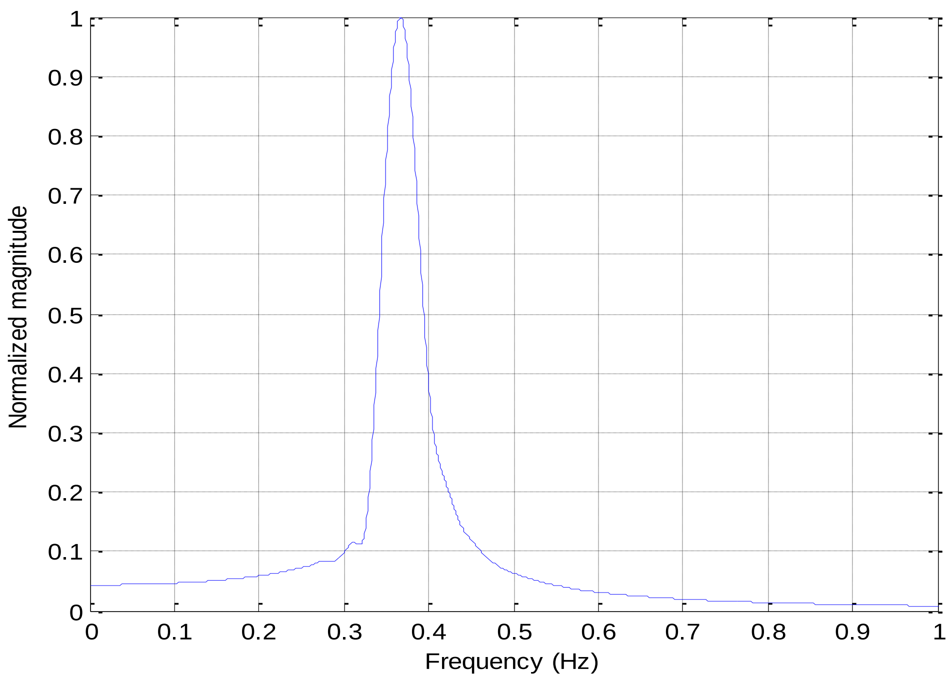

(a)

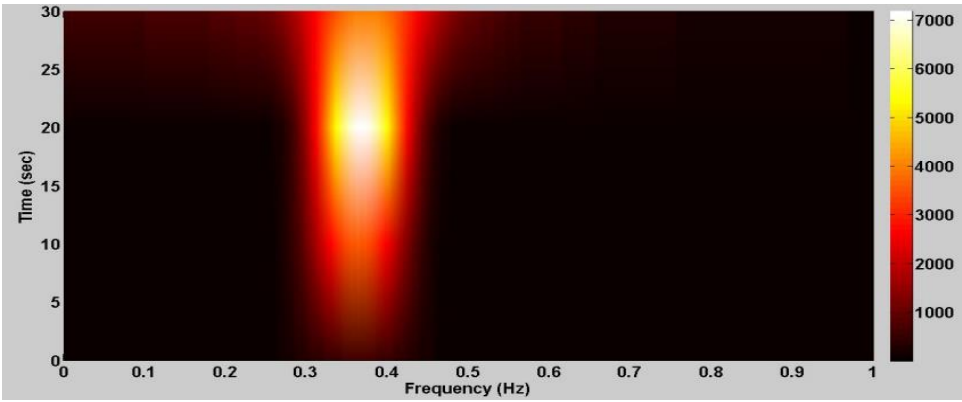

(b)

Figure 5.11 (a) The DFT of the human breathing signal. (b) STFT of the human breathing signal, after applying the presented zero-crossing method.

5.3.3 Comparison Between DFT, Mean Tracking and Zero-Crossing

A collection was made of the reflected signal from a human breathing at a breathing rate of 18 breaths/min. The subject was asked to breathe when he/she heard a tone generated by a software program and repeated every 3.33 seconds The experiments were performed in an anechoic chamber in University of Ottawa, Ottawa, Canada. The reflected signal was recorded while the target was standing, sitting, or lying down at six different angles θ from the perpendicular to the radar antenna plane. Eighteen measurements were collected at different postures and different angles.

Thirty six measurements were collected from a human breathing at different angles and postures in an anechoic chamber and an office environment. The performance of the proposed method was then compared with FFT estimators [*92*], moving average, and ellipse fitting methods [*30*]. A target was standing, sitting, or lying down 1.2 m from the PN-UWB radar with angels 0, 30, 60, 90, 135, or 180 degree from the plane of the transmitter and receiver antenna plane. Eighteen measurements were collected in the anechoic chamber and 18 measurements were collected in an office environment in University of Ottawa, Ottawa, Canada.

Figures 5.12 (a) and (b) are the mean absolute error and the variance of the absolute error of the estimated breathing rate of a human breathing with a breathing rate 18 breaths/min in an anechoic chamber using the DFT, moving average, ellipse fitting, and zero-crossing methods. The most accurate breathing rate estimation was obtained using the proposed zero-crossing method. The mean absolute error using the zero-crossing method was reduced 34.04% compared with the moving average filter method. The maximum error in the estimated breathing rate using the zero-crossing method was 32.33% of the real breathing rate while the maximum error after applying the modified harmonic summation method (see Section 5.3.1) to the DFT of the output for the moving average filter method was higher than 50% of the real breathing rate. The results in Fig. 5.12 show that the zero-crossing method outperformed the other three methods.

Figures 5.13 (a) and (b) represent the mean absolute error and the variance of the absolute error of the estimated breathing rate of a human breathing with a breathing rate 18 breaths/min in an office environment using the DFT, moving average, ellipse fitting, and zero-crossing methods.

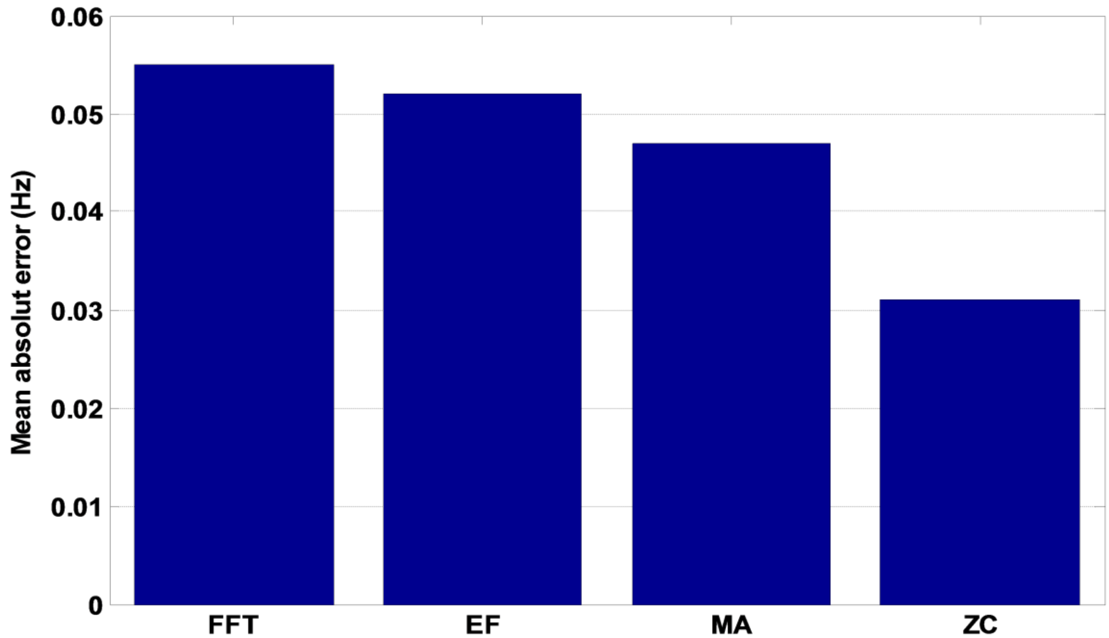

(a)

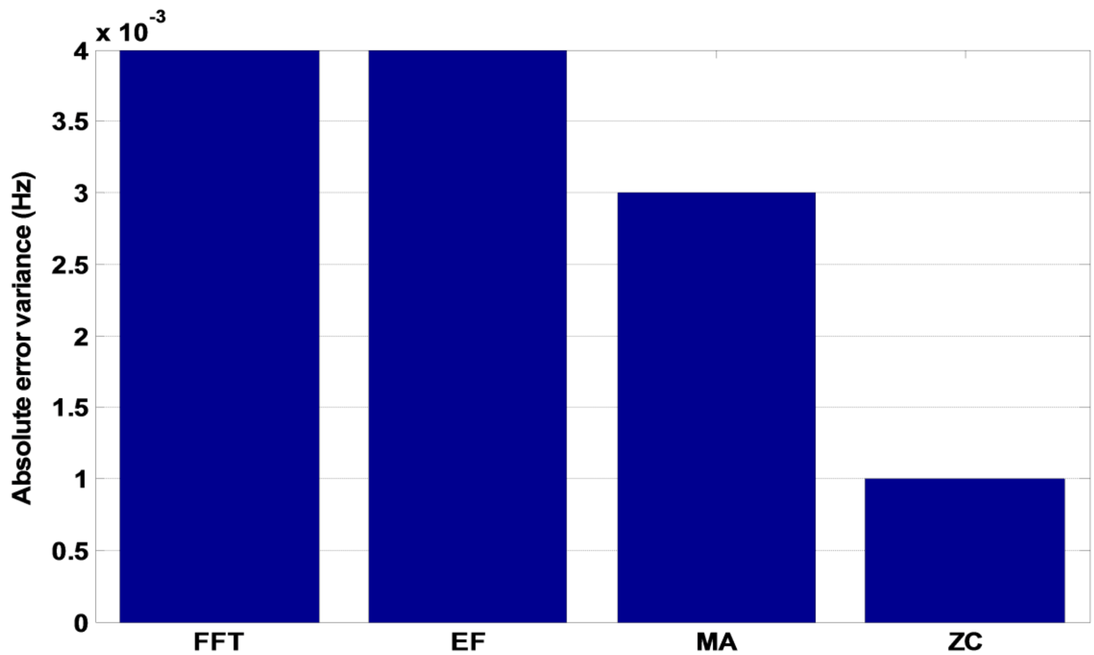

(b)

Figure 5.12 (a) The mean absolute error (b) the variance of the absolute error of the human breathing rate estimate by using the DFT, EF, MA, and ZC methods in an anechoic chamber.

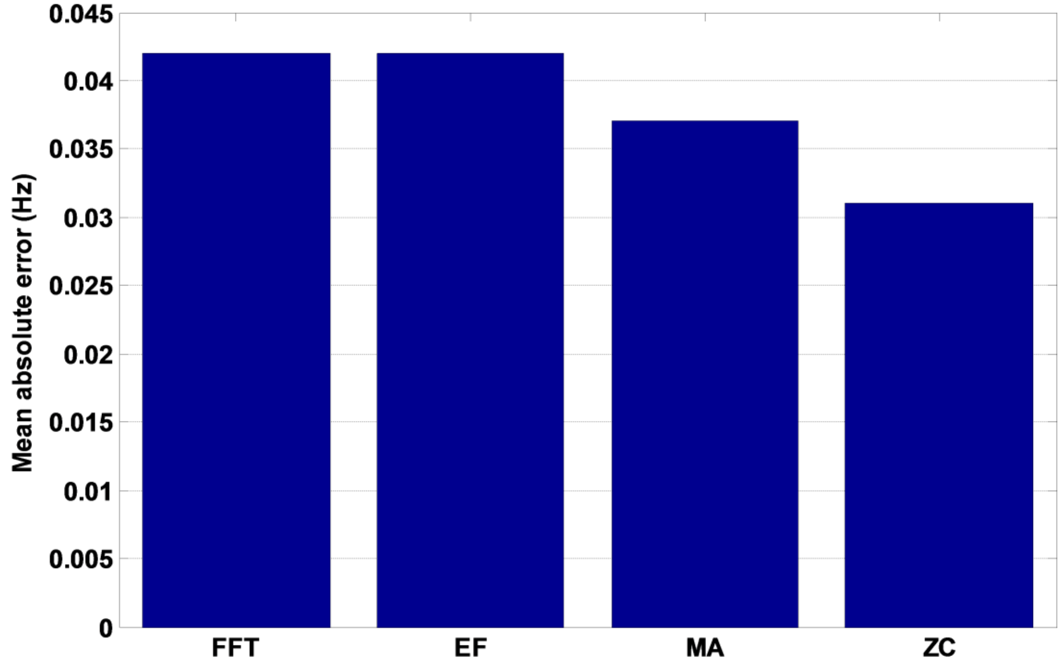

(a)

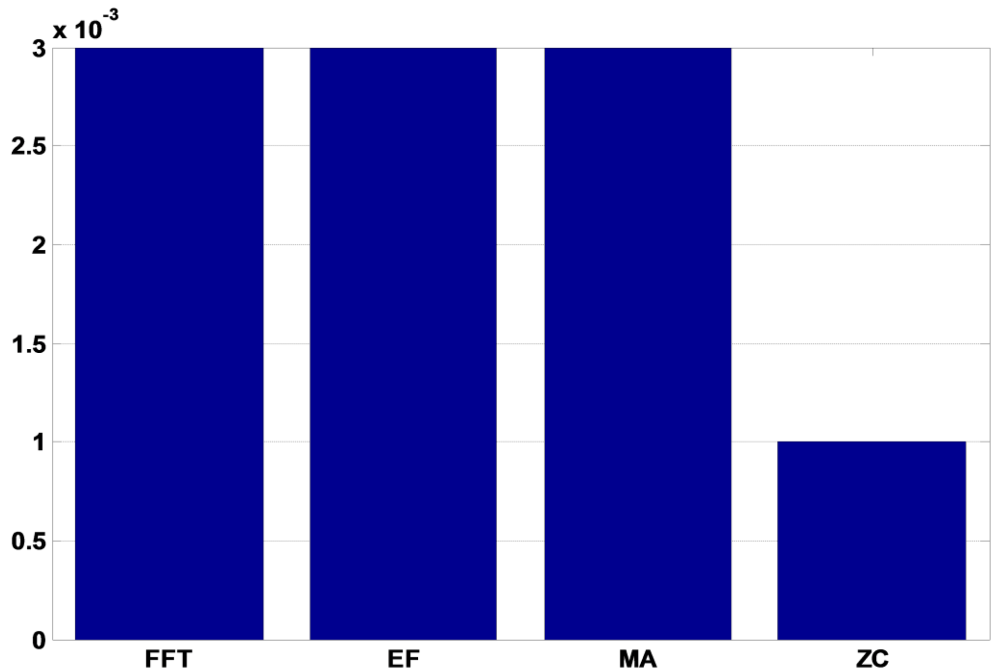

(b)

Figure 5.13 (a) The mean absolute error (b) the absolute error variance of the human breathing rate estimate by using the DFT, EF, MA, and ZC methods in an office environment.

The mean absolute error using the zero-crossing method was reduced by 16.21% compared with the moving average filter method. The maximum error in the estimated breathing rate using the zero-crossing method was 41.33% of the real breathing rate while the maximum error after applying the moving average window to the FFT of the output of the moving average filter method was 52% of the real breathing rate. The error in the human breathing rate estimation using the zero-crossing method was the least at different angels and postures. The results show that using the zero-crossing method combined with an adjustable IIR bandpass filter was suitable for the human breathing rate estimation. The method was not sensitive to the time widow size of the breathing signal.

5.3.4 Human Breathing Rate Estimation Behind Walls

In the previous section a method was proposed to estimate the human breathing rate in an anechoic chamber and in an office environment. The target detection and range-bin estimation algorithm proposed in Chapter 4 works in free space as well as behind different types of walls. In human breathing rate estimation of targets behind walls, the SVD combined with the skewness method was applied to estimate which range-bin contains the target. After that, the zero-crossing with the time interval between each breath constraint algorithm was applied to the signal in that range-bin for the purpose of estimating the breathing rate.

To study the performance of the proposed method in human breathing rate estimation behind walls, 18 measurements were collected from a human breathing with normal breathing at a breathing rate of 18 breaths/min. The target was standing, sitting, and lying down 1.5m behind a 20 cm thick gypsum wall with at different angles (0, 30, 60, 90, 135, 180 degrees) from the transmitter and receiver antenna plane. The pre-processing algorithm was applied and the proposed range-bin estimation based on SVD was applied along with the skewness method. Finally, the FFT, moving average, ellipse fitting, and zero-crossing methods were applied to the correlator output at the estimated range-bin. A comparison was made between the mean absolute errors of the estimated breathing rate using the four methods.

Figure 5.14 (a) and (b) represent the mean absolute error and the variance of the absolute error of the estimated breathing rate of a human breathing with a breathing rate of 18 breaths/min behind a 20 cm gypsum wall using the FFT, moving average, ellipse fitting, and zero-crossing methods. The mean absolute error using the zero-crossing method was reduced 28.57% compared with the moving average filter method after applying the three sliding windows. The maximum error in the estimated breathing rate using the zero-crossing method was 41.33% of the real breathing rate while the maximum error after applying the moving average filter method was 52.67% of the real breathing rate. The error in the human breathing rate estimation using the zero-crossing method was the least at different angels and postures. It can be concluded that the zero-crossing method with physiological boundaries can be used to estimate the human breathing rate in free space and behind walls with minimum error in the estimate rate.

5.3.5 Two Targets Human Breathing Rate Estimation

In Section 4.6.2, a two target detection algorithm was proposed. If the range-bins of the two targets can be estimated, the breathing rate of the two targets can be estimated by applying the zero-crossing breathing rate estimation method to the received signals in these range-bins (see Section 5.3.2).

(a)

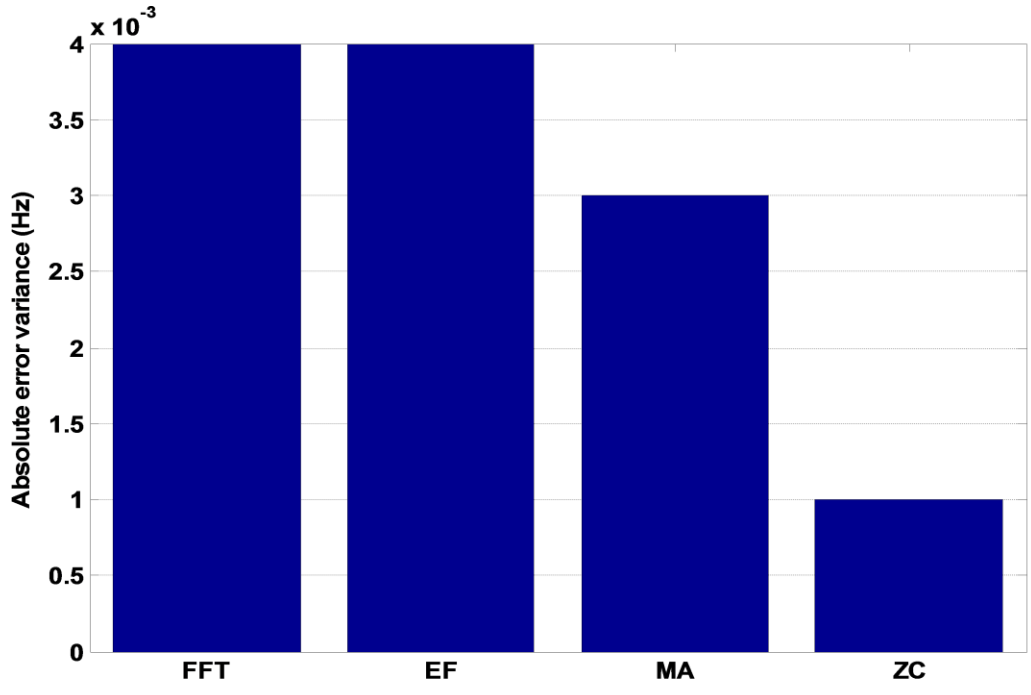

(b)

Figure 5.14 (a) The mean absolute error (b) the variance of the absolute error of the human breathing rate estimate by using the DFT, MA, EF, and ZC methods behind a 20 cm gypsum wall.

Figure 4.21 shows two targets breathing with normal breathing and sitting 2.5 m and 3.5 m from the radar in an anechoic chamber. The targets were wearing a breathing belt based on a piezo-electric sensor produced by CleveMed ™, Cleveland, USA [*116*] to measure the real breathing rate. The real breathing rates were 0.3 Hz and 0.4 Hz for the first and the second target, respectively. The targets' range-bins were estimated at 2.5 m and 3.6 m. Figure 5.15 (a) and (b) are the normalized correlator output at the first and the second target's range-bin, respectively. The estimated breathing rate for the first target was 0.29 Hz with an error equal to 3.3% of the real breathing rate and the estimated breathing rate for the second target was 0.42 Hz with an error equal to 5% of the real breathing rate.

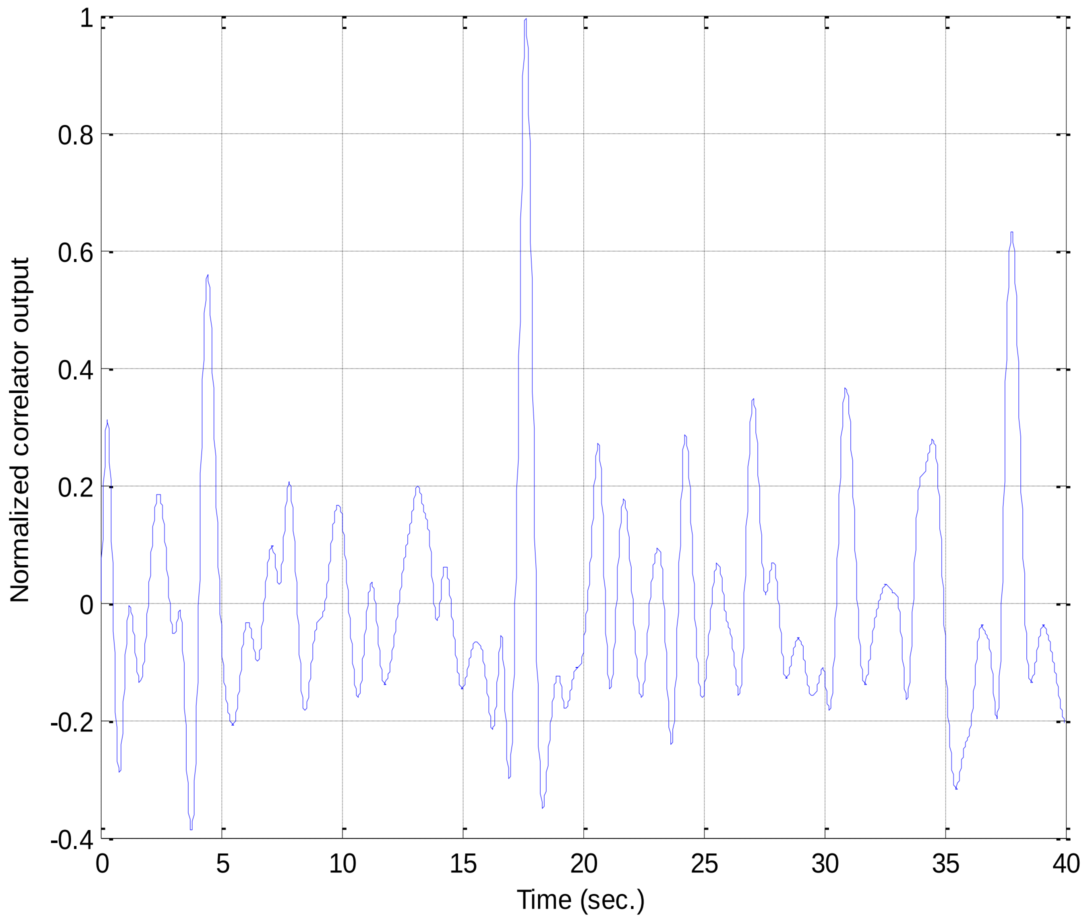

(a)

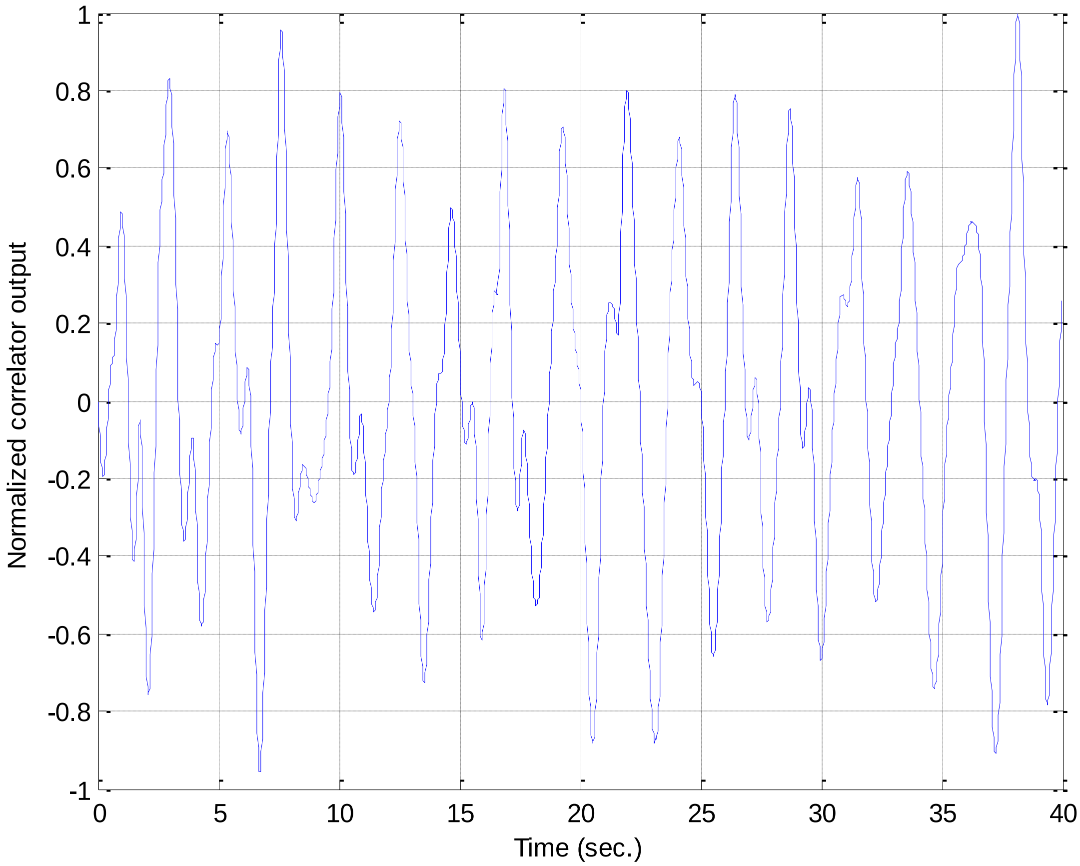

(b)

Figure 5.15 (a) The normalized correlator output at 2.5 m (b) The normalized correlator output at 3.6 m.

5.4 Discussion

In Chapter five, methods and algorithms were developed to estimate the human breathing in free space, office environment, and behind walls using UWB radars. The main source of error in human breathing estimation is the large magnitude of the second harmonic. Although any movement of the human body can be a source of error in human breathing estimation algorithms, this thesis focused on the second harmonic as a source of error. In this section, a summary is given of the observations, mathematical model, the proposed methods, and the comparison between the proposed methods and the state-of-the-art.

Important Observations Obtained Experimentally:
It was observed that the contribution of the abdominal movement resulted in multiple harmonics of the breathing signal. It was found that the major source of errors in human breathing detection algorithms was due to the second harmonic having higher magnitude than the first one.

Modeling:
The model of breathing signal reflected from a human and received in PN-UWB radar was updated so that it included contributions from the abdomen.

Proposed methods

- **Improving the State-of-the-art Algorithms**

To improve the state-of-the-art algorithms, it was necessary to address the problem of the magnitude of the second harmonic being higher than the magnitude of the first one in some scenarios. Three sliding windows were applied at the potential human breathing fundamental frequency and its second and third harmonics. This method guaranteed that the magnitude of the fundamental breathing frequency would be higher than the magnitude of its harmonics. It was found that the rectangular window outperforms Gaussian, Hann, and Hamming windows. Also, it was found that a window with length equal to 1% of the real breathing rate is suitable for this method.

- **Human Breathing Rate Estimation Based on Zero-crossing**

In this method, the zero-crossing was applied to the reflected signal from a human breathing and the time instants of the zero-crossings were estimated. The time interval constraint between each breath was applied by removing the intervals that exceeded the separation interval limits. The breathing rate f_{ZC} was estimated from the mean value of the time between the breath pulses.

The mean and the standard division of the PTPs was used to readjust the upper and lower cutoff frequencies of a Butterworth IIR BPF. The DFT of the output for the filter was computed and an estimation of the human breathing frequency f_{FFT} was made. If the difference between f_{ZC} and f_{FFT} was higher than 0.05 Hz, the output of the filter was processed by the algorithm again until the difference between f_{ZC} and f_{FFT} becomes smaller than 0.05 Hz. By using this method, it was possible to remove the contribution of higher breathing harmonics and the breathing rate was estimated accurately.

Comparisons Between the Proposed Methods and the State-of-the-art
A comparison was made between the FFT, moving average, and ellipse fitting methods before and after using the three sliding windows method, as described in Section 5.3.1.5. The FFT, moving average, and ellipse fitting methods detected the second breathing frequency harmonic as the dominant peak of the spectrum instead of detecting the peak of the first harmonic, in some scenarios. By using our new method, the first harmonic of the breathing signal was detected in all measurements.
Next, a comparison was made between FFT, moving average, and ellipse fitting methods, after using the three sliding windows and the proposed zero-crossing method with the time interval constraints between breaths. The zero-crossing method with this constraint outperformed the other methods in the anechoic chamber, the office environments, and also behind the wall. The mean absolute error using the zero-crossing method was reduced by 34.04%, 16.21%, and 28.57% compared with the moving average filter method after applying the three sliding windows in the anechoic chamber, in the office environments, and behind the wall, respectively.

Comparison between the DFT and zero-crossing algorithms in computational complexity

A comparison between the computational complexity of the FFT and zero-crossing methods was performed by measuring the mean value of the running-time for both methods. The programs were implemented in Matlab and were executed on a laptop having a 2.26 GHz Intel core i3-350M processor and Windows 7 operating system. The two methods were run 100 times to estimate the breathing rate, and the mean values of the running-time were computed. The mean values of the execution time for the FFT and zero-crossing were 0.57 seconds and 0.06 seconds, respectively. The zero-crossing method is less computationally intensive for this particular implementation.

Limitations on Improving the State-of-the-art Algorithms

The error in the estimated breathing rate increases when the spectrum of the breathing signal contains high magnitude componets at low frequencies (~0.1Hz or less). Pre-processing is very important to remove these low frequencies.

Limitations on Human Breathing Rate Estimation Based on Zero-crossing

The zero-crossing method combined with an adjustable bandpass filter based on the breathing pulse-to-pulse interval can be used to eliminate the effect of the human body large-scale displacements. Also, it can be used to eliminate the effect of the dominant second harmonic. However, when the received signal is composed of two harmonics, one at the fundamental breathing rate and the other at the second harmonic, shifted in phase by $\pi/2$ from each other, the signal will cross the positive zero-crossing level at time instants equal to multiples of the half of the real breathing pulse interval. The estimated breathing rate will be twice of the fundamental breathing rate. However, the estimated breathing rate at the negative zero-crossing level will be equal to the fundamental breathing rate. In this case, the minimum estimated breathing rate using the positive and the negative threshold level can be selected.

Chapter 6

Posture Estimation

6.1 Introduction

Human posture estimation is significant in security applications and military operations, rescue operations, and home-care applications. In security applications and military operations, it is important to estimate the number of targets and their postures before attacking the suspicious places. Estimating the posture of these targets will help in determining the best scenario to break in.

It was observed that the contribution of the abdominal displacements while breathing, relative to the chest displacements, is differed at various postures. This feature can be used to distinguish between fallen people on the ground/floor and sitting or standing people in free space and behind a wall.

In rescue operations, estimating the human posture can help in planning a rescue triage. Humans trapped under debris and lying down may need to be rescued before those who are standing or sitting. The posture of people trapped in a collapsed building disaster may be used as a parameter in the rescue triage plan.

In Chapter five, a mathematical model of the received human breathing signal in PN-UWB radar was proposed. The spectrum of the correlator output was observed. It was found that the magnitude of the breathing frequency harmonics changed when the displacements of the chest and the abdomen changed. The displacements of the chest and the abdomen changed when the human changed his/her posture. This means that the ratio between the different breathing harmonics will carry the information of the human posture. Unlike earlier published works, both chest and abdominal movements were considered for modeling the radar return signal along with the contributions of fundamental breathing frequency and its harmonics.

In this Chapter, the analyses of recorded reflected signals from three subjects in different postures and at different ranges from the radar indicated that ratios of the amplitudes for the harmonics contained information about both posture and posture changes. Attention was directed towards the relationship between the ratios of different breathing frequency harmonics magnitude for a breathing signal reflected from a human and received in PN-UWB radar. The posture of this human was also studied.

6.2 Human Breathing Displacements

The basic idea of UWB sensing is to obtain estimates of the vital signs through signal processing for the small motions related to the organs that are responsible for producing those signs. These small motions manifest as micro-Doppler in the radar returns, which is further processed to obtain the estimates.

In the literature, the signal reflected from the human breathing displacements is assumed to be a sine wave [*93,94*]. However, in [*95*], the human breathing signal was modeled as a sine wave or a number of frequency harmonics added together. In [*48*], the observation of the breathing rate for a number of volunteers indicated that the human breathing displacements were observed from the chest and the abdominal displacements. Also, it was observed that the abdomen displacements were larger than the chest displacements [*48*].

Attention was also directed towards the displacements of the chest and the abdomen of a human breathing with normal breathing. A breathing belt was utilized based on a piezo-electric sensor produced by CleveMed ™, Cleveland, USA [*116*]. The chest and the abdomen breathing signals recorded by the breathing belt are shown in Fig. 5.2 (a) and (b), respectively. The FFT of these signals is shown in Fig. 5.3 (a) and (b). Multiple frequency harmonics of the breathing frequency have been observed in the FFT of the abdominal breathing signal. This means that the displacement of the chest and the abdomen are not sinusoidal. The mathematical model presented in [*95*] has been adapted along with the two cylinder model presented in [*96*]. Observations on the displacements of the chest and the abdomen and a new mathematical model of the breathing signal received in PN-UWB radar are presented in Section 5.2. In the following section, the relationship between the human posture and the human breathing frequency harmonics ratios are observed. The objective was to find a feature that could be used in human posture classification.

6.3 Relationship between Human Posture and Breathing Frequency Harmonic Ratios

The FFT of the correlator output is presented in Eq. 5.13

$$Y(f,\tau_0) = A \sum_{k,l,m=-\infty}^{+\infty} C_{klm}\delta(f-(k+l)f_b - m(2\,f_b))$$

where

$$C_{klm} = \int_{-\infty}^{+\infty} P(\,v)J_k(\beta_{\tau_1}v)J_l(\beta_{\mu_1}v)J_m(\beta_{\mu_2}v)dv \approx \;\Delta f.J_k(\beta_{\tau_1}f_c)J_l(\beta_{\mu_1}f_c)J_m(\beta_{\mu_2}f_c)P(f_c)$$

If the phase shift between the displacements of the abdomen and the chest is $\emptyset$ and if it is assumed that the chest movement is sinusoidal and the abdomen movement is composed of fundamental frequency and the second harmonic, the correlator output at a target range-bin becomes:

$$y(t,\tau) = Ap(\tau - \tau_0 - \tau_1 sin(2\pi f_b t) - \mu_2\, sin(2\pi f_b t + \emptyset_1) - \mu_2\, sin(4\pi f_b t + \emptyset_2)) \qquad (6.1)$$

where $\emptyset_1$ and $\emptyset_2$ are the phase shift between the abdominal displacements first and second harmonic, and the chest displacement first harmonic. Equation 5.9 becomes:

$$Y(f,v) = AP(v)e^{-j2\pi v\tau_0}\int_{-\infty}^{+\infty}(S_1S_2S_3S_4S_5)e^{-j2\pi ft}dt \qquad (6.2)$$

where $P(v)$ is the Fourier transform in the fast time of the correlated pulse and:

$$S_1 = \sum_{k=-\infty}^{+\infty} J_k(\beta_{\tau_1}\,v)e^{-j2\pi kf_bt} \qquad (6.3)$$

$$S_2 = \sum_{l=-\infty}^{+\infty} J_l(\beta_{\mu_1}\,v\;cos(\emptyset_1))e^{-j2\pi lf_bt} \qquad (6.4)$$

$$S_3 = \sum_{n=-\infty}^{+\infty} J_n(\beta_{\mu_1}\,v\;sin(\emptyset_1))e^{-j2\pi nf_bt}e^{-jn\pi/2} \qquad (6.5)$$

$$S_4 = \sum_{m=-\infty}^{+\infty} J_m(\beta_{\mu_2}\, \nu\, cos(\emptyset_2)) e^{-j2\pi m(2f_b)t} \tag{6.6}$$

$$S_5 = \sum_{q=-\infty}^{+\infty} J_q(\beta_{\mu_2}\, \nu\, sin(\emptyset_2)) e^{-j2\pi q(2f_b)t} e^{-jq\pi/2} \tag{6.7}$$

where $\beta_x = 2\pi x$ and $\sum_{p=-\infty}^{+\infty} J_p(z) e^{-j2\pi p f_0 t} = e^{-jz sin(2\pi f_0 t)}$ is the series of Bessel functions.

The value of C_{klm} in Eq. 5.13 is modified to be

$$C_{klmnq} \approx \Delta f . J_k(\beta_{\tau_1} f_c) J_n(\beta_{\mu_1} sin(\emptyset_1)\, f_c) J_l(\beta_{\mu_1} cos(\emptyset_1)\, f_c) J_q(\beta_{\mu_2} sin(\emptyset_2)\, f_c) J_m(\beta_{\mu_2} cos(\emptyset_2)\, f_c) P(f_c) \tag{6.8}$$

If the phase shift between the chest and the abdomen displacements $\emptyset_1, \emptyset_2 = 0$, Eq. 6.8 reduces to Eq. 5.14.

Equation 6.8 indicates that the slow time spectrum is discrete and has spectral lines at frequencies of the harmonics for the breathing frequency. These harmonics are intermodulation products of the chest and abdominal movements. The amplitude of each intermodulation product at a given frequency $f = (k + l + n)f_b + 2(m + q)f_b$ is determined by the coefficient C_{klmnq}. It may be noted that the modulation index β_x in Eq. 6.8 changes with the posture due to the fact that the abdomen and chest displacements are different for different postures. As a consequence, the values of the coefficients C_{klmnq} change with posture. This information can be effectively used to identify the posture of the target or at the minimum provide an indication of possible posture of the target. The coefficient at the breathing frequency is given by:

$$C_f = C_{10000} + C_{01000} + C_{001000} \tag{6.9}$$

while the coefficient at the second harmonic is given by:

$$C_{2f} = C_{00001} + C_{00010} + C_{20000} + C_{02000} + C_{00200} + C_{11000} + C_{01100} + C_{10100} \tag{6.10}$$

, and the coefficient at the third harmonics is given by:

$$C_{3f} = C_{30000} + C_{03000} + C_{00300} + C_{11100} + C_{10010} + C_{10001} + C_{01010} + C_{01001} + C_{00101} + \\ + C_{00110} + C_{21000} + C_{20100} + C_{12000} + C_{10200} + C_{01200} + C_{02100} \tag{6.11}$$

The ratio of the harmonics, $R_{21} = \frac{C_{2f}}{C_f}$ and $R_{31} = \frac{C_{3f}}{C_f}$ will vary with posture and by estimating these ratios, it may be possible to identify the posture of the target.

Table 6.1 illustrates the ratios R_{21} and R_{31} at three different abdomen displacements. We assumed that the displacements of center point for the chest in front of the radar are 0.2 cm [*6*] and the displacements of the abdomen are four times the displacements of the chest [*48*]. The second harmonic magnitude of the breathing frequency is equal to 20% of the first harmonic as it was observed in Fig. 5.3 (b). The ratios R_{21}, and R_{31} increase when the displacements of the abdomen increase. The displacements of the abdomen change in the different human postures. As a result, the ratios R_{21} and R_{31} will change when a human changes his/her posture.

Table 6.1 R_{21} and R_{31} ratios at different abdomen displacements.

Index	**Chest displacements (cm)**	**Abdomen displacements (cm)**	$\frac{C_f}{\Delta f \times P(f_c)}$	$\frac{C_{2f}}{\Delta f \times P(f_c)}$	$\frac{C_{3f}}{\Delta f \times P(f_c)}$	R_{21}	R_{31}
1	0.2	0.2	0.342	0.096	0.020	0.280	0.058
2	0.2	0.8	0.615	0.385	0.188	0.626	0.306
3	0.2	1.6	0.306	0.430	0.431	1.41	1.41

Figure 6.1 presents R_{21} and R_{31} for a constant chest displacement (0.2 cm) and abdominal displacements from 0.2 to 1.6 cm. The ratios increase when the displacements of the abdomen increase. In some scenarios, the second breathing frequency harmonic may have a magnitude higher than the first breathing frequency harmonic.

Figure 6.2 is R_{21} and R_{31} for the spectrum of a simulated breathing signal that is reflected from a human breathing with chest displacements equal to 0.2 cm. The abdominal displacements were assumed to be equal to four times the chest displacements at different phase shifts $\emptyset$. The maximum ratios occur when $\emptyset$ is equal to $\pi/4$ and the minimum ratios occur when $\emptyset$ is equal to zero or $\pi/2$.

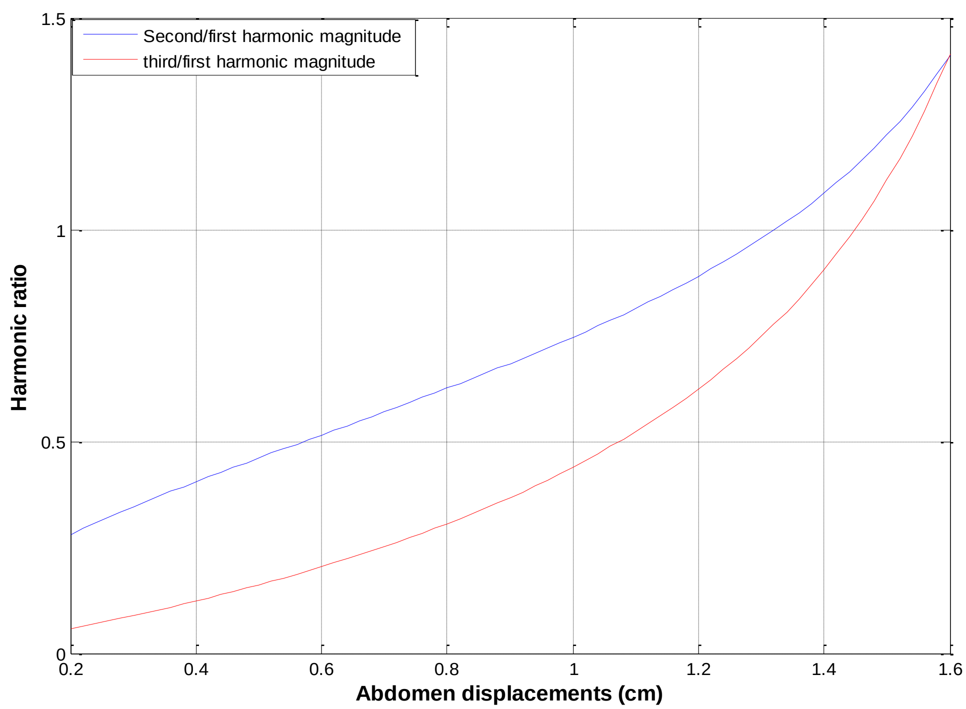

Figure 6.1 Harmonic ratios at different abdomen displacements.

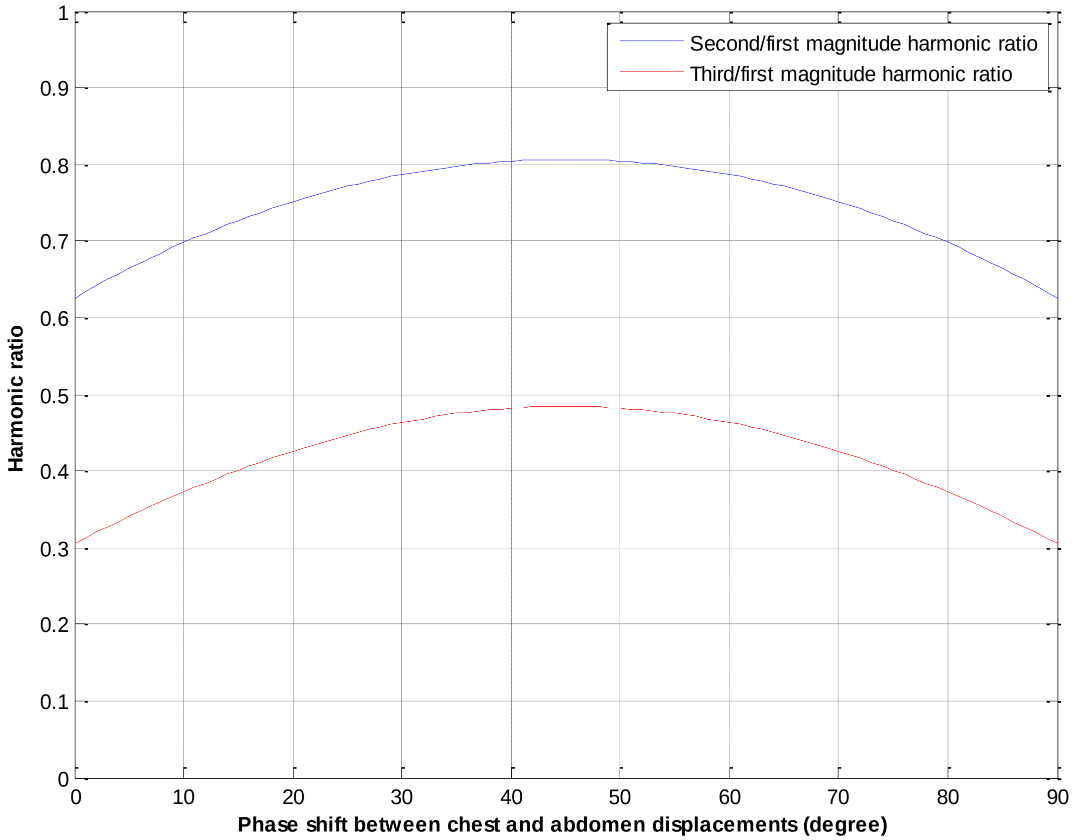

Figure 6.2 Harmonic ratios at different ∅ and the chest displacement of 0.2 cm and the abdominal displacements of 0.8 cm.

6.4 Methodology

Figure 6.3 shows this research's proposed method for computing the breathing frequency harmonic magnitude ratios. The data matrix which is collected as shown in Fig. 2.2 was applied to the data-preprocessing algorithm (Section 4.3). Then the proposed SVD detection algorithm (see Fig. 4.17) was applied. The output of the SVD detection algorithm was a decision of detection and the estimated target range-bin. An assumption was made that a target has been detected at a range-bin b computed at a fast time τ_b. From Eq. 6.1, the correlator output at the fast time τ_b will be:

$$y(t,\tau_b) = Ap(\tau_b - \tau_0 - \tau_1 sin(2\pi f_b t) - \mu_2\, sin(2\pi f_b t + \emptyset_1) - \mu_2\, sin(4\pi f_b t + \emptyset_2)) \qquad (6.12)$$

A Hann window was applied to the signal $y(t,\tau_b)$ with length equal to 40sec for the purpose of minimize the edge effects in the FFT spectrum of the signal. The output is:

$$y_h(t,\tau_b) = y(t,\tau_b) \times w(t) \qquad (6.13)$$

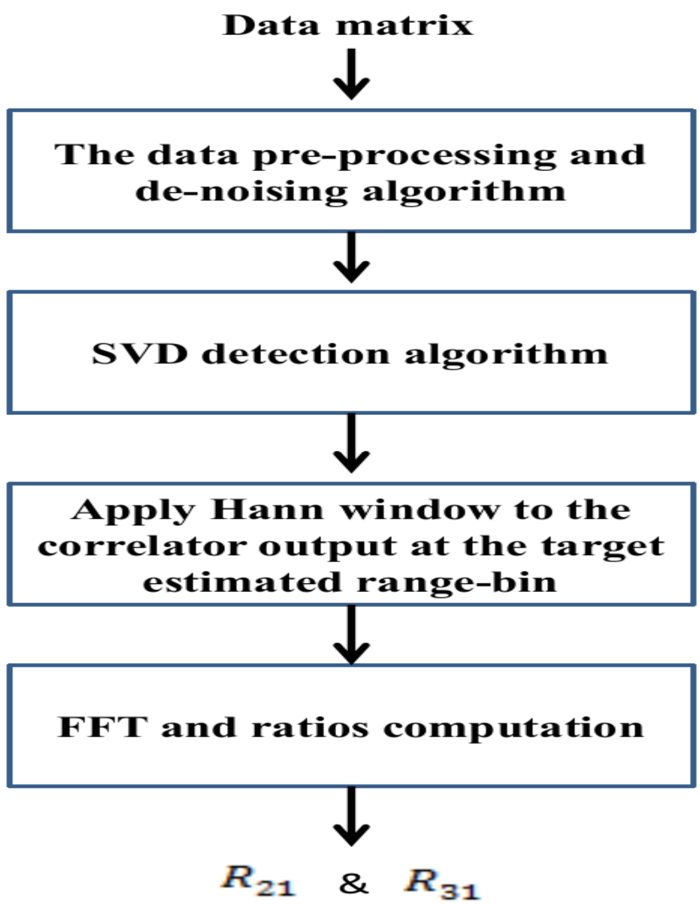

Figure 6.3 Harmonic ratios computation method.

where, $w(t)$ is Hann window with length equal to the correlator output signal length in the slow time direction. The sampled correlator output is obtained in discrete instants in slow time $t = kT_s$

$$y_h(t, \tau_b) = y(t, \tau_b) \times w(t), \qquad t = 0,1, \dots, (K-1)T_s \tag{6.14}$$

and

$$w(t) = 0.5\left(1 - cos\left(2\pi \frac{kT_s}{K}\right)\right), \qquad 0 \leq k \leq K-1 \tag{6.15}$$

where, K is the number of samples in the slow time dimension. Finally, FFT was applied to $y_h(t, \tau_b)$. From Eq. 5.13 and Eq. 6.8, FFT of $y_h(kT_s, \tau_b)$ will be:

$$Y_h(f, \tau_b) = W(f) * A \sum_{k,l,m,n,q=-\infty}^{+\infty} C_{klmnq} \delta(f - (k+l+n)f_b - 2(m+q)\, f_b) \tag{6.16}$$

where $W(f)$ is the FFT of $w(t)$ and $(*)$ is the convolution operation. $Y_h(f, \tau_b)$ will have spectral lines at frequencies $f = (k+l+n)f_b + 2(m+q)f_b$. A study will be conducted of the ratios between the magnitudes of these spectral lines and its relation with human posture change.

6.5 Breathing Frequency Harmonic Ratios in Different Environments

In this section, a study was conducted of the ratios between the second and the third to the first breathing frequency harmonics magnitude in three different environments: the anechoic chamber, an office environment, and behind a gypsum wall. The subject was asked to take a breath when he heard a tone generated from a software program and repeated every 3.33 seconds. The subject was standing, sitting, and lying down 1.5 m from the radar at angles 0, 30, 60, 90, 135, 180 degrees from the transmitter and receiver antenna plane. Six measurements were recorded at every posture and a total 18 measurements were recorded in each environment. The measurements were collected in the anechoic chamber, and in an office environment in free space and behind a 20 cm thickness gypsum wall at the University of Ottawa, Ottawa, Canada. Figure 6.5 shows the model of a human breathing while standing, sitting, and lying down and facing the radar with 0, 30, 60, 90, 135, and 180 degrees from the transmitter and receiver antenna plane.

6.5.1 Human Breathing Frequency Harmonic Ratios in an Anechoic Chamber

The breathing frequency harmonics magnitude C_f, C_{2f}, and C_{3f} are presented in Eq. 6.9, 6.10, and 6.11. The ratio of the harmonics, $R_{21} = \frac{C_{2f}}{C_f}$ and $R_{31} = \frac{C_{3f}}{C_f}$ will vary with posture and by estimating these ratios, it may be possible to identify the posture of the target.

Eighteen measurements were collected from a human standing, sitting, and lying down at different angles from the transmitter and the receiver plane as described in Fig. 6.4. The harmonic magnitudes were computed in each measurement for three scenarios: covering the abdomen with Radio Frequency (RF) absorber, covering the chest with RF absorber, and not covering the chest or the abdomen with the RF absorber. The reflectivity of the used RF absorber at the PN-UWB radar center frequency was recorded less than -22 dB [*117*]. Figure 6.5 represents a human covering his chest by an RF absorber. Table 6.2 presents the first, second, and third breathing harmonic magnitudes C_f, C_{2f}, and C_{3f} for the three scenarios in each measurement. S_c is referring to covering the abdomen with Radio Frequency (RF) absorber scenario, S_a refers to covering the chest with RF absorber scenario, and S_b refers to measurements when not covering the chest or the abdomen with the RF absorber scenario.

We computed the magnitude of the spectrum at the breathing frequency harmonics C_f**,** C_{2f} , C_{3f}, and the ratios R_{21} and R_{31} in each measurement. The ratios R_{21} and R_{31} when the chest and the abdomen were not covered by the absorber are in the bold faced numbers. We add the magnitude of the spectrum of first harmonic C_f of the two uncovered parts and test if they are approximately equal to the magnitude value when there is no absorber. 31 measurements out of 54 measurements (around 57%) were showing that the magnitude when there is no absorber is approximately equal to the magnitude when covering the chest plus the magnitude when covering the abdomen. We found that the magnitude of C_f in 40 measurements (74%) is higher than or equal to the magnitudes of C_{2f} and C_{3f}.

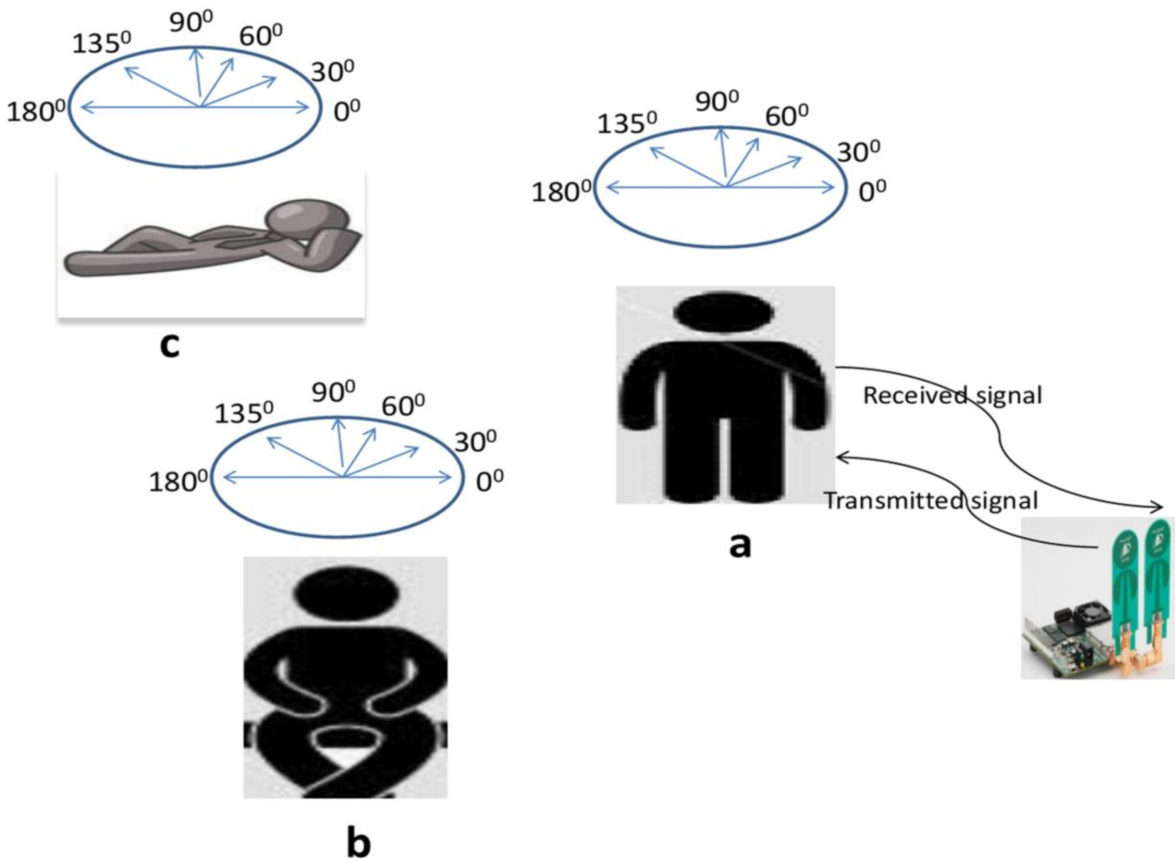

Figure 6.4 Measurement model of a human (a) standing (b) sitting (c) lying down and facing the radar at 6 different angles.

Figure 6.5 A human covering his chest with an RF absorber.

Table 6.2 Breathing frequency harmonics magnitude at different postures and angles in an anechoic chamber.

Angle	Posture	Scenario	C_f	C_{2f}	C_{3f}	R_{21}	R_{31}
0°	Standing	S_b	$1.2x10^6$	$8.86x10^5$	$2.80x10^5$	**0.74**	**0.23**
		S_c	$9.5x10^5$	$3.6x10^5$	$2.8x10^5$	0.38	0.29
		S_a	$1.2\ x10^6$	$3.1x10^5$	$2.6x10^5$	0.26	0.22
	Sitting	S_b	$1.66x10^6$	$2.00x10^6$	$0.6x10^5$	**1.20**	**0.04**
		S_c	$1.40\ x10^5$	$9.2\ x10^4$	$2.14\ x10^4$	0.66	0.15
		S_a	$9.79x10^5$	$3.6\ x10^5$	$2\ x10^5$	0.37	0.2
	lying	S_b	$15.00x10^4$	$5.00x10^4$	$4.00x10^3$	**0.33**	**0.03**
		S_c	$6.09x10^4$	$1.14\ x10^4$	$5.82\ x10^3$	0.19	0.09
		S_a	$8.32\ x10^4$	$2.43\ x10^4$	$8.56x10^3$	0.29	0.1
30°	Standing	S_b	$8.53\ x10^5$	$5.65\ x10^5$	$3.2\ x10^5$	**0.67**	**0.38**
		S_c	$3.50\ x10^5$	$1.25\ x10^5$	$0.4\ x10^5$	0.36	0.11
		S_a	$7.00x10^5$	$2.65\ x10^5$	$1.35\ x10^5$	0.38	0.19
	Sitting	S_b	$12.30\ x10^5$	$14.10\ x10^5$	$1.7\ x10^5$	**1.15**	**0.14**
		S_c	$6.20\ x10^5$	$8.20\ x10^4$	$1.65\ x10^5$	0.13	0.26
		S_a	$6.75\ x10^5$	$3.00\ x10^5$	$8.63\ x10^4$	0.44	0.13
	lying	S_b	$1.86\ x10^5$	$5.00x10^4$	$2.70x10^4$	**0.27**	**0.14**
		S_c	$7.00x10^4$	$1.00x10^4$	$1.00x10^4$	0.14	0.14
		S_a	$9.00x10^4$	$5.50x10^4$	$1.00x10^4$	0.61	0.11
60°	Standing	S_b	$2.30\ x10^5$	$1.80\ x10^5$	$0.60x10^5$	**0.78**	**0.26**
		S_c	$1.90\ x10^5$	$2.70\ x10^4$	$7.00\ x10^3$	0.14	0.04
		S_a	$2.5\ x10^5$	$1.34\ x10^5$	$6.40\ x10^3$	0.54	0.03
	Sitting	S_b	$1.65\ x10^5$	$2.34\ x10^5$	$1.10\ x10^5$	**1.41**	**0.66**
		S_c	$12.00\ x10^4$	$5.00\ x10^4$	$2.00\ x10^4$	0.42	0.16
		S_a	$2.21\ x10^5$	$0.50\ x10^5$	$0.50\ x10^5$	0.23	0.23
	lying	S_b	$1.37\ x10^5$	$4.70x10^4$	$2.30x10^4$	**0.34**	**0.17**
		S_c	$1.01\ x10^5$	$3.16x10^4$	9000	0.31	0.09
		S_a	$7.9\ x10^4$	$1.47\ x10^4$	4200	0.19	0.05
90°	Standing	S_b	$5.64\ x10^5$	$4.02\ x10^5$	$1.85x10^5$	**0.74**	**0.32**
		S_c	$6.50\ x10^5$	$2.60\ x10^5$	$4x10^4$	0.4	0.06
		S_a	$6.25x10^5$	$2.32\ x10^5$	$7.5\ x10^4$	0.37	0.12
	Sitting	S_b	$1.42\ x10^6$	$1.45\ x10^6$	$1.00\ x10^6$	**1.02**	**0.70**
		S_c	$1.14\ x10^5$	$4.00\ x10^4$	$4.00x10^4$	0.35	0.35
		S_a	$1.38\ x10^6$	$3.33\ x10^5$	$1.70\ x10^5$	0.25	0.12
	lying	S_b	$2.14\ x10^5$	$4.34\ x10^4$	$6.40\ x10^3$	**0.20**	**0.03**
		S_c	$9.29\ x10^4$	$2.54\ x10^4$	$4.25\ x10^3$	0.27	0.05
		S_a	$9.93\ x10^4$	$1.00\ x10^4$	$7.60\ x10^3$	0.10	0.08
135°	Standing	S_b	$1.50x10^6$	$1.50x10^6$	$1.00x10^6$	**1.00**	**0.66**
		S_c	$12.00x10^5$	$3.46x10^5$	$1.60x10^5$	0.29	0.13
		S_a	$2.21\ x10^6$	$1.30x10^6$	$2.00x10^5$	0.59	0.09
	Sitting	S_b	$4.25x10^6$	$5.83x10^6$	$1.50x10^6$	**1.37**	**0.35**
		S_c	$8.20x10^6$	$4.00x10^6$	$2.00\ x10^6$	0.49	0.24
		S_a	$2.16x10^6$	$2.56\ x10^6$	$6.84\ x10^5$	1.19	0.32
	lying	S_b	$8.00x10^5$	$3.20x10^5$	$2.00x10^5$	**0.4**	**0.25**
		S_c	$8.00x10^5$	$2.54\ x10^5$	$1.00\ x10^5$	0.32	0.13
		S_a	$1.57x10^5$	$4.60\ x10^4$	$3.20\ x10^4$	0.29	0.20
180°	Standing	S_b	$1.43\ x10^6$	$8.80\ x10^5$	$2.00x10^5$	**0.62**	**0.14**
		S_c	$9.13\ x10^5$	$3.50x10^5$	$2.6\ x10^5$	0.38	0.28
		S_a	$8.90\ x10^5$	$4.70\ x10^5$	$1.91\ x10^5$	0.52	0.21
	Sitting	S_b	$3.67\ x10^5$	$3.46\ x10^4$	$0.95\ x10^5$	**0.94**	**0.26**
		S_c	$5.00\ x10^5$	$2.50\ x10^5$	$0.9x10^5$	0.50	0.18
		S_a	$7.00\ x10^5$	$4.4\ x10^5$	$2.00\ x10^5$	0.63	0.29
	lying	S_b	$8.7\ x10^4$	$2.26\ x10^4$	$5.45\ x10^3$	**0.26**	**0.06**
		S_c	$4.65\ x10^4$	$4.5\ x10^3$	$4.5\ x10^3$	0.1	0.10
		S_a	$3.25\ x10^4$	$1.07\ x10^4$	$3.74\ x10^3$	0.34	0.12

From Eq. 6.16, the spectrum of the received breathing rate will have intermodulation components at the frequencies $f = (k + l + n)f_b + 2(m + q)f_b$. Figure 6.1 show that when the abdomen displacements decrease, the ratio R_{21} will be decreased. When we covered the chest or the abdomen we expected the value of R_{21} to be decreased. 49 measurements (89%) show that the ratios of R_{21} when we cover the chest or the abdomen were less than without covering any of them. From Eq. 6.9, 6.10, and 6.11, it is obvious that when the chest or the abdomen is covered by the absorber, the ratio R_{21} is expected to be lower than without covering any of them. In the 54 measurements, the ratio $R_{21}$when covering the chest or the abdomen was higher than without covering any of them only 3 times.

The subject was breathing with a breathing rate equal to 0.3 Hz. We applied FFT to the received signal in the estimated target range-bin in the slow time dimension to detect the human breathing frequency (0.3 Hz). The breathing movements have been detected when covering the chest or the abdomen by the RF absorber in all the 54 measurements. We learn from the previous measurements that the human abdomen moves while breathing and the reflected signal from a human breathing will compose of the reflected signals from the chest and the abdomen.

To compare between our mathematical model and the results in table 6.2, we measured the displacements of chest and the abdomen of the same subject using a piezo-electric breathing belt produced by CleveMed ™, Cleveland, USA [*116*]. We measured the displacements of the chest and the abdomen in three scenarios: lying down, standing, and sitting. Figure 6.6 (a), (b), and (c) represents the displacements of the chest and the abdomen for the same subject in the three scenarios, respectively. The displacements of the chest in the three scenarios were around 0.6 cm. The displacements of the abdomen were around 0.5 cm, 1 cm, and 1.2 cm in a lying down posture, standing posture, and sitting posture, respectively. The measurements showed that the displacements of the chest are almost the same in the three postures. However, the displacements of the abdomen changed when the human posture changed. The displacements of the abdomen in the sitting and standing postures were higher than the displacements of the abdomen in the lying down posture. The ratio between the displacements of the abdomen to the displacements of the chest was 0.83, 1.6, and 2 in lying down, standing, and sitting postures, respectively. Using Equations 6.9 and 6.10, the computed R_{21} ratios were 0.3, 0.78, and 1.1 in the lying down, standing, and sitting postures, respectively. Results in table 6.2 in the bold faced numbers are very close to the values that were computed using our model in different human postures.

Figure 6.7 shows the ratios R_{21} in table 6.2 without covering the chest or the abdomen with the absorber. The ratios R_{21} are illustrated with using the stars colors red, blue, and black in the lying down, standing, and sitting postures, respectively. The blue and red lines are this research's proposed mathematical model R_{21}, upper and lower limit, respectively, at fixed chest displacements equal to 0.6 cm and different abdominal displacements (0:1.5 cm), and a different phase shift, $\emptyset$,between the displacements of the abdomen and the chest (0:90^0). The measurements showed that the ratios R_{21} in the sitting and standing postures were higher than the ratios in the lying down postures. The ratios changed when the posture changed because the abdominal displacement changed. The measurements fit with this research's mathematical model.

The results showed that the chest and the abdomen of a human move while breathing and the displacements of the abdomen cannot be ignored. The state-of-the-art assumed that the human breathing movements came from one-part movement without specifying if it is from the chest or the abdomen [*31*,*34*,*95*]. The results in the table show that the human breathing movements come from two-part movements; the chest and the abdomen.

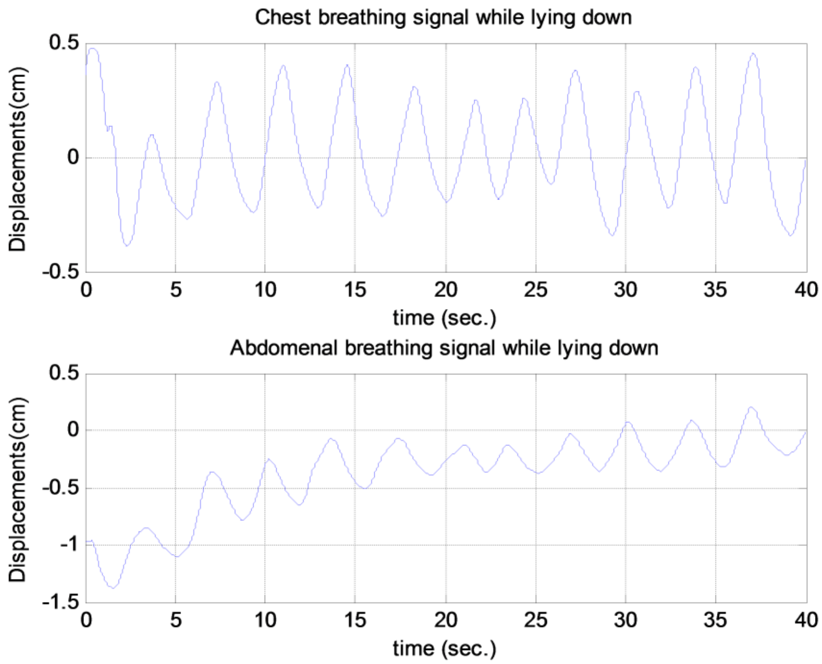

(a)

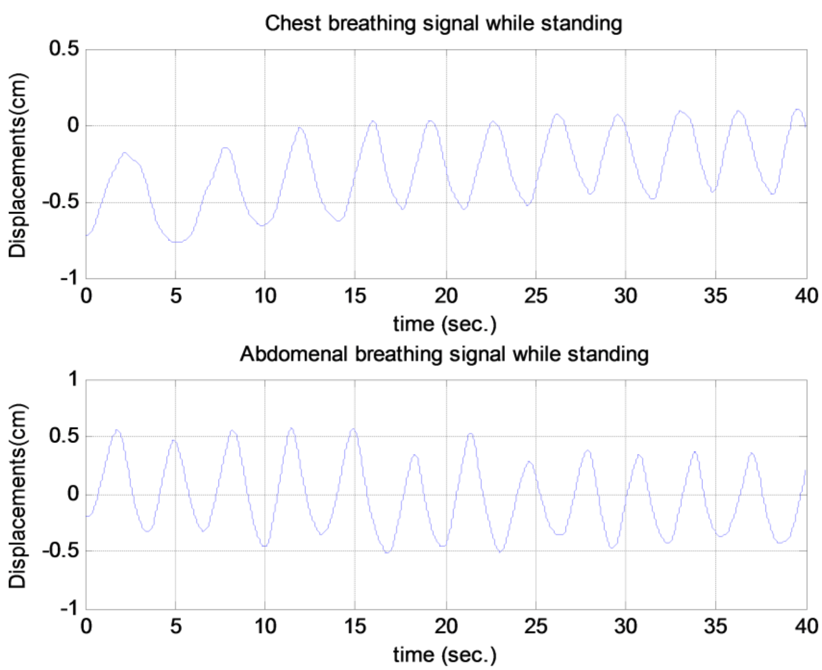

(b)

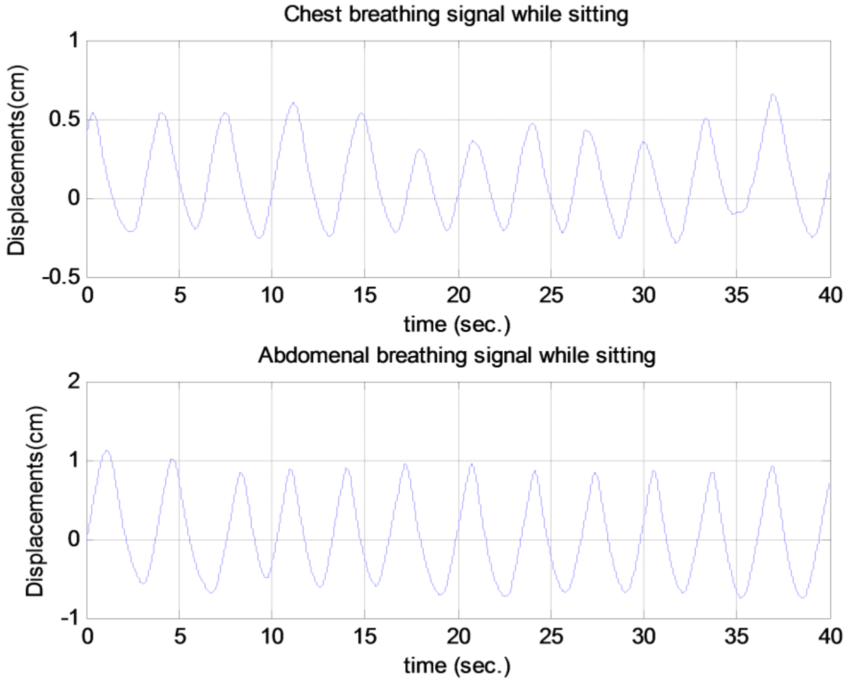

(c)
Figure 6.6 The displacements of the chest and the abdomen while (a) lying down (b) standing (c) sitting.

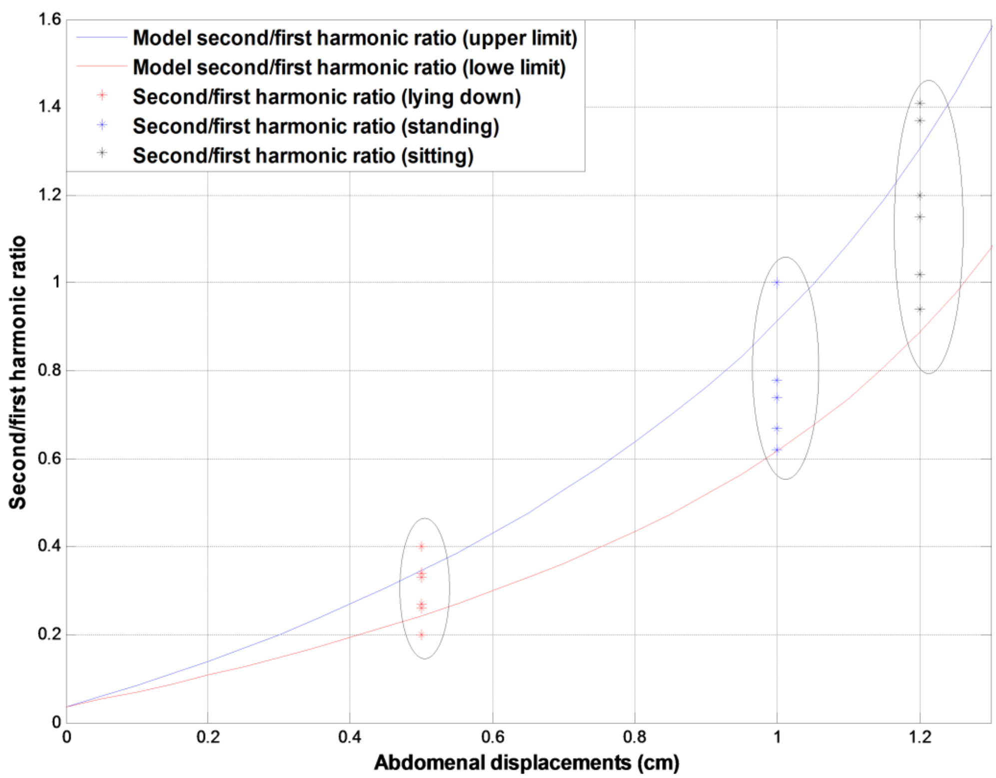

Figure 6.7 The second/first breathing harmonic ratio in three scenarios: lying down, standing, and sitting.

When studying the ratios R_{21} and R_{31} in different postures, it was observed that the ratios in standing and sitting postures are higher than the ratios in the lying down posture. The mean value of R_{21} at different angles is 0.76, 1.10, and 0.30 in standing, sitting, and lying down postures, respectively with a standard division equal to 0.13, 0.32, and 0.07, respectively.

The mean value of R_{31} at different angles is 0.33, 0.26, and 0.11 in standing, sitting, and lying down postures, respectively. It is clear that the ratios of different breathing frequency harmonics magnitude can be used as a feature in human posture estimation

In studying the ratio R_{21}in different body orientations, it was found that the orientation of the human body does not affect the ratios. The ratios R_{21} when a human is lying down are 0.33, 0.27, 0.34, 0.20, 0.40, and 0.26 at orientation angles 0^0, 30^0, 60^0, 90^0, 135^0, and 180^0, respectively. Also, the ratio $R_{31}$when the target is lying down is less than the ratio when he is sitting or standing in different orientations.

The ratio R_{21} when the target is sitting is larger than the ratio when he is standing in all body orientations. However, the ratios R_{21} when the target was sitting or standing overlapped in some measurements. Figure 6.8 (a) and (b) represents the DFT of the breathing signal of a subject breathing normally with a breathing rate equal to 0.3 Hz. The target was 1.5 m from the radar in an anechoic chamber, and sitting and lying down, respectively, with an orientation angle equal to zero. The ratio R_{21} in sitting posture ($R_{21} = 1.2$) is higher than that in lying down posture ($R_{21} = 0.33$).

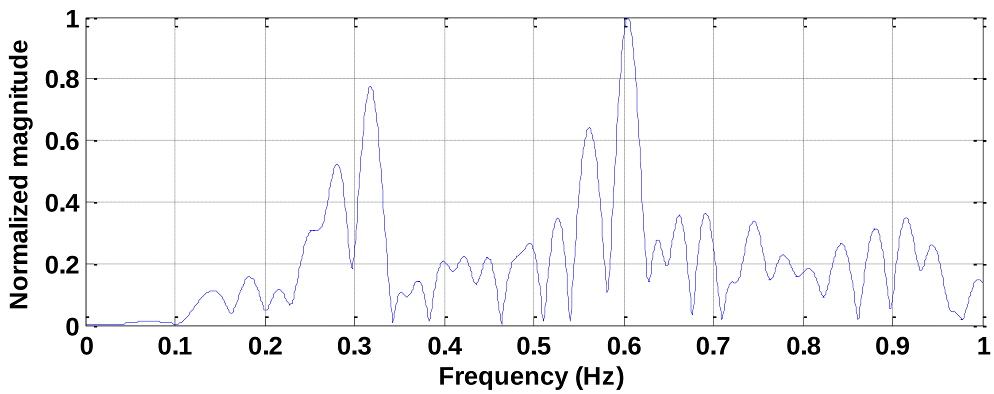

(a)

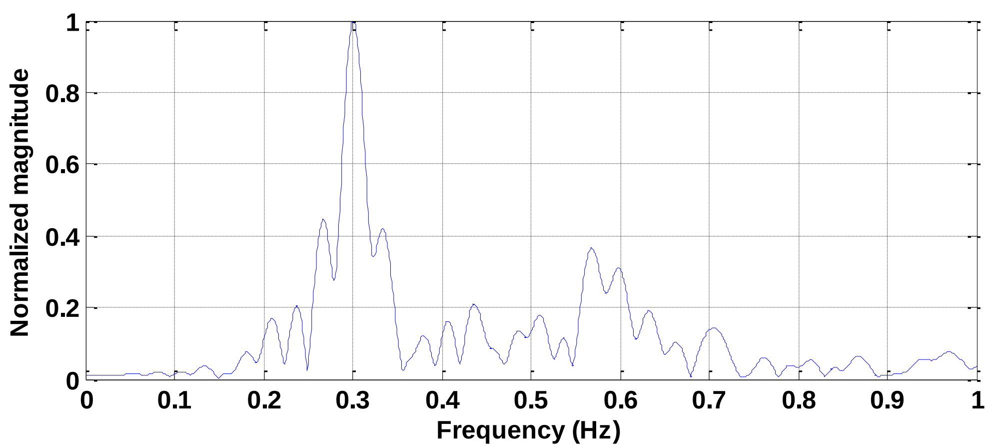

(b)

Figure 6.8 The DFT of the breathing signal in two scenarios: sitting and lying down.

6.5.2 Posture Estimation Results in Anechoic Chamber

Figure 6.9 is the Receiver Operating Characteristic (ROC) curve of the detection of a human in the dorsal position. The probability of detection is 100% with no false alarms when the threshold Thr is equal to 0.5. From the Figure, It is evident that a distinction can be made between a person lying on his/her back and a person sitting or standing. When the human body is lying down the ratios are small. This feature can be useful for detecting fallen people when monitoring them in homecare situation.

6.5.3 Posture Estimation Results in Office Environment

Eighteen measurements were collected in an office environment from a human standing, sitting and lying down at different angles from the transmitter and the receiver plane, as described in Fig. 6.4. Table 6.3 presents C_f, C_{2f} , C_{3f}, R_{21}, and R_{31}.

Studying the ratios R_{21} and R_{31} in different postures it was observed that the mean value of R_{21} at different angles was 0.82, 0.88, and 0.20 in standing, sitting, and lying down postures, respectively with a standard division equal to 0.23, 0.48, and 0.10, respectively. The mean value of R_{31} at different angles was 0.33, 0.36, and 0.06 in standing, sitting, and lying down postures, respectively. Results in table 6.2 show that when the target is standing or sitting the ratios R_{21} and R_{31} are higher than when he is lying down. Studying the ratio R_{21}in different body orientations, it was noted that the orientation of the human body does not affect the ratios.

When a human is lying down the ratios R_{21} are 0.21, 0.26, 0.35, 0.20, 0.08, and 0.09 at orientation angles 0^0, 30^0, 60^0, 90^0, 135^0, and 180^0, respectively. Also the ratio $R_{31}$was less than the ratio when he was sitting or standing. For all body orientations, the ratios when the human body was lying down are less than the ratios when he was standing or sitting.

Figure 6.10 represents the Receiver Operating Characteristic (ROC) curve of the detection for a human in the dorsal position in an office environment. The area under curve is 0.986. From the Figure, it is evident that a distinction can be made between a lying person on his/her back and a sitting or standing person. The ratios when the human body was lying down are small.

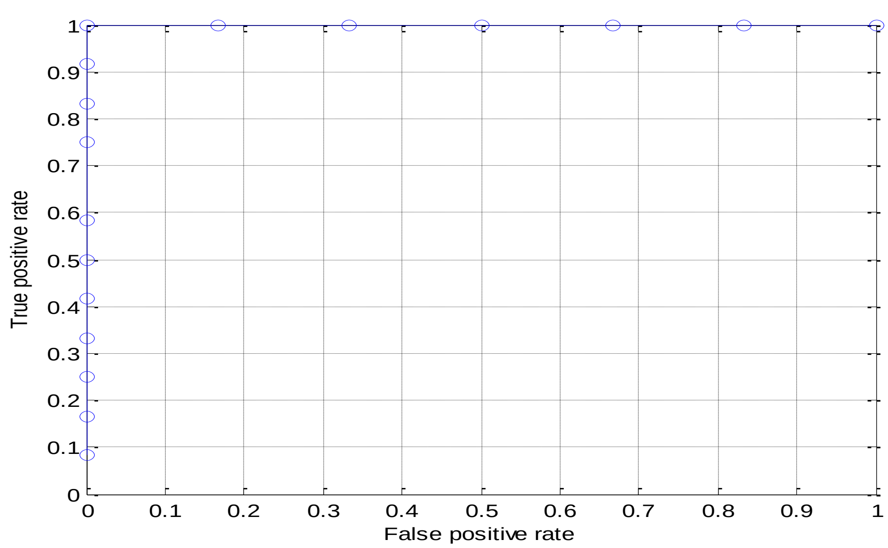

Figure 6.9 ROC curve of a human dorsal position detection.

Table 6.3 Breathing frequency harmonics magnitude ratios at different postures and angles in an office environment.

Angle	Posture	C_f	C_{2f}	C_{3f}	R_{21}	R_{31}
0°	Standing	2.94x10^6	2.80x10^6	1.42x10^6	**0.95**	**0.48**
	Sitting	3.00 x10^5	5.20 x10^5	3.00 x10^5	**1.73**	**1.00**
	Lying	3.50 x10^5	0.75x10^5	0.80x10^4	**0.21**	**0.023**
30°	Standing	2.80 x10^5	1.46 x10^5	1.00 x10^5	**0.52**	**0.35**
	Sitting	8.80 x10^4	7.55 x10^4	3.80 x10^4	**0.86**	**0.43**
	Lying	1.42 x10^6	3.70x10^5	2.34x10^5	**0.26**	**0.16**
60°	Standing	5.00 x10^5	3.00 x10^5	7.00x10^4	**0.60**	**0.14**
	Sitting	1.95 x10^5	1.28 x10^5	5.70 x10^4	**0.66**	**0.29**
	Lying	1.14 x10^5	4.00x10^4	1.4x10^4	**0.35**	**0.12**
90°	Standing	2.16 x10^5	1.83 x10^5	6.40x10^4	**0.85**	**0.29**
	Sitting	1.53 x10^5	4.93 x10^4	1.40 x10^4	**0.32**	**0.09**
	Lying	1.74 x10^5	3.50 x10^4	9.80 x10^3	**0.20**	**0.03**
135°	Standing	4.04 x10^5	3.52 x10^5	8.30x10^4	**0.87**	**0.21**
	Sitting	5.48 x10^5	3.71 x10^5	8.00x10^4	**0.68**	**0.15**
	Lying	1.24x10^5	1.00x10^4	2.37x10^3	**0.08**	**0.02**
180°	Standing	6.20 x10^5	7.10 x10^5	3.28x10^5	**1.14**	**0.53**
	Sitting	1.17 x10^6	1.23 x10^6	2.60 x10^5	**1.05**	**0.22**
	Lying	3.41 x10^4	3.00 x10^3	1000 x10^3	**0.09**	**0.03**

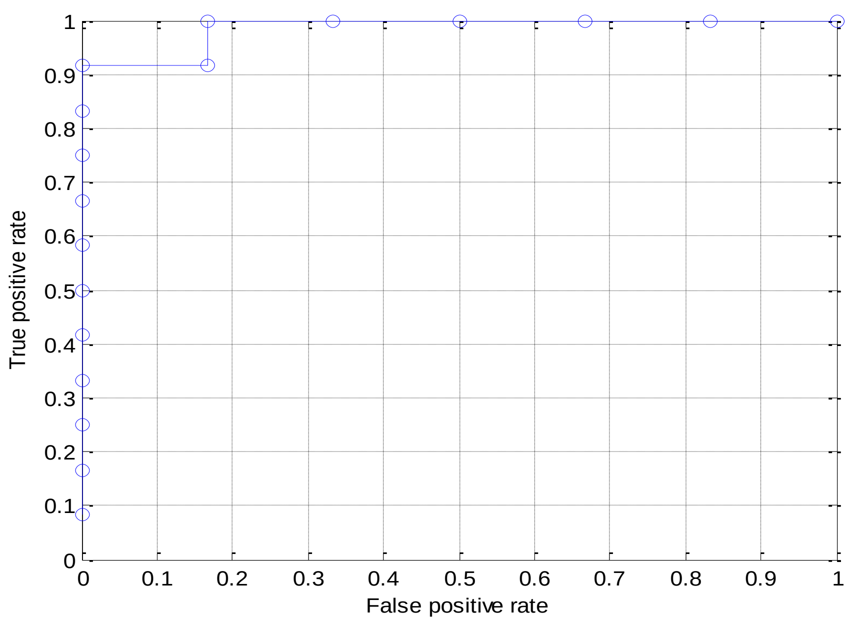

Figure 6.10 ROC curve of a human dorsal position detection in office environment.

6.5.4 Posture Estimation Results Behind Walls

Eighteen measurements were collected in office environment. A human was standing, sitting, and lying down at different angles from the transmitter and the receiver plane, as described in Fig. 6.3. The subject was standing behind a 20 cm thick gypsum wall. Table 6.4 represents C_f, C_{2f} , C_{3f}, R_{21}, and R_{31}.

When studying the ratios R_{21} and R_{31} in different postures, the mean value of R_{21} at different angles was 0.75, 0.57, and 0.12 in standing, sitting, and lying down postures, respectively, with a standard division equal to 0.35, 0.14, and 0.03, respectively. The mean value of R_{31} at different angles was 0.28, 0.15, and 0.04 in standing, sitting, and lying down postures, respectively. Results in table 6.4 show that when the target was standing or sitting the ratios R_{21} and R_{31} was higher than that when he/she was lying down.

Studying the ratio R_{21}in different body orientations, it was noted that the orientation of the human body did not affect the ratios. When a human is lying down the ratios R_{21} are 0.09, 0.16, 0.12, 0.11, 0.08, and 0.14 at orientation angles 0^0, 30^0, 60^0, 90^0, 135^0, and 180^0, respectively. When the target was lying down the ratio $R_{31}$was less than the ratio when he/she was sitting or standing in different orientations.

When the target is sitting and when he is standing, the ratio R_{21} overlapped. It is difficult to discriminate between sitting and standing position behind the wall. However in all measurements, the ratio values of $R_{21}$when the target was sitting or standing were higher than the ratio when he/she was lying down. This feature can be used to detect fallen people on the ground/floor behind the walls.

Figure 6.11 is the ROC curve of the detection of a human in the dorsal position in an office environment, behind a 20 cm thick gypsum wall. The probability of detection is 100% with no false alarms when the threshold Thr is 0.3.

The results in tables 6.2, 6.3, and 6.4 show that the displacements of the abdomen should be included in a human breathing model. The ratios between the human breathing frequency harmonics magnitude are proportional to the displacements of the chest and the abdomen. The displacements of the chest and the abdomen change when the human changes his/her posture. Results show that the ratios R_{21} and R_{31} changed when the posture changed. Minimum ratios were observed while the human was in dorsal supine position. Figures 6.8, 6.9, and 6.10 show that false alarms of human dorsal supine position detection increases in office environments and behind a gypsum wall. In order to identify the posture themselves, these ratios may be inadequate as the distribution of these ratios may have substantial overlap. Hence it may be necessary to identify further features to classify postures.

Table 6.4 Breathing frequency harmonics magnitude ratios at different postures and angles in an office environment behind 20 cm gypsum wall.

Angle	Posture	C_f	C_{2f}	C_{3f}	R_{21}	R_{31}
0°	Standing	$1.86\text{x}10^5$	$1.90\text{x}10^5$	$4.6\text{x}10^4$	**1.02**	**0.25**
	Sitting	$3.00\text{ x}10^5$	$2.03\text{ x}10^5$	$1.00\text{ x}10^5$	**0.68**	**0.33**
	lying	$8.09\text{ x}10^4$	$7.50\text{x}10^5$	$6.00\text{x}10^3$	**0.09**	**0.07**
30°	Standing	$2.83\text{ x}10^5$	$2.84\text{ x}10^5$	$7.80\text{ x}10^4$	**1.00**	**0.28**
	Sitting	$2.64\text{ x}10^5$	$1.00\text{ x}10^5$	$4.20\text{ x}10^4$	**0.38**	**0.16**
	lying	$3.79\text{ x}10^4$	$6.00\text{x}10^3$	$1.80\text{x}10^3$	**0.16**	**0.05**
60°	Standing	$2.70\text{ x}10^5$	$1.08\text{ x}10^5$	$1.00\text{x}10^5$	**0.40**	**0.37**
	Sitting	$5.74\text{ x}10^5$	$2.30\text{ x}10^5$	$5.50\text{ x}10^4$	**0.40**	**0.09**
	lying	$5.45\text{ x}10^4$	$6.80\text{x}10^3$	$1.88\text{x}10^3$	**0.12**	**0.03**
90°	Standing	$4.16\text{ x}10^4$	$2.15\text{ x}10^4$	$6.20\text{x}10^3$	**0.52**	**0.14**
	Sitting	$4.34\text{ x}10^5$	$2.61\text{ x}10^5$	$3.00\text{ x}10^4$	**0.60**	**0.07**
	lying	$4.32\text{ x}10^4$	$4.60\text{ x}10^3$	$2.00\text{ x}10^3$	**0.11**	**0.05**
135°	Standing	$7.10\text{ x}10^5$	$2.67\text{ x}10^5$	$7.00\text{x}10^4$	**0.38**	**0.10**
	Sitting	$5.48\text{ x}10^5$	$3.71\text{ x}10^5$	$8.00\text{x}10^4$	**0.68**	**0.15**
	lying	$1.44\text{x}10^5$	$1.66\text{x}10^5$	$6.00\text{x}10^4$	**0.08**	**0.02**
180°	Standing	$6.20\text{ x}10^5$	$7.10\text{ x}10^5$	$3.28\text{x}10^5$	**1.15**	**0.52**
	Sitting	$1.41\text{x}10^6$	$9.85\text{ x}10^5$	$1.40\text{ x}10^5$	**0.69**	**0.10**
	lying	$4.55\text{ x}10^4$	$6.50\text{ x}10^3$	800	**0.14**	**0.02**

6.6 Breathing Frequency Harmonic Ratios of Different Subjects at Different Ranges

Twenty-seven measurements were collected from 3 subjects breathing normally in standing, sitting, and dorsal positions and at the distances of 1 m, 2 m, and 3 m from the radar and facing the transmitter and receiver antennas. Table 5.1 illustrates the subjects' weight, height, and age. Table 6.5 show C_f, C_{2f}, C_{3f}, R_{21}, and R_{31}. The mean value of R_{21} at different ranges is 0.91, 1.39, and 0.43 in standing, sitting, and lying down postures, respectively, with a standard division equal to 0.43, 1.00, and 0.24, respectively. The mean value of R_{31} at different angles is 0.49, 0.53, and 0.16 in standing, sitting, and lying down postures with a standard division equal to 0.46, 0.43, and 0.10, respectively. Unlike the results for one person, the distribution of these ratios has a substantial overlap. This happens because the displacements of the chest and the abdomen differ from one person to another. Figure 6.12 (a) and (b) represents the ROC curve of human dorsal position detection in an office environment for 3 persons using R_{21} and R_{31}, respectively. The area under the curve was 0.9 and 0.74 in Fig. 6.12 (a) and (b), respectively. It was determined that the performance of the human dorsal position estimator was better using R_{21} ratios.

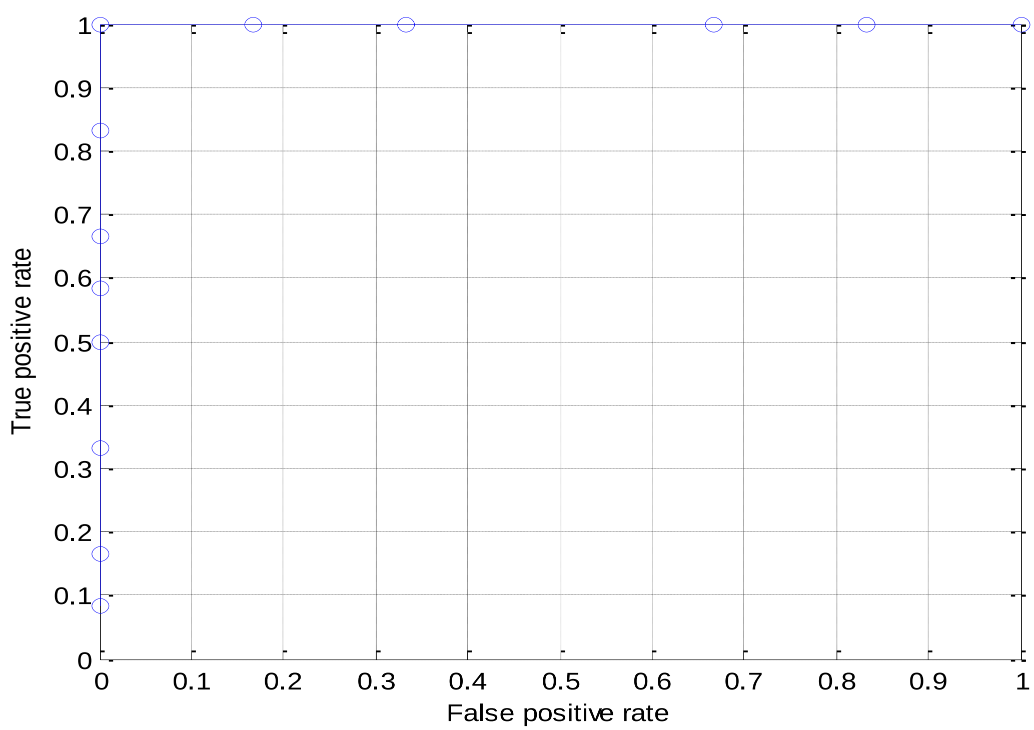

Figure 6.11 ROC curve of a human dorsal position detection in an office environment behind a 20 cm thick gypsum wall.

From Sections 6.5 and 6.6, it was observed that the ratios R_{21} and R_{31} may carry the human posture information of a human breathing in free space or behind an obstacle. These ratios can be used as a feature to extract the posture estimation information.

6.7 Discussion

Observation:

In Chapter 4 and 5 it was observed that the appearance of dominant second harmonics magnitude in the spectrum of the breathing signal caused error in estimating the breathing rate. However, in this chapter, advantage will be taken of detecting the second and third harmonic of breathing frequency to determine posture and posture change of humans.

Table 6.5 Breathing frequency harmonics magnitude ratios of three subjects at different postures and ranges in an office environment.

Subject	Posture	Range	C_f	C_{2f}	C_{3f}	R_{21}	R_{31}
A	*Lying*	1m	1.11x10^6	7.35x10^5	2.02x10^5	**0.66**	**0.18**
	Standing		9.80 x10^5	9.95 x10^5	1.20 x10^5	**1.02**	**0.12**
	Sitting		2.60 x10^5	9.85x10^5	3.50x10^5	**3.78**	**1.35**
	Lying	2m	1.13 x10^6	3.90 x10^5	9.10 x10^4	**0.35**	**0.08**
	Standing		5.40 x10^5	4.42 x10^5	2.18 x10^5	**0.82**	**0.4**
	Sitting		8.35 x10^5	8.51x10^5	9.20x10^4	**1.02**	**0.11**
	Lying	3m	3.59 x10^5	7.20 x10^4	8.20x10^3	**0.20**	**0.37**
	Standing		9.70x10^4	1.73 x10^5	1.5 x10^5	**1.78**	**1.55**
	Sitting		1.19 x10^5	1.44x10^5	7.20x10^4	**1.21**	**0.61**
B	*Lying*	1m	3.58 x10^5	7.20 x10^4	8.20x10^3	**0.20**	**0.00**
	Standing		2.94 x10^6	2.80 x10^6	1.40 x10^6	**0.95**	**0.47**
	Sitting		2.12 x10^6	8.60 x10^5	2.32 x10^5	**0.41**	**0.11**
	Lying	2m	1.42 x10^6	3.70 x10^5	2.34x10^5	**0.26**	**0.16**
	Standing		3.21 x10^5	2.47 x10^5	4.00x10^4	**0.77**	**0.12**
	Sitting		5.35x10^5	9.50x10^5	3.45x10^5	**1.78**	**0.64**
	Lying	3m	1.14 x10^5	4.00 x10^4	1.40x10^4	**0.35**	**0.12**
	Standing		4.45x10^5	1.30 x10^5	2.59x10^5	**0.29**	**0.58**
	Sitting		3.16 x10^5	4.30x10^5	3.13 x10^5	**1.36**	**0.99**
C	*Lying*	1m	5.58 x10^5	4.76 x10^5	1.3 x10^5	**0.85**	**0.23**
	Standing		4.82 x10^5	3.99 x10^5	1.91 x10^5	**0.83**	**0.39**
	Sitting		1.19 x10^6	1.23 x10^6	4.10 x10^5	**1.03**	**0.34**
	Lying	2m	2.23 x10^5	1.57 x10^5	4.00 x10^4	**0.70**	**0.18**
	Standing		7.68 x10^5	9.32 x10^5	5.6 x10^5	**1.21**	**0.73**
	Sitting		6.43 x10^5	2.55 x10^5	7.5 x10^4	**0.40**	**0.12**
	Lying	3m	1.51 x10^6	4.00 x10^5	2.00 x10^5	**0.26**	**0.13**
	Standing		1.65 x10^5	8.00 x10^4	5.5 x10^3	**0.48**	**0.03**
	Sitting		9.5 x10^4	1.41 x10^5	0.50 x10^5	**1.48**	**0.53**

Model:

The phase shift between the chest and the abdomen displacements was included in mathematical model for the breathing signal. The ratios between the second and the third to the first breathing frequency harmonics magnitude changed when the displacements of the abdomen changed. The model was validated by recording the breathing signal reflected from a human breathing with normal breathing and sitting, standing, or lying down at different orientation angles. This was conducted in an anechoic chamber. The results showed that when the human posture changed, the abdominal movements changed, and the ratios $R_{21}$and R_{31} changed.

Algorithms for detecting dorsal posture:

An algorithm to detect the dorsal posture has been proposed in this chapter. The data matrix was applied to a preprocessing algorithm to remove noise from the received signal. After that SVD was applied to remove clutter and to estimate the target range-bin. Hann window was applied to the signal in the slow time direction at the target range-bin. After that, FFT was applied to compute the different breathing harmonic ratios magnitude R_{21} and R_{31}.

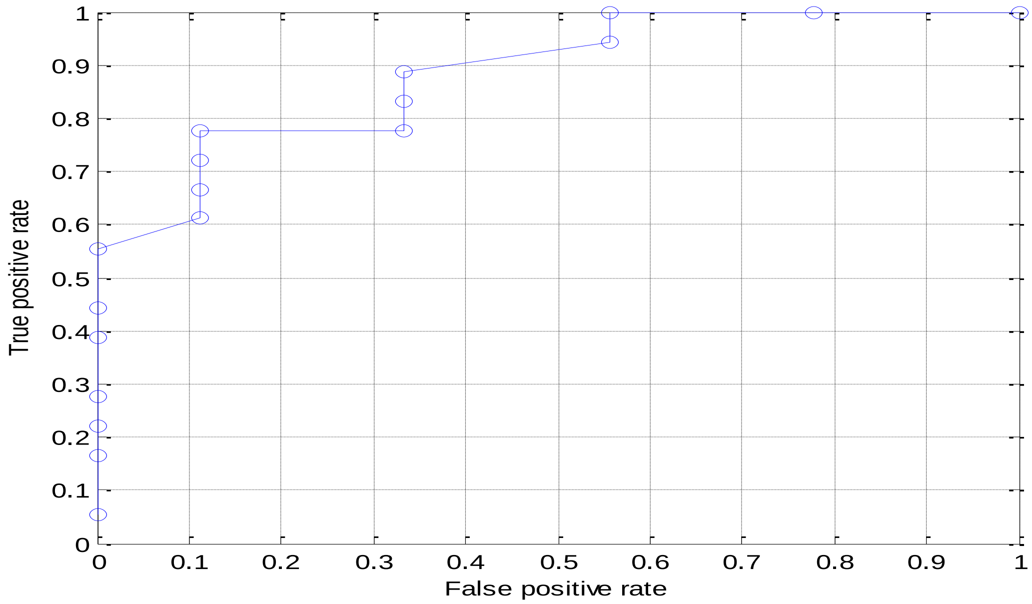

(a)

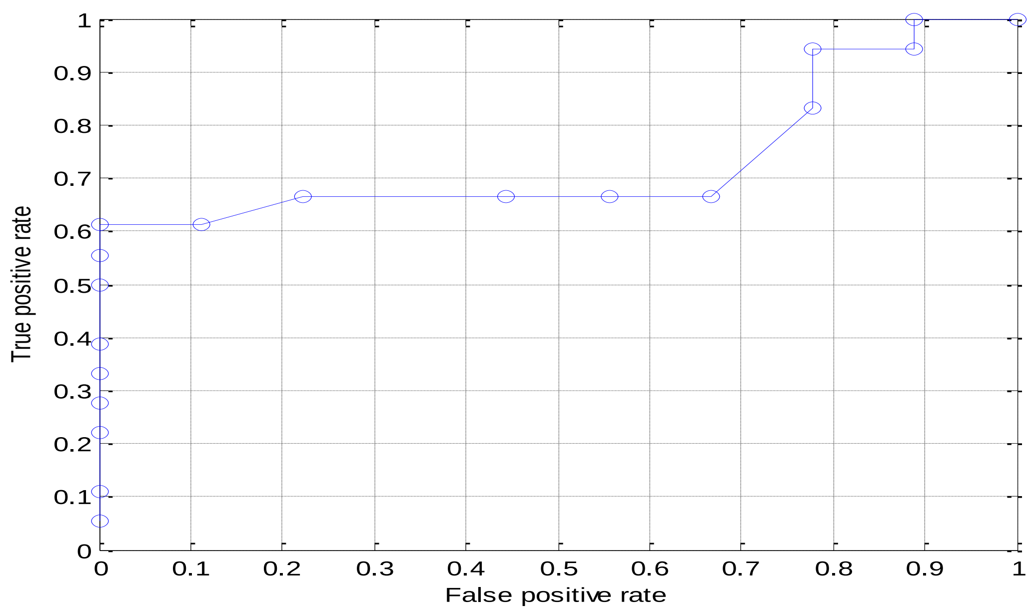

(b)

Figure 6.12 ROC curve of human dorsal position detection in an office environment for 3 persons using (a) R_{21} (b) R_{31} Ratios.

Different experiments done:

Experiments were performed in an anechoic chamber, an office environment, and behind a 20 cm thick gypsum walls at the University of Ottawa, Ottawa, Canada, by recording the reflected signal from a human breathing normally. The subject was sitting, standing, or lying down at different orientation angles. Using the collected data, the performance of the proposed algorithm in detecting the human dorsal posture was studies. After that, 27 measurements were taken in an office environment of the subjects sitting, standing, and lying down at different ranges from the radar. The collected data was used to study the performance of the proposed algorithm when detecting the dorsal posture of three different subjects in an office environment.

Results:

It was found that the ratios between different breathing harmonics $R_{21}$and R_{31} are higher in sitting and standing postures than in the lying down posture. The body orientation does not affect the results. It was also observed that the false alarms in human dorsal supine position detection increased in an office environments and behind walls as opposed to an anechoic chamber. However, the probability of detection was 100% with no false alarms when the threshold Thr was 0.3 in behind the wall scenario.

Limitations:

Although, the proposed algorithm of this research can detect the human dorsal posture in different environments, the algorithm has some limitations including:

- It was found that it is difficult to discriminate between standing and sitting postures because the $R_{21}$and R_{31} ratio values are overlapped in these two postures.
- It was also found that the discrimination between different human postures for many subjects is more difficult than for one subject.

Future work:

In this chapter, a method to extract some posture information from the breathing signal spectrum is proposed. The algorithm distinguished between the human dorsal posture and the sitting or standing postures. However, it was very difficult to distinguish among all three human postures. In future work, an effort will be made to distinguish between the human postures in different environments. Also, an attempt will be made to study the performance of the proposed algorithm behind different types of walls. The feature of changing the value of the ratios in different postures could be combined with some other features such as the distance between the torso and the ground/floor which was proposed in [*40*] to be used in a classifier with the aim of distinguishing between different human postures.

Chapter 7

Conclusions and Future Work

7.1 Conclusions

Human breathing detection in free space and behind the walls is significant in many applications. In military and security applications, it is preferred to obtain all the possible information about the number of people and their postures to estimate the situation behind barriers. In rescue operations, it is very important to detect live people as fast as possible. Obviously, the more time passes the less likely is to find people alive. Obviously, the earlier survivors are detected and rescued, the lower the victim rate. In homecare monitoring applications, the breathing rate and posture monitoring may help save elderly people who live alone and have fallen.

The signal reflected from a human breathing behind a wall is highly attenuated and interfered by electromagnetic wave propagation effects such as fading, shadowing, multipath propagation, etc. UWB radar technology can overcome these problems. Although impulse, random noise, FMCW and SFCW radars have been used in this application, PN-UWB radars have shown impressive results in human detection behind walls. P410 PN-UWB radar produced by Time Domain was used in experimental studies connected with this research.

The main objective of this thesis was to explore different ways to enhance the performance of a human breathing detection system. Chapter two introduced dominant problems which should be solved by a human breathing detection radar system. These problems are: the clutter, multiple signals received from two targets, high errors in the estimated breathing rate, and no posture information being available. To the best of the author’s knowledge, there is no published research that has solved all of these problems using one radar system.

There have been a number of different techniques which researchers used to try to solve these problems. These techniques were reviewed in Section 3. However, there are many questions remaining to be answered.

- The SVD was used in clutter suppression by applying the SVD while keeping the singular value that contains the target information, making other singular values equal to zero, and by inverting SVD to reconstruct the data matrix. However, we need to know *which principal component contains the target information and on what basis the detection threshold should be assigned*. This question was answered in Chapter four by combining the SVD and the skewness test methods. In this thesis, it was possible to detect the target without any prior knowledge of which singular component contained the target information. The skewness of the range profile in the slow time direction was studied. It was observed that the value of the skewness dropped abruptly in a target range-bin. The distribution of the skewness value of the square of the range profile in a target range-bin did not overlap with that in a clutter range-bin allowing for a simple detection threshold method to be applied. The method was tested to detect a human behind a wall. The target was standing 1.5 m behind a 20 cm gypsum wall and data was collected from two subjects in six sets of data. A total 46 measurements were collected. The null hypothesis was not rejected when there was no target. However, target detection was rejected twice out of 46 measurements when there was a target. The results contained no type I error and only 4.34% type II error.

- The received breathing signal may be composed of reflected signals from two breathing targets. It is necessary to study, *how one can distinguish between the two targets*. This question was answered in Chapter four by using the SVD method combined with the skewness test method. As a result, it was possible to distinguish between two targets standing in an anechoic chamber, an office environment, and behind a 20 cm gypsum wall and separated by a distance equal to 1 m, 0.5 m, and 0.3 m between each other.
- It was necessary to determine *why the error of the estimated human breathing rate was high in some scenarios*. This question was answered in Chapter five. A novel mathematical model of the human breathing signal received in PN-UWB radar was proposed. It was noted that the magnitude of the second breathing harmonics was higher than that of the first breathing harmonics in some scenarios. The main reason for the high error in the estimated breathing rate was due to the second breathing harmonic. A novel method was proposed based on zero-crossing with the time interval constraint between each breath. The mean absolute error of the estimated breathing frequency using the zero-crossing method was reduced by 23.13%, 33.46%, and 49.18% in an anechoic chamber, an office environment, and behind a 20 cm gypsum wall, respectively compared with the FFT estimator.
- It was observed that not much effort has been put in remote estimation of the human posture. However, it can be very crucial to estimate the human posture and detect fallen people in many applications. It is important to determine *how one can distinguish between fallen people on the ground/floor and standing or sitting people*. The ratios between the second and the third to the first breathing frequency harmonic magnitudes were used to estimate the human posture and distinguish between lying down and standing or sitting postures.

In brief, proposed solutions to issues related to the human breathing detection behind a wall can enhance the human breathing detection, reduce the number of false alarms, and estimate the human breathing rate accurately. In addition, information could be provided about the human posture in both free space and behind a wall.

7.2 Summary of Contributions

In this research, proposed solutions to the dominant problems related to human breathing detection in both free space and behind the walls were proposed. Although state-of-the-art attempted to solve these problems, there are many remaining issues. These include:

- Reducing errors in the estimated breathing rate in some scenarios.
- Extracting information about the human posture from the breathing signal frequency spectrum.
- Reducing the false alarms in the human breathing detection algorithms.
- Determining what principal component contains the target information when the SVD is used to suppress the clutter.
- Distinguishing between two targets with low false alarm rate.

Below is a list of the major contributions in this research:

- Addressed the problems of the dominant second breathing harmonic in the human breathing rate estimation application.
- Extracted a feature from the breathing signal spectrum which can be used in distinguishing between fallen people on the ground/floor and sitting or standing people.
- Reduced the false alarms in human breathing detection by studying the skewness of the amplitude squared for the range profiles at every range-bin.
- Proposed a new human breathing detection algorithm based on SVD and skewness variations that does not require prior knowledge of which principal component contains the target information.
- Distinguished between two targets separated by 30 cm in free space and behind gypsum wall using SVD combined with skewness variations method.

The contributions from this research solve some of the dominant problems in the human breathing detection radar systems. In this research, unanswered questions by the-state-of-the-art were addressed and an attempted was made to propose methods that can be used to detect human breathing in realistic conditions, distinguish between two targets. In addition attention was given to accurately estimate the breathing rate, and distinguish between lying down posture and sitting or standing posture.

7.3 Suggestions for Future Work

There are several different ways this research could be extended in the future. Some of these are as follows:

- Respiratory patterns vary according to the injury and victim stress level. By studying the respiratory pattern of a human, the degree of injury and the stress level can be estimated. Our proposed human breathing rate estimation method, as presented in this research can estimate the human breathing rate in a short-time window and can detect the stop-breathing or accelerating-breathing events. The results of this research could be extended by using this information in a classification method to identify the breathing patterns of a human behind walls and to detect a stress level mark.

- The human breathing detection was studied in both free space and behind the wall. The proposed human breathing detection algorithm reduced the false alarms. This research could be extended by studying the human breathing detection under rubble or snow. A goal for the future is to solve all the problems introduced in Section 2.3, introduce a new approach to reject the false alarms, and build a rescue radar system that can provide the rescue teams with the estimated breathing rate and a received stress mark from that target.

- Although the proposed method for human breathing detection can distinguish between two targets, a goal for the future will be to have the ability to estimate the number of targets behind a wall (more than two targets). As confirmed in this present research, the main problem in multi-target discrimination is the existence of false targets which are generated away from the real targets. The false targets are generated by multipath for the reflected waves. One suggested solution for this problem is to combine between this present research's algorithm and the algorithm presented in [*32*]. Any ghosts will be eliminated by using the algorithm in [*32*], then the method to discriminate between multiple targets can be applied. . Another solution is to use multiple transmitters and receivers and apply the proposed detection algorithm.

- Although the ratios between the second and the third to the first breathing frequency harmonics magnitude in lying down posture are less than that in standing or sitting postures in free space, an office environment, and behind a 20 cm gypsum wall, the ratios in standing posture were higher than that in sitting posture behind the walls. This present research could be extended by studying ratios between the various breathing frequency harmonics magnitude behind different types of walls or under rubble. The goal is to find the most suitable feature that can be used alone to discriminate between the different human postures.

- In our work, we have not considered the Blind Source Separation (BSS) methods to distinguish between the clutter and targets. In the future work, we will use one of the available BBS methods to distinguish between clutter and human targets and we will compare between it and the SVD combined with the skewness test method.

References

[1] E.F. Greneker, "Radar Sensing of Heartbeat and Respiration at a Distance with Security Applications," *Proceedings of SPIE, Radar Sensor Technology II*, vol. 3066, no. 22, pp. 22-27, June 1997.

[2] H. R. Chuang *et al*. , "Microprocessor-Controlled Automatic Clutter-Cancellation Circuits for Microwave Systems to Sense Physiological Movements Remotely Through the Rubble," in *7th IEEE Instrumentation and Measurement Technology Conference IMTC-90*, San Jose, 1990, pp. 177-181.

[3] E. J. Baranoski, "Through Wall Imaging: Historical Perspective and Future Directions," in *IEEE International Conference on Acoustics, Speech and Signal Processing (ICASSP)*, Nevada, 2008, pp. 5173-5176.

[4] A. G. Yarovoy *et al*., "Comparison of UWB Technologies for Human Being Detection with Radar," in *European Radar Conference (EuRAD 2007)*, Munich, 2007, pp. 295-298.

[5] A. G. Yarovoy *et al*., "UWB Radar for Human Being Detection," *Aerospace and Electronic Systems Magazine*, vol. 23, no. 5, pp. 36-40, May 2008.

[6] G. Ossberger *et al*., "Non-Invasive Respiratory Movement Detection and Monitoring of Hidden Humans using Ultra Wideband Pulse Radar," *International Workshop on Ultrawideband Systems and Technologies IWUWBS*, Kyoto, 2004, pp. 395-399.

[7] I. Y. Immoreev *et al*., "Short-Distance Ultra-wideband Radars," *IEEE Aerospace and Electronic Systems Magazine*, vol. 20, no. 6, pp. 9-14, June 2005.

[8] H. Burchett, "Latest Advances in Through-Wall Radar Sensing for Security Applications," *Conference on Crime and Secuirity*, London, 2006, pp. 511-525.

[9] B. Levitas and J. Matuzas, "UWB Radar for Breath Detection," *11th International Radar Symposium*, Vilnius, 2010, pp. 1-3.

[10] A. Nezirovic *et al*., "Narrowband Interference Suppression in UWB Impulse Radar for Human Being Detection," in *IEEE International Conference on Ultra-Wideband*, Singapore, 2007, pp. 56-61.

[11] A. Nezirovic *et al*., "Experimental Study on Human Breathing Cross Section using UWB Impulse Radar," in *5th European Radar Conference*, Amsterdam, 2008, pp. 1-4.

[12] L. Liu *et al*.," Through-Wall Bio-Radiolocation with UWB Impulse Radar: Observation, Simulation and Signal Extraction," *IEEE Journal of Selected Topics in Applied Earth Observations and Remote Sensing*, vol. 4, no. 4, pp. 791-798, December 2011.

[13] J. Li *et al*.,"Through-Wall Detection of Human Being's Movement by UWB Radar," IEEE Geosci. Remote Sens., vol. 9, no. 6, pp. 1079-1083, November 2012.

[14] Z. Yang *et al*., "Detecting and Identifying Two Stationary-Human-Targets: A Technique Based on Bioradar," *First International Conference on Pervasive Computing Signal Processing and Applications (PCSPA)*, Harbin, 2010, pp. 981-985.

[15] Y. Zhang *et al*., "A Detecting and Identifying Method for Two Stationary Human Targets Using Single-Channel Ultra-Wideband Radar," *Journal on Advances in Signal Processing EURASIP*, pp. 1-6, September 2012.

[16] R. R. Jr. Leach *et al*., "Trough wall detection and tracking system," A2 WO 2007/001368, January 4, 2007.

[17] United States Geological Survey (USCG). (2013, May) Earthquakes with 50,000 or More Deaths. [Online]. http://earthquake.usgs.gov/earthquakes/world/most_destructive.php

[18] T. R. Frieden, "The State of Aging and Health in America," Centers for Disease Control and Prevention, Atlanta, 2013.

[19] Administration on Ageing, "A Profile of Older Americans: 2012," U.S. Department of Health and Human Services, Washington, D.C., 2012.

[20] P. E. Cuddihy *et al*., "Radar Based Systems and Methods for Detecting a Fallen Person," B2 8742935, June 3, 2014.

[21] M. Singh and G. Ramachandran, "Reconstruction of sequential cardiac in-plane displacement patterns on the chest wall by laser speckle interferometry," *IEEE Transactions on Biomedical Engineering*, vol. 38, no. 5, pp. 483-489, May 1991.

[22] L. Zheng and S.Hui-xia, "Micro-Doppler Analysis and Application of Radar Targets," in *International Conference on Information and Automation*, Zhangjiajie, 2008, pp. 1343-1347.

[23] A. Nezirovic *et al*., "Experimental Verification of Human Being Detection Dependency on Operational UWB Frequency Band," in *IEEE International Conference on Ultra-Wideband*, Singapore, 2007, pp. 305-310.

[24] S. Singh *et al*., "Sense Through Wall Human Detection Using UWB Radar," *Journal on Wireless Communications and Networking, EURASIP*, pp. 1-11, June 2011.

[25] N. Maaref *et al*., "A Study of UWB FM-CW Radar for the Detection of Human Beings in Motion inside a Building," *IEEE Transactions on Geoscience and Remote Sensing*, vol. 47, no. 5, pp. 1297-1300, May 2009.

[26] A. Nezirovic, "Trapped Victim Detection in Post-Disaster Scenarios Using Ultra-Wideband Radar," Dept. Elect. Eng., Delft Univ., Delft, Netherlands, PhD. dissertation 2010.

[27] M. Baboli *et al*., "A New WaveletBased Algorithm for Estimating Respiratory Motion Rate Using UWB Radar," in *International Conference on Biomedical and Pharmaceutical Engineering*, Singapore, 2009, pp. 1-3.

[28] Z. Li *et al*., "A Wavelet–Based Strong Clutter Removal Technique for UWB Life Detection," in *14th International IEEE Conference on Ground Penetrating Radar (GPR)*, Shangahi, 2012, pp. 957- 960.

[29] A. Lazaro *et al*., "Techniques for Clutter Suppression in the Presence of Body Movements during the Detection of Respiratory Activity Through UWB Radars," *Journal of Sensors*, vol. 14, no. 2, pp. 2595-2618, February 2014.

[30] C. Li, "Non-contract Estimation of Respiration and Heartbeat Rate using Ultra-Wideband Signals," Dept. Elect. Eng., Virginia Tech, Blacksburg, Virginia, M.S. thesis 2011.

[31] A. Lazaro *et al*., "Analysis of Vital Signs Monitoring Using an IR-UWB Radar," *Electromagnetics Research*, pp. 265-284, 2010.

[32] Y. F. Li *et al*., "Analysis of Characteristics of Two Close Stationary Human Targets Detected by IM-Pulse Radio UWB Radar," *Progress In Electromagnetics Research*, vol. 126, pp. 429-447, March 2012.

[33] L. Anitori *et al*., "FMCW Radar for Life-Sign Detection," in *IEEE Radar Conference*, Bordeaux, 2009, pp. 1-6.

[34] R. M. Narayanan *et al*., "Through-the Wall Detection of Stationary Human Targets Using Doppler Radar," *Progress in Electromagnetics Research B*, vol. 20, pp. 147-166, 2010.

[35] Hao Lv *et al*., "Characterization and Identification of IR-UWB Respiratory-Motion Response of Trapped Victims," *IEEE Geoscience and Remote Sensing*, vol. 52, no. 11, pp. 7195- 7204, November 2014.

[36] M. Ganesh *et al*., "Physiology monitoring and alerting system and process," U.S. Patent 0 245 479, September 27, 2012.

[37] C. D. Cook *et al*., "Mobile sense through the wall radar system," U.S.Patent 8 169 362, May 1, 2012.

[38] E. T. Rosenbury, "Handheld instrument capable of measuring heartbeat and breathing motion at a distance," U.S.Patent 7 898 455, March 1, 2011.

[39] W. H. Dwelly and V. N. Adams, "Biometric radar system and method for identifying persons and positional states of persons," U.S.Patent 8 026 840, September 27, 2011.

[40] J. Osterweil, "Method and appartous for a body position monitor using radar," U.S.Patent 7 567 200, November 29, 2011.

[41] L. Liu *et al*., "An Automatic Fall Detection Framework Using Data Fusion of Doppler Radar and Motion Sensor Network," *EMBC2014*, Chicago, 2014.

[42] L. Liu *et al*., "Doppler Radar Sensor Positioning in a Fall Detection System," *EMBS2012*, San Diego, 2012, pp. 256-259.

[43] L. Liu *et al*., "Fall Detection Using Doppler Radar and Classifier Fusion ,"*IEEE-EMBS International Conference on Biomedical and Health Informatics* (*BHI 2012*) , Hong Kong and Shenzhen, 2012, pp. 180-183.

[44] T. Yardibi *et al*., "Gait Characterization via Pulse-Doppler Radar," *IEEE International Conference on Pervasive Computing and Communications Workshops*, Seattle, 2011, pp. 662-667.

[45] L. Liu *et al*., "Automatic Fall Detection Based on Doppler Radar Motion Signature," *5th International Conference on Pervasive Computing Technologies for Healthcare* (*PervasiveHealth*) *and Workshops*, Dublin, 2011, pp. 222-225.

[46] J. Sachs *et al*., "Detection and Tracking of Moving or Trapped People Hidden by Obstacles using Ultra-Wideband Pseudo-Noise Radar," in *The 5th European Radar Conference*, Amsterdam, 2008, pp. 408-411.

[47] A. Beeri, "Through-The-Obstacle Radar System and Method of Operation," B2 US8098186, November 28, 2007.

[48] S. Quirk *et al*., "External Respiratory Motion Analysis and Statstics for Patients and Volunteers," *Journal of Applied Clinical Medical Physics*, vol. 14, no. 2, pp. 90-101, 2013.

[49] A.S. Bugaev *et al*., "Through Wall Sensing of Human Breathing and Heart Beating by Monochromatic Radar," in *10th Conf. on Ground Penetrating Radar*, Delft, 2004, pp. 291-294.

[50] J. P. Edgcombe, "Latest advances in through-wall radar sensing for security applications," *Sensor Review*, vol. 28, no. 3, pp. 205 – 211, 2008.

[51] K. M. Chen *et al*., "An X-band microwave distant life-detection system," *IEEE Transactions on Biomedical Engineering*, vol. BME-33, no. 7, pp. 697-701, July 1986.

[52] A. Ruengwaree, *Design of UWB Radar Sensors*. Kassel, Germany: Kassel University press, 2007.

[53] J. Pan and R. Jain, "Medical Applications of Ultra-Wideband (UWB),"survey paper, Washington University in St. Louis, Hadley, 2008.

[54] T. E. McEwan, "Body monitoring and imaging apparatus and method," U.S.Patent 5 573 012 , November 12, 1996.

[55] B. Levitas and J. Matuzas, "UWB Radar for Human Being Detection Behind the Wal," in *International Radar Symposium*, Krakow, 2006, pp. 1-3.

[56] V. Chernyak, "Signal Processing in Multisite UWB Radar Devices for Searching Survivors in Rubble," in *3rd European Radar Conference*, Manchester, 2006, pp. 190-193.

[57] D. C. Bell and R. M. Narayanan, "Theoretical Aspects of Radar Imaging Using Stochastic Waveforms," *IEEE Transactions on Signal Processing*, vol. 49, no. 2, pp. 394-400, February 2001.

[58] R. M. Narayanan and X. Xu, "Principles and applications of coherent random noise radar technology," *Porc. SPIE* , vol. 5113, pp. 503-514, June 2003.

[59] R. M. Narayanan *et al*., "Radar penetration imaging using ultra wideband (UWB) random noise waveforms," *IEEE Proceedings on Radar, Sonar and Navigation*, vol. 151, no. 3, pp. 143-148, June 2004.

[60] C-P Lai, "Through Wall Surveillance Using Ultra Wide Band Random Noise Radar," Dept. Elect. Eng., Pennsylvania state Univ., Pennsylvania, PhD. Dissertation 2007.

[61] C-P Lai and R. M. Narayanan, "Ultra-wideband Random Noise Radar Design for Through-Wall Surveillance," *IEEE Transactions on Aerospace and Electronic Systems*, vol. 47, no. 4, pp. 1716-1730, October 2010.

[62] G. Grazzini *et al*., "An Ultra-Wideband High-Dynamic Range GPR for detecting buried people after collapse of buildings using SFCW radar," in *13th International Conference on Ground Penetrating Radar (GPR)*, Lecce, 2010, pp. 1-6.

[63] X. Zhuge, "Short-Range Ultra-Wideband Imaging with Multiple-Input Multiple-Output Arrays," Dept. Elect. Eng., Delft Univ, Delft, PhD. Dissertation 2010.

[64] X. Zhuge *et al*., "Assessment of Electromagnetic Requirements for UWB Through-Wall Radar," in *International Conference on Electromagnetics in Advanced Applications ICEAA*, Torino, 2007, pp. 923 – 926.

[65] Kun-Mu Chen *et al*., "Microwave Life-Detection Systems for Searching Human Subjects under Earthquake Rubble or behind Barrier," *IEEE Transactions on Biomedical Engineering*, vol. 27, no. 1, pp. 105-114, January 2000.

[66] H. J. Kim *et al*., "Measurement of Human Heartbeat and Respiration Signals Using Phase Detection Radar," *Review of Scientific Instruments*, vol. 78, no. 10, pp. 104703 - 104703-3, October 2007.

[67] M. Pieraccini *et al*., "Detection of Breathing and Heartbeat Through Snow Using a Microwave Transceiver," *IEEE Geoscince and Remote Sensing*, vol. 5, no. 1, pp. 57-59, January 2008.

[68] Q. Liu *et al*., "A Compact Integrated 100 GS/s Sampling Module for UWB See Through Wall Radar with Fast Refresh Rate for Dynamic Real Time Imaging," in *IEEE Radio and Wireless Symposium (RWS)*, Santa Clara, 2012, pp. 59-62.

[69] Z. Li *et al*., "A Novel Method for Respiration-Like Clutter Cancellation in Life Detection by Dual-Frequency IR-UWB Radar," *IEEE Transactions on Microwave Theory and Techniques*, vol. 61, no. 5, pp. 2086-2092, May 2013.

[70] Z. Zhang *et al*., "Human-Target Detection and Surrounding Structure Estimation under a Simulated Rubble via UWB Radar," *IEEE Geoscience and Remote Sensing Letters*, vol. 10, no. 2, pp. 328-331, March 2013.

[71] C. Kim and J.Lee, "ToA-based Multipath Localization and Respiration Detection Using UWB Radars," *EURASIP Joural on Wireless Communications and Networking*, pp. 2-15, 2014.

[72] G. F. Ross *et al*., "Next generation Ultra-Wideband (UWB) intrusion detection radar," Defence Nuclear Agency, Alexandria, Technical report DNA-TR-94-184, 1996.

[73] A. Sume *et al*., "Radar detection of moving targets behind corners," *IEEE Geoscience and Remote Sensing Letter*, vol. 49, no. 6, pp. 2259-2267, June 2011.

[74] I.Y. Immoreev *et al*., "Short-Distance Ultra-wideband Radars," *IEEE Aerospace and Electronic Systems Magazine*, vol. 20, no. 6, pp. 9-14, June 2005.

[75] F.H.C. Tivive *et al*., "An SVD-based Approach for Mitigating WallReflections in Through-the-Wall Radar Imaging," in *IEEE Radar Conference*, Kansas, 2011, pp. 519-524.

[76] M. G. Amin, "Radar, signal, and image processing techniques for through the wall imaging (Keynote Paper)," *Proceeding of SPIE*, vol. 5819, pp. 33-45, July 2005.

[77] D. J. Daniels, *Ground Penetrating Radar*. London, United Kingdom: London: Institution of Electrical Engineers, 2004.

[78] A. Kumar, "Experimental Study of Through-Wall Human Being Detection Using Ultra-Wideband Radar," Dept. Elect. Eng., U. T. Arlington, Arlington, M.S. thesis 2011.

[79] TIME DOMAIN. (2013, October) PulsON®410, P410 radar kit. [Online]. http://www.timedomain.com/

[80] A. Nezirovic , A.G. Yarovoy , and L.P. Ligthart, "Experimental study on human being detection using UWB radar," in *International Radar Symposium*, Kraków, 2006, pp. 1-4.

[81] S. Haykin and C. Deng, "Classification of Radar Clutter Using Neural Networks," *IEEE Transactions and Neural Networks*, vol. 2, no. 6, pp. 589-600, November 1991.

[82] D. G. Falconer *et al*., "Robot-Monted Through-Wall Radar for Detecting, Locating, and Identifying Building Occupant," *IEEE Conference on Robotics & Automation*, San Francisco, 2000, pp. 1868-1875.

[83] E. Conte *et al*. "Statistical Analysis of Real Clutter at Different Range Resolutions," *IEEE Aerospace and Electronic Systems Magazine*, vol. 40, no. 3, pp. 903-918, July 2004.

[84] L. Shen *et al*., "Human Detection Based on the Excess Kurtosis in the Non-stationary Clutter Environment Using UWB Impulse Radar," *International Asia-Pacific conference on Synthetic Aperture Radar* (*APSAR*), Seoul, 2011, pp. 1-4.

[85] M. A. Richards, *Fundamentals of Radar Signal Processing*. New York, USA: MC Graw-Hil, 2005.

[86] C.Y. Lai *et al*., "Wireless Sensing of Human Respiratory Parameters by Low-Power Ultrawideband Impulse Radio Rada," *IEEE Transactions on Instrumentation and Measurements*, vol. 60, no. 3, pp. 928-938, March 2011.

[87] Y. Xu *et al*., "A Novel Method for Automatic Detection of Trapped Victims by Ultrawideband Radar," *IEEE Geoscience and Remote Sensing Magazine*, vol. 50, no. 8, pp. 3132-3142, August 2012.

[88] F. Mohamadi *et al.*, "Deternination of hostile individuals armed with weapon, using respiration and heartbeat as well as spectral analysis at 60 GHz," U.S.Patent 8 354 234, January 22, 2013.

[89] A. Wiesner, "Method and system for detecting vital signs of living bodies," U.S.Patent 0 189 740, July 30, 2009.

[90] Y. Chen, E. Gunawan , K. S.Low , C. B. Soh, and L. L. Thi , "Human respiration rate estimation using body-worn ultra-wideband radar," in *Antennas and Propagation Society International Symposium*, Honolulu, 2007, pp. 265-268.

[91] T. Ballal *et al*., "Breathing Rate Estimation from a Non-Contact Biosensor Using an Adaptive IIR Notch Filter," in *IEEE Topical Conference on Biomedical Wireless Technologies, Networks, and Sensing*, Santa Clara, 2012, pp. 5-8.

[92] Y. Liao, "Phase and Frequency Estimation: High-Accuarcy and Low-Complexity Techniques," Dept. Elect. Eng., WPI Univ., Worcester, Ms.C. dissertation 2011.

[93] P. v. Dorp and F.C.A. Groen, "Human walking estimation with radar," *IEE Proc. Radar, Sonar, and Navigation*, vol. 150, no. 5, pp. 356-365, October 2003.

[94] S. Z. Gürbüz , "Radar detection and identification of human signatures using moving platforms," Georgia Institute of Technolog, Georgia, PhD. Dissertation 2009.

[95] S. Venkatesh *et al*., "Implementation and analysis of respiration-rate estimation using impulse-based UWB," in *IEEE Military Communications Conference (IEEE Milcom'05)*, Atlantic City, 2005, pp. 3314-3320.

[96] J. E. Kiriazi *et al*., "Modeling of human torso time-space characteristics for respiratory effective RCS measurements with Doppler radar," in *IEEE International Microwave Symposium Digest (MTT)*, Baltimore, 2011, pp. 1-4.

[97] Luis B. Almeida, *Nonlinear Source Separation*. Lisboa, Portugal: Morgan & Claypool, 2006.

[98] S.H Jensen *et al*., "Reduction of Broad-Band Noise in Speech by Truncated QSVD," *IEEE Transactions on Speech and Audio Processing*, vol. 3, no. 6, pp. 439– 448, November 1995.

[99] K. Hermus *et al*., "Fully Adaptive SVD-Based Noise Removal for Robust Speech Recognition," *Sixth European Conference on Speech Communication and Technology*, Budapest, 1999, pp. 1951–1954.

[100] K.-C. Lee *et al*., "Application of SVD Noise-Reduction Technique to PCA Based Radar Recognation," *Progress In Electromagnetics Research, PIER 81*, pp. 447–459, 2008.

[101] B. Zhang and W. Wang, "Through-Wall Detection of Human Being with Compressed UWB Radar Data," *Journal on Wireless Communications and Networking*, pp. 1-7, June 2013.

[102] I. Ipsen, *Numerical Matrix Analysis*, USA: Society of industrial and applied Mathematics (siam), 2009.

[103] D. A. Shnidman, "Generalized radar clutter model," *IEEE Transactions on Aerospace and Electronic Systems*, vol. 35, no. 3, pp. 857-865, March 1999.

[104] R. B. D'agostino and M. A. Stephens, , *Goodness-of-Fit Techniques*, Burnaby, Canada: Marcel Dekker, Inc., 1986.

[105] N. Patwari *et al*., "Monitoring Breathing Via Signal Strength in Wireless Networks," Cornell University, Tech. Rep. arXiv:1109.3898v1 [cs.NI], 2013.

[106] D. Rife and R. R. Boorstyn, "Single-tone parameter estimation from discrete-time observations," *IEEE Transactions on Information Theory*, vol. 20, no. 5, pp. 591–598, September 1974.

[107] D. Rife, "Digital tone parameter estimation in the presence of Gaussian noise," Polytechnic Institute of Brooklyn, Brooklyn, PhD thesis 1973.

[108] T.J. Abatzoglou, "A fast maximum likelihood algorithm for frequency estimation of a sinusoid based on Newton's method," *IEEE transactions on acoustics, speech, and signal processing*, vol. 33, no. 1, pp. 77-89, February 1985.

[109] M.D. Macleod, "Fast nearly ML estimation of the parameters of real or complex single tones or resolved multiple tones," *IEEE Transactions on Signal Processing*, vol. 46, no. 1, pp. 141–148, January 1998.

[110] J. Moorer, "The optimum Comb Method of Pitch Period Analysis of Continuous Digitized Speech," *IEEE Trans. Acoust., Speech, Signal Process.*, vol. 22, no. 5, pp. 330-338, October 1974.

[111] C. Shahnaz *et al*., "Pitch Estimation Based on a Harmonic Sinusoidal Autocorrelation Model and a Time-Domain Matching Scheme," *IEEE Transactions on Audio, Speech, and Language Processing* , vol. 20, no. 1, pp. 322-335, January 2012.

[112] M. G. Christensen, "Lecture Notes in Audio Analysis: Pitch Estimation for Dummies," Aalborg University, Aalborg, Audio Analysis Lab 2013.

[113] V. Friedman, "A Zero Crossing Algorithm for the Estimation of the Frequency of a Signal Sinusoid in White Noise," *IEEE Transactions on Signal Processing*, vol. 42, no. 6, pp. 1565-1569, June 1994.

[114] R. G. Wiley, "Approximate FM Demodulation Using Zero Crossings," *IEEE Transactions on Communications*, vol. COM-29, no. 7, pp. 1061-1065, July 1981.

[115] D. R. Brown III *et al*., "Low-complexity Real-time Single-tone Phase and Frequency Estimation," in *2010 Military Communication Conference*, San Jose, 2010, pp. 1-6.

[116] CleveMed™. (2014, March) BioCapture. [Online]. http://www.clevemed.com/.

[117] MAST TECHNOLOGIES. (2014 , July) RF absorbers, MF32-0002-00. [Online]. http://.www.masttechnologies.com/products/convoluted-foam/mf32-0002-00

[118] L. W. Fullerton and J. L. Richards, "System and Method for Intrusion Detection Using a Time Domain Radar Array," U.S. Patent 6 400 307, August 9, 2001.

[119] A. Cereti *et al*., "Electromagnetic Measurements on Martian Soil Analogs: Implications for MARSIS and SHARAD Radars in Detecting Subsoil Water," *Planetary and Space Science*, vol. 55, pp. 193-202, January 2007.

[120] D. Mukherjee *et al*., "Geoelectrical Constraints on Radar Probing of Shallow Water-Saturated Zones within Karstified Carbonates in Semi-Arid Environments," *Journal of Applied Geophysics*, vol. 70, no. 3, pp. 181-191, March 2010.

[121] E. Pettinelli *et al.*, "Electromagnetic Propagation Features of Ground-Penetrating Radars for the Exploration of Martian Subsurface," *Near Surface Geophysics*, vol. 4, no. 1, pp. 5-11, February 2006.

[122] D. Gómez-Ortiz *et al.*, "Joint Application of Ground Penetrating Radar and Electrical Resistivity Imaging to Investigate Volcanic Materials and Structures in Tenerife (Canary Islands, Spain)," *Journal of applied geophysics*, vol. 62, no. 3, pp. 287-300, July 2007.

[123] F. Sh. A. Ghasemi and M. S. Abrishamian, "A Novel Method for FDTD Numerical GPR Imaging of Arbitrary Shapes Based on Fourier transform," *Non-destructive Testing and Evaluation International*, vol. 40, no. 2, pp. 140–146, March 2007.

[124] A. Loizos and C. Plati, "Accuracy of Ground Penetrating Radar Horn-Antenna Technique for Sensing Pavement Subsurface," *IEEE Sensors journal*, vol. 7, no. 5, pp. 842-850, May 2007.

[125] T. Saarenketo, "Recommendations for Guidelines for The Use of GPR in Construction Quality Control," INTERREG, Sweden, Project 2011.

[126] M. Amin and F. Ahmand, "Change Detection Analysis of Humans Moving Behind Walls," *IEEE Transactions on Aerospace and Electronic Systems*, vol. 9, no. 3, pp. 1410-1425, July 2013.

[127] X. Zhuge *et al*., "Assessment of Electromagnetic Requirements for UWB Through-Wall Radar," in *International Conference on Electromagnetics in Advanced Applications ICEAA*, Torino, 2007, pp. 923 – 926.

[128] K. M. Chen, "An X-band microwave distant life-detection system," *IEEE Transactions on Biomedical Engineering*, vol. BME-33, no. 7, pp. 697-701, July 1986.

[129] Y. Xiao *et al*., "Single-channel UWB-based radar type life detection instrument for multi-target detection," Patent 102008291B, March 14, 2012.

[130] L. Hao *et al*., "Method for identifying and one-dimensionally positioning multiple human body targets by using single-channel UWB-based radar life detection instrument," Patent 102018515 B, March 21, 2012.

[131] W. Qi *et al*., "UVB based multi-channel radar life detection instrument," Patent 102058411B, May 8, 2013.

Appendix A

File Number: H05-13-18 **Date (mm/dd/yyyy):** 09/10/2013

Université d'Ottawa University of Ottawa

Bureau d'éthique et d'intégrité de la recherche Office of Research Ethics and Integrity

Ethics Approval Notice

Health Sciences and Science REB

Principal Investigator / Supervisor / Co-investigator(s) / Student(s)

First Name	Last Name	Affiliation	Role
Miodrag	Bolic	Engineering / Computer Science	Principal Investigator
Huthaifa	Abderahman	Engineering / Others	Co-investigator
Seddigheh	Baktash	Engineering / Others	Co-investigator
Hilmi	Dajani	Engineering / Others	Co-investigator
Voicu	Groza	Engineering / Computer Science	Co-investigator
Mohamed	Mabrouk	Engineering / Others	Co-investigator

File Number: H05-13-18

Type of Project: Professor

Title: Detection of human being behind wall using pulsed UWB radar

Approval Date (mm/dd/yyyy)	Expiry Date (mm/dd/yyyy)	Approval Type
09/10/2013	09/09/2014	Ia

(Ia: Approval, Ib: Approval for initial stage only)

Special Conditions / Comments:
N/A

Appendix B

Detailed survey of the state of the art of using NB and UWB technology in detection behind walls.

Narrow Band Radar Technology (under non-realistic conditions)								
Index	**Author**	**Type of paper**	**Problem addressed**	**Technical Requirements**			**Solutions**	
				Trans. Power (mW)	**BW**	**SNR/Depth**	**Method**	**Main results**
1	H.R. Chuang et al, 1990.	Conference [*2*].	P1	10-20	Center frequency 2 GHz and 10 GHz	Not Available (NA)/3 Feet.	Used clutter-cancellation circuits for microwave systems to sense physiological movements remotely through the rubble.	Target was detected successfully.
2	A.S. Bugaev et al, 2004.	Conference [*49*].	P1	10	Center frequency of 1.6 GHz	NA/10 cm brick wall.	Human was seated at a distance 1m from the wall. The radar antenna was covered by antiradar coating $2m^2$. Mathematical model was introduced.	Target has been detected successfully.
3	M. Pieraccini et al., 2008.	IEEE Letters [*67*].	P1	10	Center frequency is 2.42 GHz.	NA/1.8 m thick snow barrier as well as through 1.2 m thick roof of an igloo dugout.	Detection of breathing and heartbeat through snow using a microwave transceiver.	The target was detected behind dry snow. It will be difficult with wet snow. The attenuation of wet snow was higher.
Narrow Band Radar Technology (under realistic conditions)								
1	K-M. Chen, et al, 2000.	IEEE Transactions [*65*].	P1, P2	400	Center frequency 1150 MHz or 450 MHz	NA/10-ft thickness of rubble.	NBCW radars used to detect human subjects under earthquake rubble or behind a barrier.	EM wave of 450 MHz was difficult to penetrate layers of reinforced concrete slabs with imbedded metallic wire of 4-in spacing. 1150 MHz can penetrate these layers.
UWB Impulse Radar Technology (under non-realistic conditions)								
1	G. Ossberger et al., 2004.	Conference [*6*].	P1	NA	0.33 GHz	NA/Target was standing 5 meters away behind a 20 cm thickness wall.	UWB combined with Continuous Wavelet Transform (CWT) method to detect human breathing behind a wall.	Target was detected but not in realistic conditions. Non-stationary clutter and NBI were not in their model.
2	B. Levitas and J. Matuzas, 2010.	Conference [*9*].	P1	NA.	BW from 0.5- 2.5 GHz.	Dynamic range is -78 dB/ NA.	Using UWB in breathing detection behind a barrier. Researcher discriminated between the two targets by the breathing rate. The breathing rate of the dog was higher.	Detected a human and a dog behind rubble of a collapsed building.
3	I. Immoreev and S. Samkov., 2005.	IEEE Magazine [*7*].	P1	240	0.33 GHz with central operation frequency of 1 GHz.	Operating range from 0.1 to 4m/ target standing 2 m behind 0.45 m thickness brick wall.	The paper discusses using short-distance UWB radars in medicine and in detection behind walls. Researchers used time of arrival for detection & range gating to eliminate interference and clutter reflections.	Target was detected and was monitored heart rate activity successfully. Measurements were not under realistic conditions.
4	V. Chernyak, 2006	Conference [*56*].	P1	0.1	Center frequency is 2250 MHz with BW of 500 MHz	SNR received is 0 dB/ 50 cm thickness concrete wall.	Used UWB multisite radar device to detect people under rubble.	Very weak signal was detected and the position of the target was localized.
5	A. Yarovoy et al, 2008	IEEE Magazine [*5*].	P1	NA	BW of 11.7 GHz and receiver band is from 1 to 12 GHz.	Dynamic range is 78 dB/NA.	UWB radar with large operational bandwidth was used to detect human breathing behind a wall.	The novelty of the radar lies in its large operational bandwidth combined with excellent time stability.

UWB Impulse Radar Technology (under non-realistic conditions)								
Index	**Author**	**Type of paper**	**Problem addressed**	**Technical Requirements**			**Solutions**	
				Trans. Power (mW)	**BW**	**SNR/Depth**	**Method**	**Main results**
6	J. Edgcombe, 2008.	Journal [*50*].	P1	NA	BW of 500 to 3 GHz.	NA	The paper discusses the latest advances in through wall radar sensing. A comparison was made between NB, UWB, and SAR technologies.	Suitable operating frequency is 1 GHz. Higher frequencies have poor penetration characteristics and lower frequencies have poor resolution. UWB and SAR technologies can be used for detection behind walls. Sensor fusion can be used to reduce false alarms.
7	Zhang et al. 2012	Journal [*15*].	P1, P3	5000	Center frequency is 400 MHz	NA/ Targets are standing 9 m behind a 30 cm thickness brick wall.	They used single-channel UWB radar, Improved SNR by filtering and also moving average subtraction, and used space-frequency analysis to distinguish between stationary human targets.	Two targets were detected behind the wall.
8	Fulerton et al., 2001	US patent No. 035,837 [*118*].	P1	NA	Center freq. between 1-3 GHz	NA	System and method for intrusion detection using a time domain radar array.	Higher angular resolution at a low central frequency. The radar detected human movement around a perimeter of a building.
9	JR. Leach et al., 2006	US patent No. 061,504 [*16*].	P1	NA	Center freq. between 0.9-5 GHz, BW 400 MHz.	Receiver gain 60 dB/ NA	Researchers introduced a system to detect the movement of targets and distinguish between human and animals behind walls. Two low power UWB radars were used in his system.	The system can detect the respiration, heartbeat, movements of an individual or an animal using a system of 2 UWB radars.
10	A. Beeri, 2012	US patent No. 8,098, 168 B2 [*47*].	P1	NA	NA	NA	A system comprises of multiple receivers and transmitters arranged in at least one antenna array to detect movement of targets behind walls. Sampling was provided from several receiving channels.	The system measured the amount of activity behind walls at different hours and used these measurements in a security application or intrusion detection system.
UWB Impulse Radar Technology (under realistic conditions)								
1	J. Li et al., 2012.	IEEE Letter [*13*].	P1, P2	NA	Operating frequency from 200 MHz to 1.6 GHz	NA/0.2 wall of bricks and plaster coating.	UWB radar combined with 2 dimensional FFT was used to detect human breathing behind a wall.	The method had high accuracy and was easy to implement.
2	L. Liu et al., 2011	Journal [*12*].	P1, P2	NA. He referred to [44]	0.5 GHz with central freq. 1.67GHz.	NA/human standing 1 m behind 20 cm thickness concrete wall.	Impulse UWB radar combined with FDTD, FFT, and HHT methods to detect cardio-respiratory signatures of human behind a wall. Data profiles were presented in time domain first to discuss the most obvious chest motion features; then processed by one of the three methods (FDTD-FFT-HHT).	Human breathing was detected. To detected heartbeat higher central operating frequency is required.

UWB Impulse Radar Technology (under realistic conditions)								
Index	**Author**	**Type of paper**	**Problem addressed**	**Technical Requirements**			**Solutions**	
				Trans. Power (mW)	**BW**	**SNR/Depth**	**Method**	**Main results**
3	Singh et al. 2011.	Journal [*24*].	P1, P2	P220 UWB radar has been used	center frequency of 4.3 GHz with a 10 dB bandwidth of 2.3 GHz.	NA/1- 1-ft thick Gypsum wall and man standing at 6.5 ft. 2- A 4 cm wooden door and Person is standing at a distance of 7.6 f from the radar. 3- 12 cm Brick wall. Person is standing at a distance of 8 f from the radar.	Target was detected using FFT or STFT combined with SVD method.	STFT was not suitable for all types of walls.
4	A. Nezirovic,et al., 2007	Conference [*10*].	P1, P2	NA	0.33 GHz	SNR is 15 dB and Signal-to Interference Ratio (SIR) is 48 dB/ NA.	Paper compared between four methods in suppressing NBI from the reflected UWB waveform.	Extract and subtract LMS gave bad results. Filter-and-Restore Linear Interpolation method was the best and it showed an improvement factor of 12.9 dB.
5	A. Nezirovic et al., 2008.	Conference [*11*].	P1, P2	NA	880MHz with center frequency750 MHz	NA/Results have been taken in line-of- site condition.	Human breathing cross-section in the UWB radar was a function of aspect angle for three positions of the body and three combinations of antenna-pair polarization. The paper discussed the effect of the human position on detection.	The highest radar cross section was when the victim was resting on his side and facing the receive antenna. The cross polarized antenna pairs should be avoided.
6	Zhu Zhang, et al, 2013.	IEEE Letters [*70*].	P1, P2	NA	BW of 500 MHz	NA/Rubble of 1 m and a target 0.8 m under the pile of rubble.	The paper discussed the detection of the surrounding rubble structure during survivor detection using UWB radar.	Configuring the rubble positions and human was very helpful for deciding the optimal rescue plan.

UWB Noise Radar Technology (under non-realistic conditions)								
Index	**Author**	**Type of paper**	**Problem addressed**	**Technical Requirements**			Solutions	
				Trans. Power (mW)	**BW**	**SNR/Depth**	Methods	Main results
1	J. Sachs et al., 2008.	Conference [*46*].	P1	NA	BW is 2.5 GHz.	NA/ target is 1.5 m behind a 0.18m thickness wall.	Pseudo-Noise UWB Radar was used to detect human behind walls or under rubble.	Researcher used the trilateration method to track the movement of the targets in the 2-D plane x and y.

Index	Author	Type of paper	Problem addressed	Technical Requirements			Solutions	
UWB Noise Radar Technology (under realistic conditions)								
				Trans. Power (mW)	BW	SNR/Depth	Method	Main results
1	C. Lai	PhD. Dissertation [*60*].	P1, P2, P3	4	500 MHz with center frequency 500 MHz.	NA/50 cm brick wall	Cross-correlated technique was used in the receiver to obtain better ROC.	Detected a human at a distance 10m behind 50 cm brick wall.
UWB Noise Radar Technology (under realistic conditions)								
Index	Author	Type of paper	Problem addressed	Trans. Power (mW)	BW	SNR/Depth	Method	Main results
2	Q. Liu et al., 2012.	Symposium [*68*].	P1, P2	316	1.5 – 4.5 GHz with center frequency 3 GHz	NA/10m	Introduced a compact integrated 100 GS/s sampling module for UWB see-through-wall radar.	Narrow Band Interference (NBI) was easily minimized and high resolution range profile was obtained.
3	Z. Li, et al, 2013.	IEEE Transactions [*69*].	P1, P2	5000	Two radars with center operating and BW frequency of 400 and 270 MHz	NA/two parallel 24 cm thick brick wall separated by 3m. Another model is person standing 3 m from the antenna behind bricks of 2 m thickness.	A novel method for respiration-like clutter cancellation in life detection by dual-frequency IR-UWB radar. The paper was trying to solve the problem of drift where the clutter may act in a way like the human respiration reflected waveform.	Adaptive clutter cancellation (ACC) algorithm specifically for this radar was proposed to remove the respiration-like clutter reflected from walls or rubble, especially from those walls or rubble adjacent to the human target.
4	A.Kumar, 2011.	Thesis [*78*].	P1, P2	NA	Center frequency 4.3 GHz and BW 3.2GHz.	NA/ 0.34 m thickness wall. The target is standing 1m behind gypsum wall, 1.6 m behind a wooden door, and 1.2m behind a concrete wall.	Using pseudo-random UWB radar to detect human behind walls or under ruins.	The system showed no interference with radio signals, low probability of intercept, high resolution and resistant to multipath interferences and jamming.
FMCW UWB Radar Technology (under realistic conditions)								
Index	Author	Type of paper	Problem addressed	Trans. Power (mW)	BW	SNR/Depth	Method	Main results
1	N. Maaref, et al, 2009.	IEEE Transactions [*25*].	P1, P2	NA	1 to 5 GHz.	NA/ three different types of 20 cm thick walls: a hollow brick wall, a hollow concrete wall with a 12 cm thick air gap, and a solid concrete wall.	FMCW UWB radar was been used for through wall detection of human beings. Detection is combined with appropriate differentiator and SVD method.	The attenuation in walls had low value and the RCS of a human had high values when the operating frequency was from 3 to 4 GHz.

FMCW UWB Radar Technology(under non-realistic conditions)								
Index	**Author**	**Type of paper**	**Problem addressed**	**Technical Requirements**			**Solutions**	
				Trans. Power (mW)	**BW**	**SNR/Depth**	**Method**	**Main results**
1	L. Anitori et al., 2009.	Conference [*33*].	P1	25	Operating frequency of 2.4 GHz, 5.7 GHz, 9.4 GHz and 24 GHz.	NA/2.5 m above a person in free space (LOS).	The paper investigated the use of FM-CW UWB radar in people life-signs detection.	FFT and autocorrelation methods were used for target detection.
SFCW UWB Radar Technology (under realistic conditions)								
2	G. Grazzini et al., 2010.	Conference [*62*].	P1, P2	1	operating frequency from 100 MHz to 1 GHz	Dynamic range is 100 dB/ The debris was 1 m thickness.	Researchers used UWB CW-SF Ground Penetrating Radar (GPR) as rescue equipment to detect people after collapse of buildings.	Results show the ability to detect a human lying under one meter thick debris.

Appendix C

C.1 PN-UWB P410 Radar System

The key features of the radar are [*79*]:

- Excellent performance in high multipath and high clutter environments.
- Coherent signal processing which extends operating range.
- Direct sequential pulse sampling which allows measurement of received waveform (resultant waveform is available to the user for ranging optimization)
- Two-Way Time-of-Flight (TW-TOF) ranging technique provides highly precise range measurements with industry-leading update rate.
- Coarse Range Estimation (CRE) technique estimates the range from a transmitting unit by using the received leading edge signal strength.
- UWB chipset enables low cost, small size, and low power operation.
- UWB waveform and pseudo random encoding ensures noise-like transmissions with a very small RF footprint.
- RF transmissions from 3.1 GHz to 5.3 GHz, with center at 4.3 GHz.
- RF emissions compliant with FCC limits.
- Each unit is a full transceiver.
- Single 3” x 3.15” (7.6 x 8.0 x 1.6 cm) board.
- USB or Serial interface.
- Several sleep modes allow user to reduce power consumption.

In the following section, the P410 radar system will be described and the reasons given for its selection.

C.1.1 P410 Radar Transmitter

The P410 Radar transmits a mono-cycle pulse with pulse width equal to 500 ps and duty cycle transmission equal to 10 MHz. Such pulse forms are inherently broadband. Figures C.1 (a) and (b) show the transmitted pulse in time domain and frequency domain, respectively [*79*].

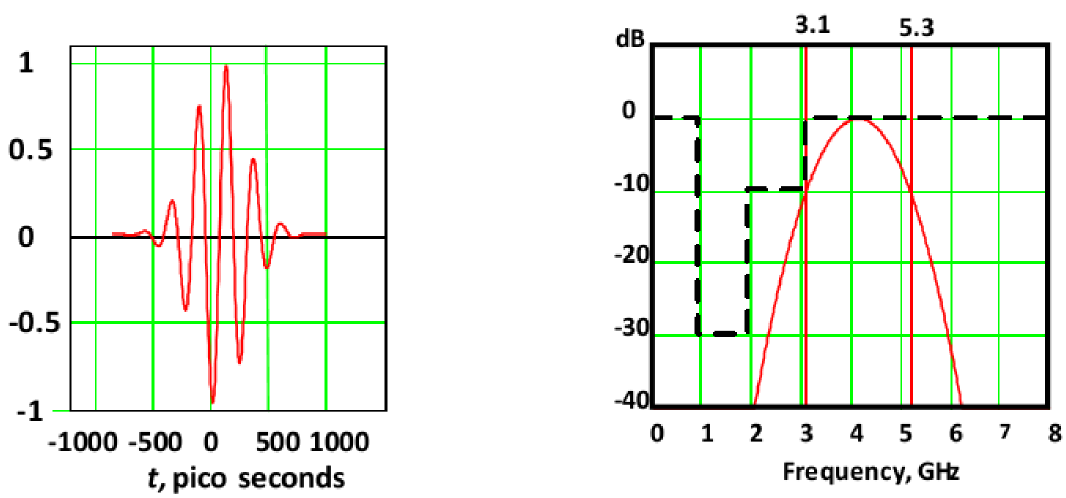

(a) (b)

Figure C.1 P410 UWB transmitted pulse (a) in time domain (b) in frequency domain [*79*].

Figure C.2 is the block diagram of Time Domain UWB transmitter technology. The single bit of information is first modulated and then sent to a programmable time delay chip. The programmable time delay unit uses Pseudo-random Noise codes (PN codes) generated from the code generator to shift each pulse actual transmission time. This is called a Pulse Position Modulation (PPM) scheme. After performing the time delay process, the output of the programmable time delay unit is used to trigger the pulse generator. The output of the pulse generator is transmitted via the antenna [*78*].

The transmitted waveform has a noise-like appearance. This noise-like appearance has two advantages. First, it is unlikely that transmissions will interfere with other UWB or non-UWB devices. Second, these transmissions are very hard for others to detect, especially at a distance. Therefore, these transmissions have excellent Low Probability of Intercept/Low Probability of Detection (LPI/LPD) characteristics [*79*].

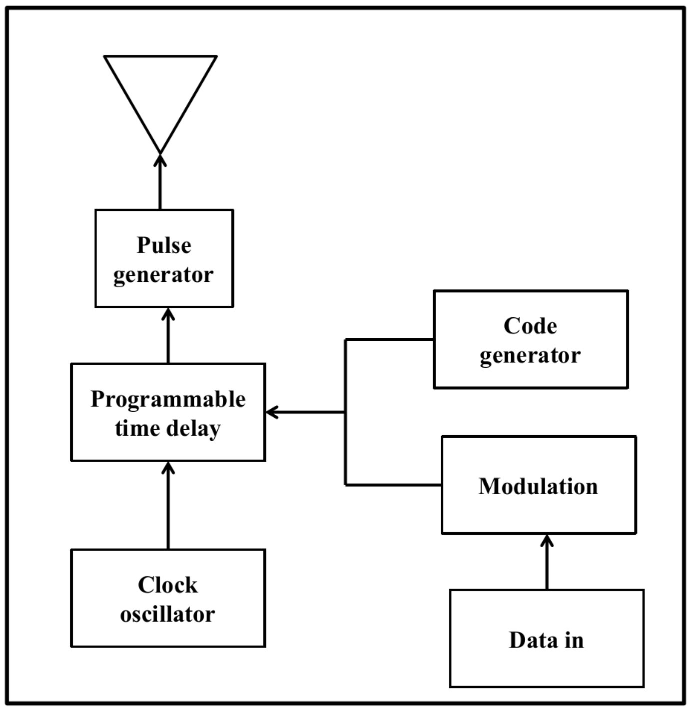

Figure C.2 TM-UWB transmitter block diagram [*78*].

C.1.2 P410 Radar Receiver

Figure C.3 is the Time-Domain UWB receiver block diagram. The architecture of receiver resembles the transmitter, except that the pulse generator feeds the multiplier with a template waveform within the correlator. The input to the correlator is the received signal from the antenna and the output of the pulse generator is triggered with the output of the programmable delay unit as in the transmitter. The P410 radar uses a cross-correlation receiver which multiplies the received signal with a template signal and integrates the output over time. The receiver uses the PN code to estimate the receiving relative time. The output of the receiver is the amplitude of the cross-correlation process and the relative time position.

If the transmitted signal is $x(t)$ and the received signal is $y(t)$, then the output of the cross-correlation process will be:

$$R_{yx}(\tau) = \frac{1}{T}\int_0^T y(t)x(t+\tau)dt \tag{C.1}$$

where τ is the time delay between $x(t)$ and $y(t)$. The information of interest is the impulse response function of the channel which includes the transmission channel, transmit antenna, scatter, and receiver antenna.

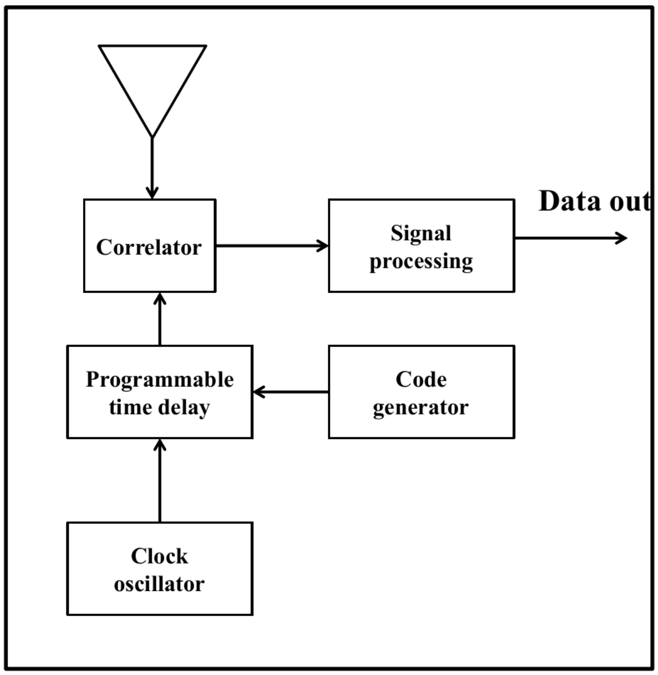

Figure C.3 TM-UWB receiver block diagram [*78*].

If $R_{xx}(\tau)$ is the autocorrelation of the transmitted signal, then the output of the receiver is the convolution between $R_{xx}(\tau)$ and the impulse response of the channel. If the transmitted signal is the UWB signal (appears like Delta function in time domain), the output $R_{yx}(\tau) \approx h(t)$, where $h(t)$ is the channel impulse response [*77*].

C.1.3 P410 Radar in or near Buildings

This research's main target is to use radar that allows for human breathing detection behind walls. There are two factors that affect the radar detection performance in or near buildings. The first is the attenuation in the received signal through wall materials, and the second is the multipath.

According to the attenuation problem, both the electrical and homogenous properties of the wall must be considered. Attenuation of the signal is dependent on the electrical properties and on the number of objects that will scatter the signal. Interfaces can be any form of man-made objects, different kinds of materials in the wall or other interfaces [*60*].

Other factors responsible for limiting radar's depth of penetration include wall thickness (sometimes referred to as the wall effect) [*60*], reflection coefficient of the medium [*119*], moisture level [*120*], presence of magnetic materials in the area of interest [*121*] , and the choice of frequency band to be used. The rule of thumb applied here is that the higher the operating frequency, the better the resolution but the worse the penetration depth [*122*,*123*,*124*,*125*].

In the case of detection behind the walls, if we set the penetration requirements to those of brick walls with a total thickness up to 40 cm (in one way propagation), then an operating frequency from 1.6 to 2.4 GHz or from 3 to 4 GHz gives good penetration performance [*64*]. The radar cross section of a human target has its highest value in the frequency range from 3 to 4 GHz [*25*]. However, decreasing the center operating frequency below 1 GHz results in increasing the received SNR [*26*,*34*]. Typical building materials used in walls can vary from plasterboard or thin smooth concrete with attenuation (at, say, 2 GHz) of 1-2 dB to dense brick with attenuation of several tens of dB. The receiver operating characteristics (ROC) curve in [*60*] shows the lowest probability of detection when the target is standing behind a wet brick wall.

The system has to cope with the different types of building material used. The P410 operating band is from 3.1 GHz to 5.3 GHz with center frequency 4.3 GHz. For that reason, P410 radar is suitable for our application.

According to the multipath problem, P410 radar can resolve multipath and detect small movements in highly cluttered environments. Some of the reflected signals from multipath interfere constructively and some interfere destructively. P410 radar uses multipath to enhance the received signal strength by detecting the strongest signal present.